iScience

CellPress

Article

Optimizing Group Transfer Catalysis by Copper Complex with Redox-Active Ligand in an Entatic State

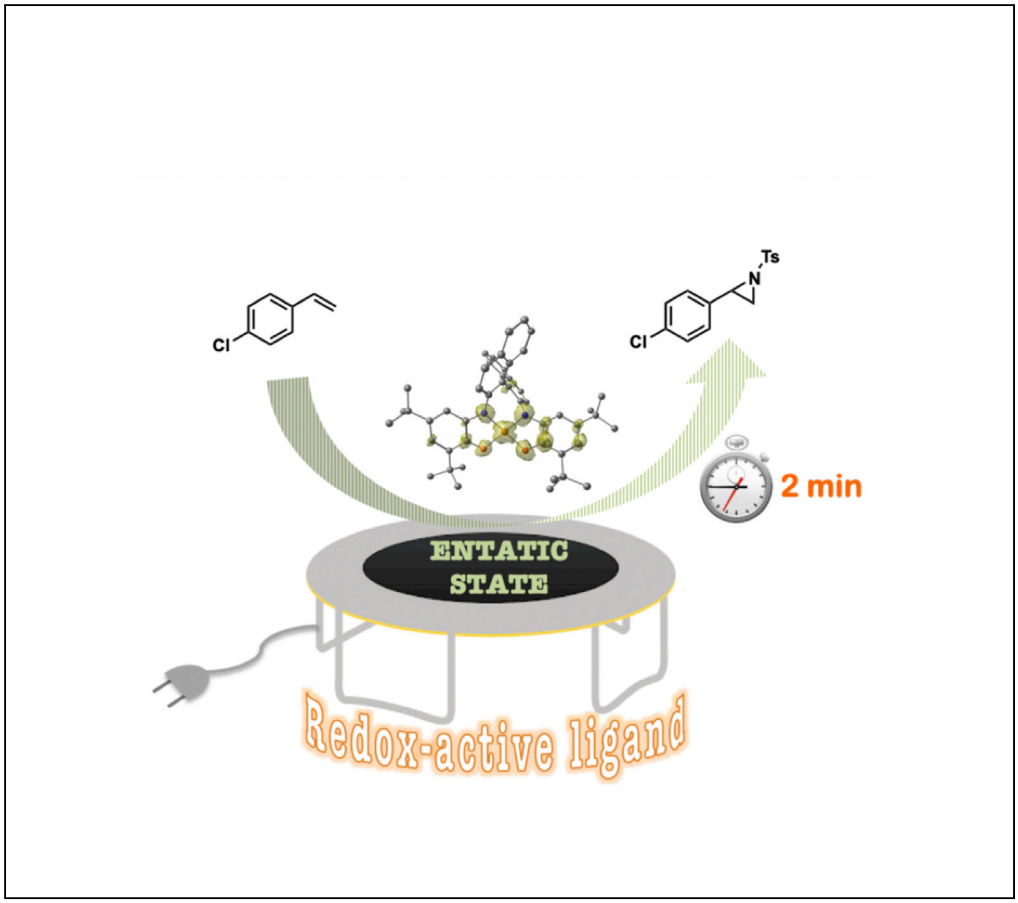

Yufeng Ren, Jeremy Forté, Khaled Cheaib, ..., Maylis Orio, Sébastien Blanchard, Marine Desage-El Murr

desageelmurr@unistra.fr

HIGHLIGHTS

We design a catalyst interfacing two reactivity-enhancing tools from metalloenzymes

This work merges redox-active cofactors and entatic state reactivity

The modifications in the coordination sphere lead to enhanced catalytic behavior

These results open perspectives in bioinspired catalysis and group-transfer reactions

Ren et al., iScience *23*, 100955
March 27, 2020
https://doi.org/10.1016/j.isci.2020.100955

iScience

CellPress

Article

Optimizing Group Transfer Catalysis by Copper Complex with Redox-Active Ligand in an Entatic State

Yufeng Ren,[1] Jeremy Forté,[1] Khaled Cheaib,[1] Nicolas Vanthuyne,[2] Louis Fensterbank,[1] Hervé Vezin,[3] Maylis Orio,[2] Sébastien Blanchard,[1] and Marine Desage-El Murr[4,5,*]

SUMMARY

Metalloenzymes use earth-abundant non-noble metals to perform high-fidelity transformations in the biological world. To ensure chemical efficiency, metalloenzymes have acquired evolutionary reactivity-enhancing tools. Among these, the entatic state model states that a strongly distorted geometry induced by ligands around a metal center gives rise to an energized structure called entatic state, strongly improving the reactivity. However, the original definition refers both to the transfer of electrons or chemical groups, whereas the chemical application of this concept in synthetic systems has mostly focused on electron transfer, therefore eluding chemical transformations. Here we report that a highly strained redox-active ligand enables a copper complex to perform catalytic nitrogen- and carbon-group transfer in as fast as 2 min, thus exhibiting a strong increase in reactivity compared with its unstrained analogue. This report combines two reactivity-enhancing features from metalloenzymes, entasis and redox cofactors, applied to group-transfer catalysis.

INTRODUCTION

The biological world offers potential clues to solve the current pressing energy and resources-related issues (Adesina et al., 2017; Rudroff et al., 2018). The efficiency of biological catalytic systems faces chemists with the challenges of transferring enzymatic performance into synthetic small-molecule catalysts using non-noble metals. Metalloenzymes use earth-abundant *3d* metals and amino acid-derived coordination spheres to achieve complex (multi)electronic transformations required for small-molecule activation and atom transfer reactions. To fulfill these stringent criteria of natural resources, metalloenzymes have evolved reactivity-enhancing strategies aimed at performing such difficult transformations through more favorable thermodynamic pathways. The entatic state concept stems from the observation that single molecule coordination complexes designed as metalloenzymes models often fail to exhibit properties similar to the natural metalloenzymatic active sites (Vallee and Williams, 1968; Williams, 1971, 1995; Stanek et al., 2018). It was thus suggested that secondary and tertiary structures induced by amino acid-based side chains in proteins provide distortions in the coordinative environment that endow the metal center with enhanced reactivity, to which Vallée and Williams refer as "a catalytically poised state" (Vallee and Williams, 1968). Strikingly, a strong link between local geometric frustration induced by tertiary structure effects around enzymatic catalytic sites and their catalytic activity has recently been unveiled (Freiberger et al., 2019). Frustration patterns were demonstrated to be evolutionarily highly conserved, more than the primary structure or residues forming the catalytic site itself, which establishes the central relevance of coordinative distortion to enzymatic catalytic activity.

Entasis is well known in copper proteins involved in electron transfer such as blue copper proteins and has traditionally been studied in the context of Cu^{I}/Cu^{II} oxidation states. When tetracoordinated, these two oxidation states have distinct geometric requirements from tetrahedral to square planar, and the entatic state exhibits an in-between distorted geometry that minimizes energetic penalties arising from coordinative reorganization (Figure 1A). Possible designs for coordination spheres inducing ligand misfit have been discussed by Comba (2000). The majority of reports involve two ditopic or one cyclic tetradentate ligand and include systems with biphenyl subunits (Malachowski et al., 1999; Müller et al., 1996, 1988), multiple bonds and rigid or substituted structures, carbohydrate backbones (Garcia et al., 2015), and guanidinoquinoline ligands (Hoffmann et al., 2013; Stanek et al., 2017). More recently, the entatic state concept was extended to photoinduced electronic transfers (Dicke et al., 2018) thus showing the continued relevance

[1]Sorbonne Université, Institut Parisien de Chimie Moléculaire, UMR CNRS 8232, 75005 Paris, France

[2]Aix Marseille Université, CNRS, Centrale Marseille, iSm2, UMR CNRS 7313, 13397 Marseille, France

[3]Université des Sciences et Technologies de Lille, LASIR, UMR CNRS 8516, 59655 Villeneuve d'Ascq Cedex, France

[4]Université de Strasbourg, Institut de Chimie, UMR CNRS 7177, 67000 Strasbourg, France

[5]Lead Contact

*Correspondence: desageelmurr@unistra.fr

https://doi.org/10.1016/j.isci.2020.100955

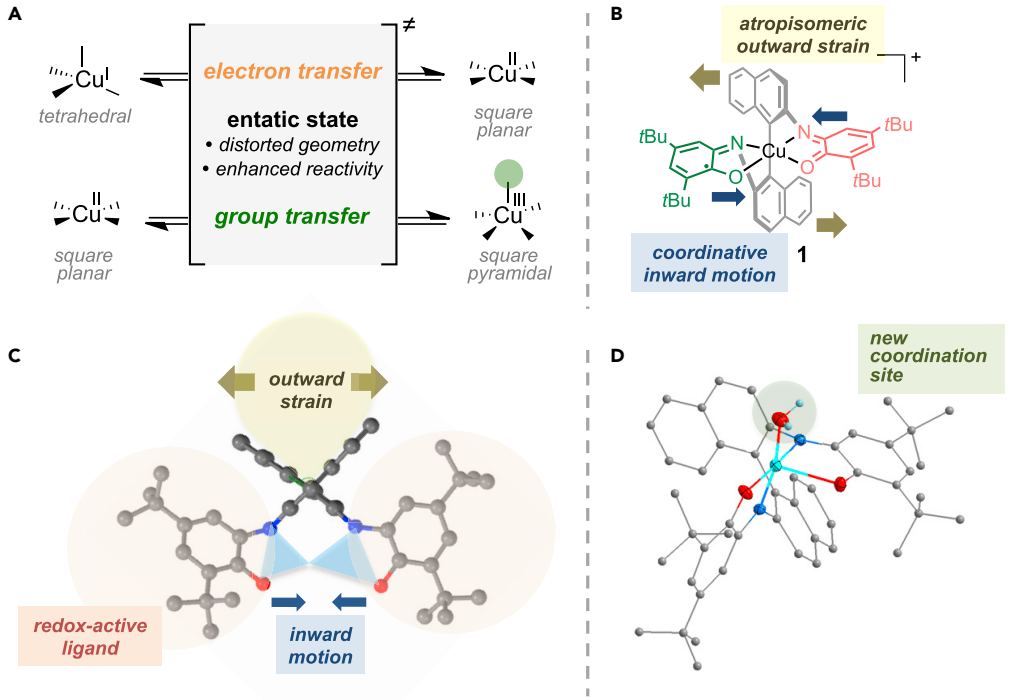

Figure 1. Design of a Redox-Active Ligand Creating a Vacant Coordination Site at Metal through Strong Coordination Distortion

(A) The entatic state reactivity model for electron and group transfer in a tetracoordinated copper complex.

(B) Structure of complex **1** $[CuBINap\ (SQ\text{-}BQ)]^{+}$.

(C) X-ray crystal structure of ligand **2** representing the associated strains.

(D) X-ray crystal structure of complex **1** exhibiting a pentacoordinated coordination sphere resulting from coordination strain.

of this biomimetic feature in electron transfer chemistry. Although most studies focus on electron transfer involving a Cu^{I}/Cu^{II} redox couple, the seminal article by Vallée and Williams (Vallee and Williams, 1968) states that entatic behavior arising from ligand misfit also extends to enzymatic metallic sites performing "transfer of an atom, radical, or a group," as well as higher metallic oxidation states such as Co^{II}/Co^{III} in corrin enzymes and Fe^{II}/Fe^{III} (Mara et al., 2017). A recent report on the hydroxylation of methane to methanol by heterogeneous catalysis performed by iron-containing zeolithes demonstrates that the zeolithe lattice induces a matrix strain that activates a square planar Fe(II) site into a Fe(IV) = O reactive center through entasis (Snyder et al., 2016), and a bispidine Fe(IV) = O species in an entatic state has been reported to perform oxygen-group transfer in homogeneous catalysis (Comba et al., 2016). These examples of oxygen-group transfer systems, which emulate natural systems' catalytic arsenal, provide great opportunities for the design of synthetic systems able to perform highly desired transformations such as multi-electronic small-molecule activation. However, to date, no synthetic catalytic system was demonstrated to perform group transfer other than oxygen through the entatic state model.

Just as the entatic state principle provides a fruitful trail of inspiration for coordination chemists, other biomimetic strategies, related to electron transfer, focus on enzymatic redox co-factors that provide electrons to the active sites (Stubbe and van der Donk, 1998; Davidson, 2018). Such systems are known as redox-active ligands. This field of research is morphing into an area of intense development aimed at harnessing the potential of systems with rich redox flexibility (Albold et al., 2019; Blanchard et al., 2012; Broere et al., 2015; Chirik and Wieghardt, 2010; Grützmacher, 2008; Kaim, 2011; Luca and Crabtree, 2012; Lyaskovskyy and de Bruin, 2012; Praneeth et al., 2012; van der Vlugt, 2012, 2019). Recently, an entatic pair of copper complexes bearing redox-active guanidine ligands was shown to enable fine-tuning between metal- and ligand-based electronic transfers (Schrempp et al., 2017). This structural study was the first report interfacing the two concepts of entasis and redox-active ligands and was focused on the electronic behavior of the entatic pair. Using redox-active copper complex $Cu(SQ)_2$ (SQ: iminosemiquinone) originally

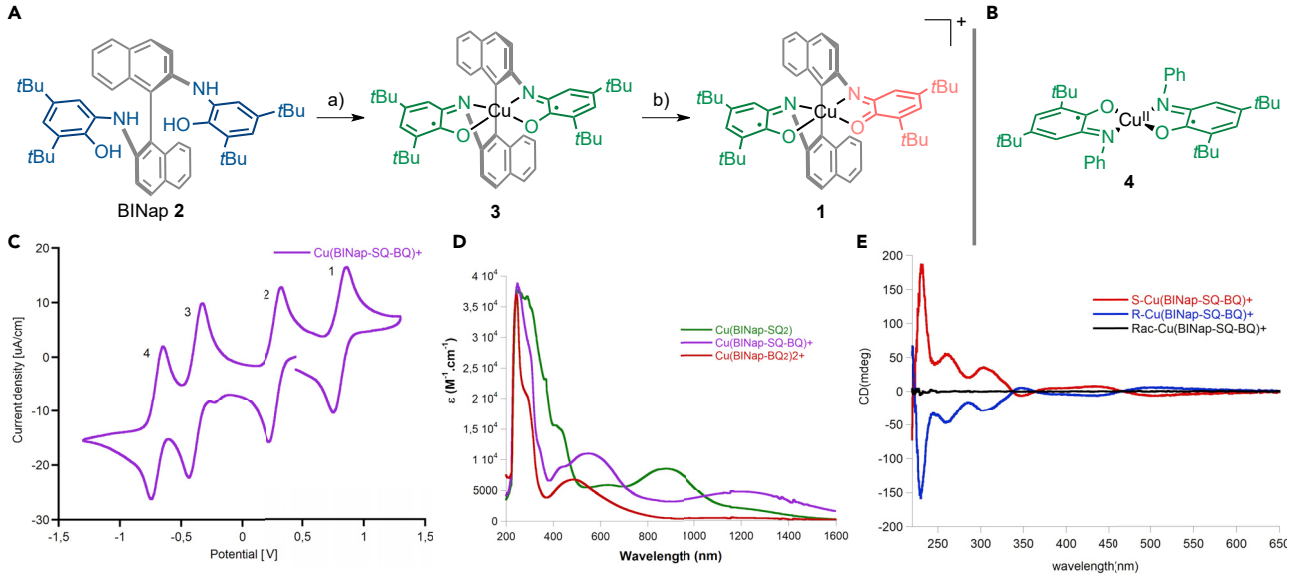

Figure 2. Synthesis and Spectroscopic Studies for Complex 1

(A) Synthetic scheme for complex **1**, reaction conditions: (a) CuCl (1 equiv.), Et_3N (4 equiv.), dry acetonitrile; (b) AgOTf (1 equiv.).

(B) Unstrained complex $Cu(SQ)_2$ **4**.

(C) Cyclic voltammogram of complex **1**.

(D) UV-vis-NIR spectrum of $[Cu(BINap\text{-}SQ\text{-}BQ)]^+$ **1** (purple), $Cu(BINap\text{-}SQ_2)$ **3** (green), and $[Cu(BINap\text{-}BQ_2)]^{2+}$ **5** (see Supplemental Information for structure, red); 0.1 mM in DCM at rt.

(E) Circular dichroism spectrum of racemate and enantiopure $[Cu(BINap\text{-}SQ\text{-}BQ)]^+$ **1** (C = 0.3 mM).

developed as a galactose oxidase (GAO) model (Chaudhuri et al., 1998, 2001), we have shown that ligand-based redox activity influences the overall reactivity of the complex toward electron transfer (Jacquet et al., 2016a, 2017), C–N bond formation (Jacquet et al., 2016b), and nitrogen group transfer (Ren et al., 2018) while preserving a Cu(II) oxidation state. Here we report an acyclic tetradentate redox-active ligand exhibiting C_2 symmetry with overall three possible rotations around single bonds (degrees of freedom). This particular geometry induces enhanced catalytic reactivity of resulting complex **1** through entasis. This specific ligand design combines an atropisomeric backbone, which enforces chirality and exerts an outward strain, with a redox-active iminosemiquinone/iminobenzoquinone ONNO coordination sphere that pulls in the opposite inward direction toward metal chelation (Figure 1B). These conflicting steric demands induce a coordination stress while the bridging binaphthalene backbone installs full conjugation between the two redox-active units, resulting in enhanced electronic delocalization. Complex **1** performs catalytic nitrogen and carbon group transfer in as fast as 2 min on a model substrate and exhibits up to a 40-fold increase in synthetic efficiency compared with its unstrained analogue $Cu(SQ)_2$. Moreover, it can convert sterically hindered or unactivated alkenes. The present work shows that interfacing two reactivity-enhancing features from metalloenzymes, such as entasis and redox cofactors, can improve group-transfer catalysis.

RESULTS

Complex Synthesis and Structural Studies

Condensation of two *tert*-butylcatechol with 1,1′-binaphthyl-2,2′-diamine yields easy access to 1,1′-binaphtyl-2,2′-diaminophenol (hereafter noted BINap) ligand (Figure 2A and Supplemental Information), and its structure was confirmed by X-ray crystallography (Figure 1C). Aerobic complexation of BINap ligand **2** with copper chloride affords complex $Cu(BINap\text{-}SQ_2)$ **3** as a green solid. The spectroscopic signature of **3** (Figures 2C–2E) is very similar to those of $Cu(SQ)_2$ **4** (Figure 2B) and $Cu(L_{Biphen}SQ_2)$, a copper complex reported by Chaudhuri and incorporating a biphenyl unit instead of the atropisomeric binaphthyl unit (Mukherjee et al., 2008). At 10 K, **3** displays an S = 1/2 signal centered on the copper (Figure S10), as attested by the strong anisotropy of the EPR spectrum and the presence of hyperfine coupling with the I = 3/2 copper nucleus. The doublet ground spin state of **3** is further supported by density functional theory (DFT) calculations (Table S15). The UV-vis spectrum of **3** (Figure 2D) presents the expected ligand-to-ligand

(SQ to SQ) charge transfer band around 900 nm (800 nm in **4** and 880 nm in Cu($L_{Biphen}SQ_2$)), which points toward **3** as a Cu(II) complex bearing a dianionic diradical BINapSQ$_2$ ligand. This description is in agreement with the DFT-calculated electronic structure of **3** (Figures S110 and S111). The cyclic voltammogram of **3** displays four reversible waves (two oxidative and two reductive, Figure S9) at redox potentials very close to those of the parent complexes, indicating similar electronic structures and ligand-based redox processes (Tables S1 and S2).

Oxidation of Cu(BINap-SQ$_2$) **3** with Br_2 followed by halide abstraction led to the formation of fully oxidized $[Cu(BINap\text{-}BQ_2)]^{2+}$ **5**. The singly oxidized complex $[Cu(BINap\text{-}SQ\text{-}BQ)]^{+}$ **1** can be prepared either by oxidation of **3** with 1 equiv. $AgPF_6$ or by mediamutation between an equimolar mixture of complexes **3** and **5** (see Supplemental Information). Cyclic voltammograms of **1** and **5** are very similar to that of **3** and only differ by the onset potential, thus attesting the chemical reversibility of the redox processes. Complex **1** is X-band EPR silent at 10 K, whereas **5** displays an EPR spectrum in agreement with an S = 1/2 ground state centered on the copper (Figure S13). The doublet ground spin state of **5** has been also predicted by DFT calculations (Figures S113 and S114). The UV-vis spectrum of **1** displays around 1,200 nm an ligand-to-ligand charge transfer (LLCT) band associated with the oxidation of an SQ moiety into BQ, whereas no LLCT can be identified for fully oxidized **5** (Figure 2D). This is reminiscent of the parent complexes and confirms that the two oxidation processes are ligand centered. Enantiopure R or S complexes of **1** and **3** can be synthesized from enantiopure R or S forms of **2**, as attested by circular dichroism and chiral HPLC analysis (Figures S3 and S5).

Attempts to grow crystals of **3** led to very weakly diffracting samples, with maximum resolution of 1.29 Å (see Supplemental Information), which indicates that the copper center is in coordinence 4 (N_2O_2 of BINap). Crystals suitable for X-ray diffraction were obtained on racemate and enantiopure samples of complex **1** and revealed that the coordination sphere is completed by an aquo ligand to provide a square pyramidal environment in which an oxygen atom of the BINap occupies the axial position and not the water molecule (from a CCDC database search, of 126 structures of 5-coordinated Cu complexes bearing $\{(NCCO)_2 + OH_2\}$ coordination sphere, only five do not display a square pyramidal geometry with water as apical ligand) (Figure 1D). This unusual coordination sphere can be explained by the coordination stress resulting from the design of ligand **2**, and the singly oxidized SQ-BQ redox-active subunit, which bears increased electrophilicity compared with complex **3**. The combination of these unique steric and electronic features induces a distorted pentacoordinated sphere with a newly occupied coordination site. The atropisomeric backbone exerts an outward strain associated to the large torsion angle between the two naphthalene rings (99.9° in free ligand **2**, 66.7° in the complex) and opposes to N_2O_2 and Cu being in the same plane. The long axial Cu-O_{BINap} distance (2.309(2)Å) indicates a weak coordination. Detailed analysis of the bond distances in coordinated BINap ligand shows that this O atom belongs to the benzoquinone part of the ligand (bond lengths in this part of the ligand of $d_{C\text{-}O}$ = 1.235(4)Å, $d_{C\text{-}C}$ = 1.519(15)Å, and $d_{C\text{-}N}$ = 1.289(5) Å), whereas the in-plane half of the ligand corresponds to the iminosemiquinone moiety ($d_{C\text{-}O}$ = 1.288(4)Å, $d_{C\text{-}C}$ = 1.455(5)Å, and $d_{C\text{-}N}$ = 1.344(4)Å) (Chaudhuri et al., 2001). Such deviation from square planar geometry has been reported in the context of a salen-based Cu^{II} GAO functional mimic with an atropisomeric backbone by Stack and co-workers (Wang et al., 1998). DFT calculations provided insights into the electronic features of complex **1**, which can be assigned as a Cu(II) center bound to a radical BINap ligand (Figures S113 and S114). The system is characterized by a triplet S = 1 ground spin state due to moderate ferromagnetic coupling between the metal center and the ligand radical moiety (Table S15). A singlet S = 0 state is close enough in energy to be thermally populated.

Nitrogen-Group Transfer Reaction: Aziridination

We have previously reported copper-catalyzed aziridination with unstrained complex **4** bearing two independent redox-active iminosemiquinone units and exhibiting a planar geometry around the copper center (Figure 2B) (Ren et al., 2018). Complex **4** can perform aziridination on a wide range of unactivated alkenes through a mechanism involving molecular spin catalysis, related to the multistate reactivity model encountered in metalloenzymes. Aiming to assess the effect of tetratopic ligand **2** in comparison with two independent ditopic redox-active units, the reactivity of complex **1** in aziridination was therefore investigated.

To examine the influence of ligand strain and redox state, we performed benchmarking reactivity tests under identical conditions on all three possible redox state combinations (SQ/SQ, SQ/BQ, and BQ/BQ) of the redox-active units for the unstrained (**4**, **6**, **7**) and strained (**3**, **1**, **5**) complexes (Table S10). Strikingly, complex **1** was found to outperform all other complexes, delivering the aziridination adduct **8** of

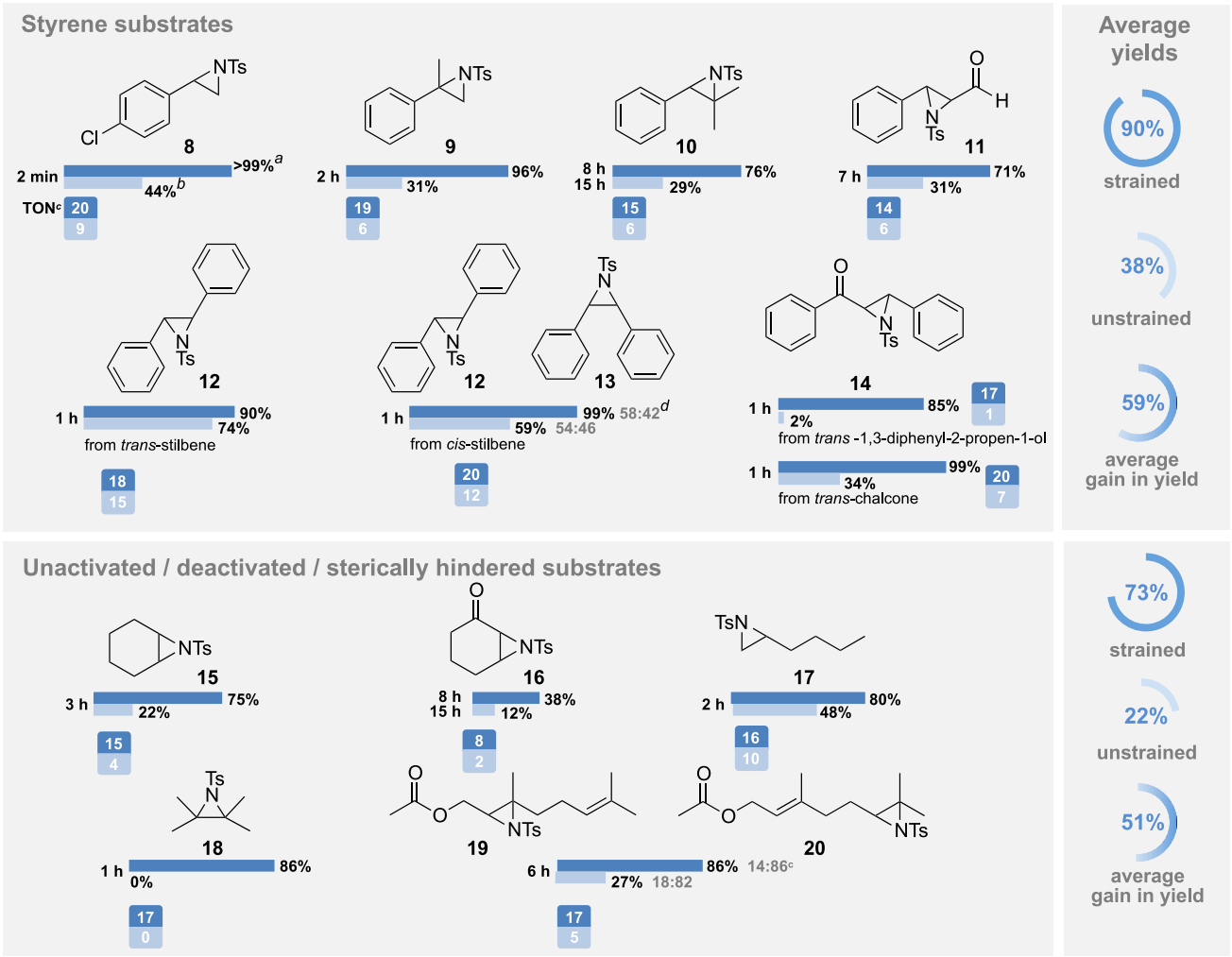

Scheme 1. Scope for Nitrogen-Group Transfer with Complex 1 and Comparison with Unstrained Analogue 4

Aziridination reaction performed with [a]complex **1** [CuBINapSQ-BQ]$^+$ (dark blue), [b]complex **4** $Cu(SQ)_2$ (pale blue), [c]TON calculated for complexes **1** and **4** [d] ratio of products (numbers in gray). Reaction conditions: 4-chlorostyrene (1 equiv.), PhINTs (2 equiv.), complex (5 mol%), acetonitrile, rt. Yields were determined by ^{1}H NMR using trimethoxybenzene as internal standard and calculated considering olefin as limiting reactant.

4-chlorostyrene in quantitative yield. These results suggest that the major reactivity improvement observed with complex **1** is linked to two factors: electronic conjugation between the SQ and BQ redox-active subunits and high steric strain induced by the ligand. Interestingly, the SQ-BQ redox state $Cu(L_{Biphen}SQ\text{-}BQ)^+$ of a functional galactose oxidase model, was suggested to be involved in the catalytic activity. This model incorporates a biphenyl unit instead of the atropisomeric binaphthyl unit and thus retains full conjugation between the redox-active subunits but does not exert steric strain as rotation around the arylic C–C bond is possible in the biphenyl unit but not in the atropisomeric binaphthyl unit (Mukherjee et al., 2008). This provides strong grounds for the role of electronic communication installed between redox-active subunits through the conjugated backbone on the redox state of the reactive complex. The second factor for the major reactivity improvement is the high steric strain observed in complex **1**. This observation is reminiscent of the entatic state model, defined as a strong steric distortion induced by ligands in a metal complex leading to improvement in catalytic activity (Vallee and Williams, 1968).

The scope of the reaction was evaluated (Scheme 1) and revealed the ability of complex **1** to perform aziridination on a wide range of substrates including mono-, di-, and trisubstituted double bonds, as well as electrophilic functions (**11** and **14**) with yields from 76% up to quantitative (**8**–**10**). Trans-stilbene gave the corresponding *trans* diastereoisomer **12** in 90% yield, whereas *cis*-stilbene provided a mixture of

cis- and *trans*-aziridines (**12** and **13**), thus pointing toward a probable radical mechanism accounting for *cis-trans* isomerization toward the most stable *trans* isomer. Also, conversion of unactivated alkenes (**15** and **17**) could be performed in up to 80% yield, whereas aziridination of a deactivated substrate afforded the expected product in 38% yield. Tetrasubstituted substrate **18**, unreactive with complex **4**, was transformed in 86% yield within an hour. Reaction on a geraniol derivative led to products **19** and **20** in higher yield compared with the unstrained complex, and regioselectivity was reinforced toward the less hindered site in accordance with the high steric hindrance in complex **1**. The most striking results are observed when comparing catalysis with strained complex **1** and the most efficient unstrained analogue from our benchmarking reactivity test complex **4** $Cu(SQ)_2$. Reaction time could be divided by up to a factor 8 for compounds **10**, **11**, and **16**–**20**, and yields increased up to 42-fold (compound **14**), thus demonstrating the efficiency of complex **1**. Based on the substrate scope, average yields of 90% for styrene substrates and 73% for unactivated or hindered substrates are obtained with complex **1**, whereas the unstrained analogue **4** provides much lower average yields (38% and 22%, respectively). The calculated average gain in yield observed is 59% and 51%, respectively (calculated as the mean value of subtracted yields). This indicates that steric strain in complex **1** is accountable for a major reactivity improvement. TON (turnover number) was calculated and found to be significantly and consistently higher in the case of complex **1** versus its unstrained analogue (Scheme 1). The maximum TON value of 20 was found for substrate **8**, along with a TOF (turnover frequency) of 600 h^{-1}. In the case of styrene, we checked that, once the aziridination reaction was complete with either complex **1** (after 2 min) or complex **4** (after 12 min) as a catalyst, addition of new equivalents of styrene and PhINTs led to the formation of the aziridination product in 95% yield for **1** and 82% yield for **4**: thus, little or no deactivation of the catalyst occurs during the reaction. Since the BINap ligand exhibits axial chirality, the two enantiomers of complex **1** were prepared from commercial enantiopure 1,1′-binaphthyl-2,2′- diamine and the S-isomer was tested in the reaction with 4-chlorostyrene. However, only modest enantiomeric excesses were observed with a maximum 35% ee (Table S8). This could be related to the fact that the chirality-inducing atropisomeric motif is remote from the coordination sites involved in the reaction, which disfavors enantioselectivity.

Carbon-Group Transfer Reaction: Cyclopropanation

Having established the efficiency of complex **1** in N-group transfer, we investigated its ability to perform C-group transfer with ethyl diazoacetate (EDA), a carbene precursor used in metal-based cyclopropanation reactions. Optimized reaction conditions (Tables S11–S14) led to the isolation of the cyclopropanated adduct **21** of 4-chlorostyrene in quantitative yield, and the scope of the cyclopropanation reaction was studied (Scheme 2). A wide range of substrates including diverse mono- and disubstituted styrene derivatives (**21**–**26**) and polycyclic (**27**–**28**) substrates as well as unactivated or deactivated tri- and tetrasubstituted scaffolds (**29**-**30**) was efficiently converted. Similarly as before, complex **1** was found to systematically outperform the most efficient unstrained analogue (complex $[Cu(SQ\text{-}BQ)]^+$ in this case) and deliver average yields of 95% and 97% on styrene derivatives and unactivated or hindered substrates, respectively, whereas the unstrained complex reached 67% and 81% average yields, respectively. This translated into average gains in yield of 21% and 16% for the two substrate scope categories. The lower gain observed with complex **1** in cyclopropanation compared with aziridination can be explained by the reaction conditions. Reaction yields are assessed over a fixed period of time set by the best performing catalyst, and the reaction is stopped upon completion of maximum conversion by the best catalyst (complex **1**). Although the aziridination reaction is very fast and can be performed in as fast as 2 min, the cyclopropanation conditions require that the carbene source is added slowly over 20 min to the reaction mixture to avoid unproductive homo-coupling of EDA as side product. Although this accounts for both longer reaction times and decreased gains in yield, complex **1** remains more efficient than the unstrained complex, and this is further confirmed by the calculated TON values close to 100 and a calculated TOF of 300 h^{-1} for complex **1** with substrate **21**.

Mechanistic Studies

Mechanistically, metal-catalyzed aziridination and cyclopropanation rely on the formation of transient and highly reactive metal-carbene (Dzik et al., 2010, 2011) and metal-nitrene (Suarez et al., 2013; Goswami et al., 2015; Corona et al., 2016; Kuijpers et al., 2017; Fujita et al., 2018) species, which have been actively investigated in the context of ligand noninnocence. High-resolution mass spectrometry performed on an aliquot of a mixture of complex **1** and excess nitrene (respectively, carbene) source at −80°C evidences the presence of a species at m/z 920.3522 (respectively, m/z 837.3693) corresponding to the formation of mono-nitrene adduct [**1**-NTs] (respectively, mono-carbene adduct [**1**-$C(H)CO_2Et$]) (Figures S23 and S26). UV-vis

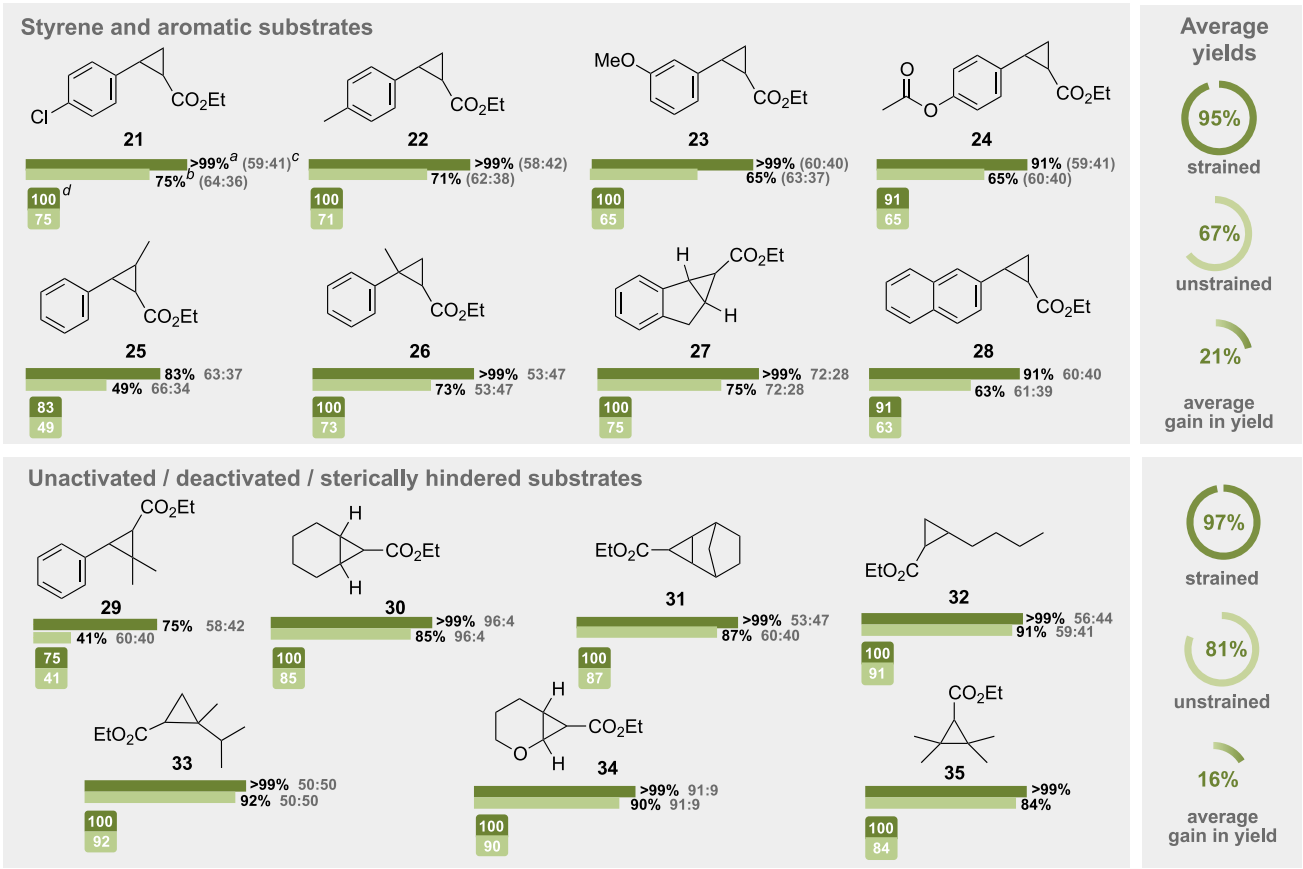

Scheme 2. Scope for Carbon-Group Transfer with Complex 1 and Comparison with Unstrained Analogue

Cyclopropanation reaction performed with [a]complex **1** $[CuBINapSQ\text{-}BQ]^+$ dark green, [b]complex **6** $[Cu(SQ\text{-}BQ)]^+$ pale green, [c]trans/cis ratio. Reaction conditions: 4-chlorostyrene (1 equiv.), EDA (2 equiv.), copper complex (1 mol%), DCM, rt. EDA was added slowly in 20 min, reaction time: 20 min. Yields were determined by ^{1}H NMR using trimethoxybenzene as internal standard and calculated considering olefin as limiting reactant. [d]Calculated TON for complexes **1** and **6**.

studies of complex **1** with the nitrene or carbene sources (Figures S24, S27, and S28) show rapid disappearance of the intervalence band around 1,200 nm, in agreement with an electron transfer from the BINapSQ-BQ ligand to the nitrene upon coordination thus generating $[Cu(BINap\text{-}BQ_2)]^{2+}$ **5**, which does not present any LLCT band. To further assess the efficiency of complex **1**, reaction kinetics were studied by ^{1}H NMR, and it was observed that aziridination with complex **1** is complete in less than 2 min (Figure 3A), whereas cyclopropanation yields the final product in 20 min upon slow addition of EDA over the course of the reaction (Figure 3B).

The group transfer reactions were studied by continuous wave EPR spectroscopy and operando mode, as our previous work has shown that these techniques can monitor the redox state changes of the complexes and provide structural and kinetic insights into the intermediate species (Figures 3C and 3D) (Jacquet et al., 2016b). Regarding the aziridination reaction (Figure 3C), the first important observation is the absence of spectral differences between the beginning and the end of the reaction (2 h), indicating that the catalytic reaction is extremely fast. X-band EPR spectra of complex **1** alone shows that the starting complex is EPR silent from 5 K to room temperature. However, when the aziridination reaction with complex **1** is followed by operando studies (Figure 3C), two signals are immediately observed: one typical of a Cu^{2+} species (g_{iso} = 2.12 and A_{iso} = 82 G) and the other an organic radical displaying five lines with a coupling of 12.2 G and an intensity ratio of 1:2:3:2:1. The latter can be attributed to the formation of an organic radical coupled to two magnetically equivalent nitrogens. This suggests that nitrene incorporation instantaneously leads to a Cu^{2+} species with formation a ligand-based radical, these two species not being magnetically coupled. These EPR results indicate fast electron transfer from the starting complex to the

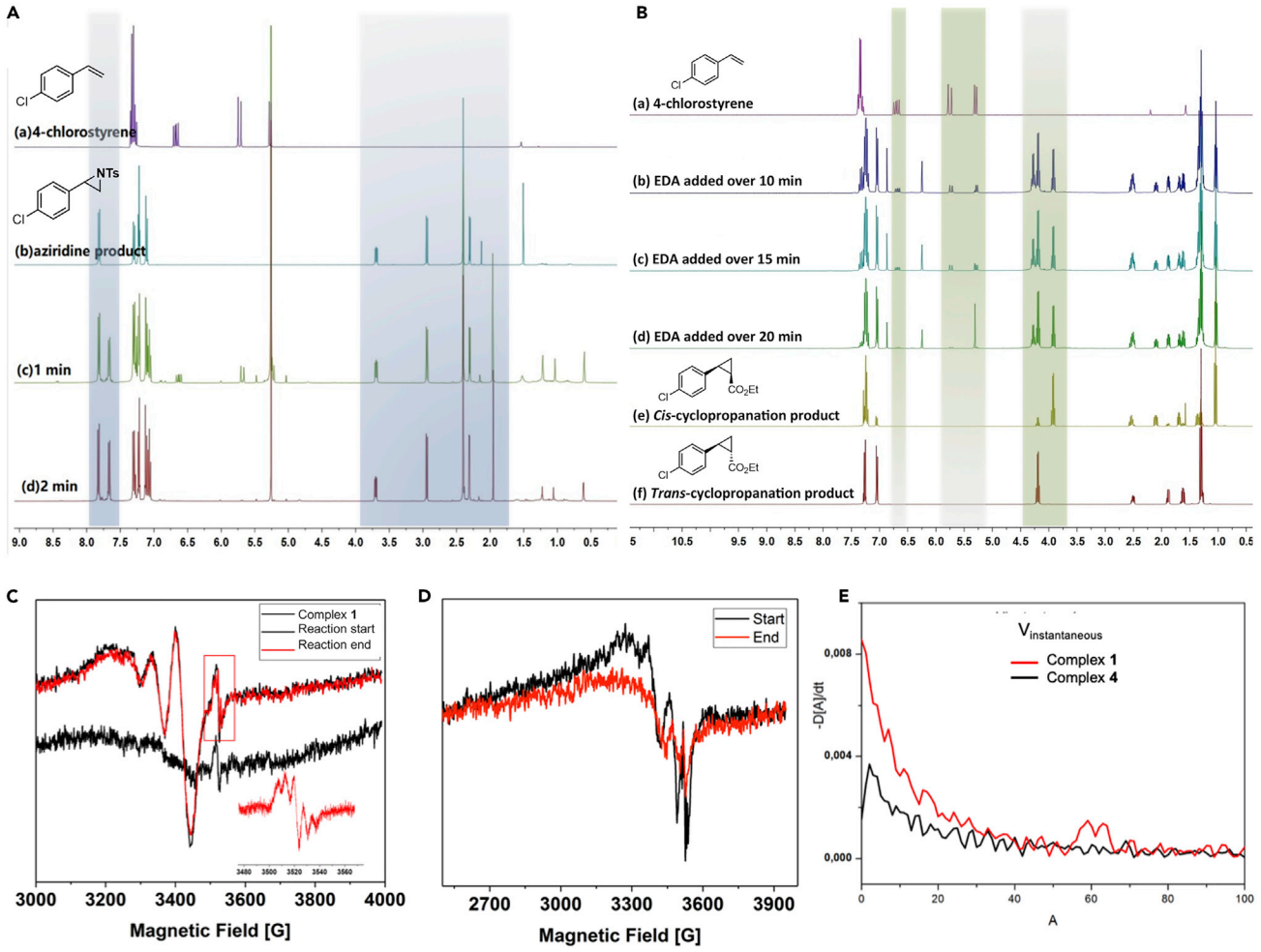

Figure 3. Spectroscopic Investigations of Reaction Mechanism

Operando ^{1}H NMR and EPR studies for aziridination (A and C) and cyclopropanation (B and D) of 4-chlorostyrene with complex **1** and kinetic UV-vis studies for aziridination of trans-chalcone with complexes **1** and **4** (E).

nitrene part upon coordination and are consistent with the ^{1}H NMR monitoring of the reaction showing completion of the reaction in 2 min. Operando EPR studies attempted on the cyclopropanation reaction were not conclusive as the experimental conditions implying slow addition of EDA could not be reproduced under operando conditions (Figure 3D). Following the reaction by UV-vis spectroscopy on trans-chalcone as substrate showed an initial instantaneous reaction rate at least two times higher using complex **1** compared with complex **4** (Figures 3E and Figures S20–S22). This initial rate enhancement can be directly related to the difference in geometries of the two complexes and points toward a behavior similar to the entatic state, defined as a reactivity improvement arising from strong steric distortion induced by ligands in a metal complex.

In light of our combined mechanistic studies, the following general mechanistic scheme can be proposed (Scheme 3). Insertion of the nitrene or carbene group on starting complex **1** generates intermediates **36a-b** (both detected by high-resolution mass spectroscopy [HRMS]), in which the high coordinative strain and torsion angles in complex **1** are released upon reactive group coordination. Intermediates **36a-b** subsequently undergo alkene insertion to yield species **37a-b** (Figure S115 and Table S15) and release the group-transfer product upon ring closure. DFT calculations (Figure 4) conducted on intermediate **36a** show that one singly occupied molecular orbital (SOMO) is perfectly aligned with the Cu-nitrene axis, which reflects the presence of an unpaired electron occupying a metal-based orbital having a Cu $3d_{z^2}$ character. The other SOMO appears mainly distributed over the N-SO_2 group confirming the formation of a nitrene

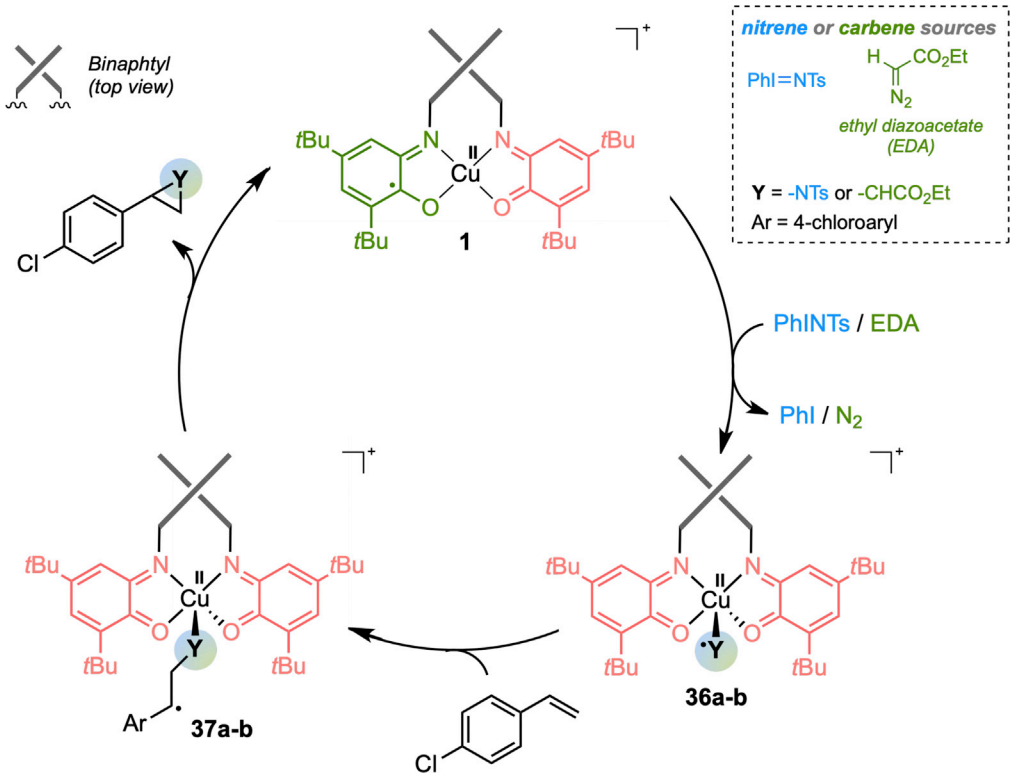

Scheme 3. Proposed Catalytic Cycle for N- and C-Group Transfer Reactions with Complex 1
a: Y = -NTs, b: Y = -$CHCO_2Et$.

radical moiety (Figures S115 and S116). This supports the triplet ground spin state of **36a** due to the orthogonal character of the two SOMOs preventing magnetic coupling as observed by EPR spectroscopy. When looking at the electronic structure of **37a**, we observe that the nature of the first SOMO remains metal centered, whereas the second SOMO is now a delocalized π-orbital distributed over the styrene moiety with the spin density being displaced from the nitrogen to the aryl group upon styrene insertion (Figures S117 and S118). DFT calculations conducted on intermediate **36b** reveal that one SOMO features a dominant Cu-character and the other one is a ligand-based orbital almost exclusively centered on the carbon atom of the -$CHCO_2Et$ ligand, which supports the formation of a carbene adduct (Figures S119 and S120). Upon styrene insertion on **36b**, the spin density is shifted toward the carbon center adjacent to the aryl group and the two SOMOs of **37b** appear similar to those of **37a** with one SOMO being metal centered and the other one being ligand based delocalized on the styrene moiety (Figures S121 and S122). Interestingly, a ΔΔG calculation comparing the relative stability of the species obtained upon nitrene and alkene insertion on strained and unstrained complexes **1** and **4** shows that intermediates **36a** and **37a** are stabilized by 2.5 and 7.1 $kcal.mol^{-1}$, respectively, in the case of complex **1** compared with complex **4** (Tables S16 and S17). These findings highlight the energetic gain observed when using the strained BINap ligand instead of the unstrained SQ and also reflect that the highly distorted structure induced by coordination of this ligand to the metal center facilitates insertion reactions. Comparison of catalytic efficiency shows that complex **1** compares well with other reported catalytic systems in terms of both reaction time and yield (Table S18).

In conclusion, this report combines the entatic reactivity model and redox cofactors, which are staples of metalloenzymes' reactivity toolbox, for enhanced group-transfer catalytic transformations. We have demonstrated that an atropisomeric tetratopic redox-active ligand imposing high steric and coordinative strain on a copper center can perform group transfer reactions up to eight times faster than related unstrained systems. The redox-active atropisomeric backbone establishes electronic communication between the two redox-active subunits, thus favoring intramolecular electron transfer during catalysis and maintaining a Cu^{II} redox homeostasis. This system bridges the gap between small-molecule enzymatic

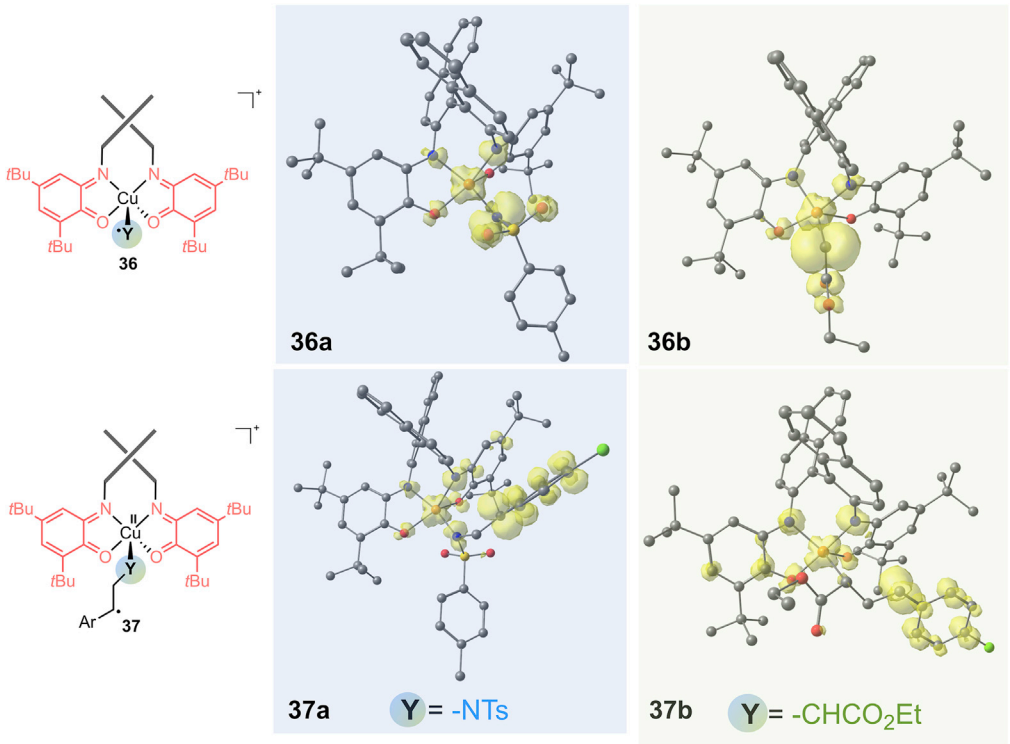

Figure 4. DFT-Calculated Spin Density Plots for Intermediates 36a-b and 37a-b

structural models focused on the design of the first coordination sphere and top-down approaches achieving control over the amino acid secondary and tertiary coordination spheres by directed enzymatic evolution (Arnold, 2017; Farwell et al., 2015; Coelho et al., 2013; Knight et al., 2018). This work shows that the combination of enzymatic reactivity-enabling strategies offers a promising approach to reactivity control in bioinspired catalysis and should open the door toward more challenging synthetic reactions.

Limitations of the Study

Enantioselective catalysis could not be achieved with this system. Furthermore, the cyclopropanation procedure requires addition of ethyldiazoacetate through syringe pump over a set period of time as to avoid dimerization of the carbene source.

METHODS

All methods can be found in the accompanying Transparent Methods supplemental file.

DATA AND CODE AVAILABILITY

The accession number for the compounds **1** and **2** reported in this paper is CCDC 1906978 and 1906977 (**1**, C2/c and P1 forms) and 1908272 (**2**). These data are provided free of charge by The Cambridge Crystallographic Data Centre.

SUPPLEMENTAL INFORMATION

Supplemental Information can be found online at https://doi.org/10.1016/j.isci.2020.100955.

ACKNOWLEDGMENTS

The authors would like to thank Sorbonne Université (SU), Université de Strasbourg, CNRS, IR-RPE CNRS FR3443 RENARD network (CW X-band EPR with Dr. J.-L. Cantin, INSP UMR CNRS 7588, SU and X-band EPR in Lille). SU is acknowledged for an Emergence grant (M.D.-E.M. and K.C.) and CSC for a PhD fellowship (Y.R.). The authors gratefully acknowledge the COST Action 27 CM1305 ECOSTBio and FrenchBIC

network. We would also like to thank Dr Vincent Lebrun, CNRS, Université de Strasbourg, for valuable discussions.

AUTHOR CONTRIBUTIONS

Y.R. synthesized and purified the compounds, collected and analyzed synthetic and analytical data, and performed catalytic experiments and reaction scopes; J.F. performed the X-ray crystallographic analysis; K.C. performed synthetic work and UV-vis studies and analyzed the data; N.V. performed the chiral HPLC studies; L.F. analyzed the data and commented on the manuscript; H.V. performed the operando EPR studies, analyzed the data, and wrote the manuscript; M.O. performed the DFT studies, analyzed the data, and wrote the manuscript; S.B. performed electrochemical and EPR experiments, analyzed the data, and wrote the manuscript; M.D.-E.M. designed the study, analyzed the data, and wrote the manuscript. All authors contributed to the analysis of the results and commented on the manuscript.

DECLARATION OF INTERESTS

The authors declare no competing interests.

Received: September 24, 2019
Revised: January 14, 2020
Accepted: February 25, 2020
Published: March 27, 2020

REFERENCES

Adesina, O., Anzai, I.A., Avalos, J.L., and Barstow, B. (2017). Embracing biological solutions to the sustainable energy challenge. Chem *2*, 20–51.

Albold, U., Hoyer, C., Neuman, N.I., Sobottka, S., Hazari, A.S., Lahiri, G.K., and Sarkar, B. (2019). Isolable Cu(I) complexes of extremely electron-poor, completely unreduced o-Quinone and "Di-o-Quinone" ligands stabilized through π–π interactions in the secondary coordination sphere. Inorg. Chem. *58*, 3754–3763.

Arnold, F.H. (2017). Directed evolution: bringing new chemistry to life. Angew. Chem. Int. Ed. *57*, 4143–4148.

Blanchard, S., Derat, E., Desage-El Murr, M., Fensterbank, L., Malacria, M., and Mouries-Mansuy, V. (2012). Non-innocent ligands: new opportunities in iron catalysis. Eur. J. Inorg. Chem. 376–389, https://doi.org/10.1002/ejic.201100985.

Broere, D.L.J., Plessius, R., and van der Vlugt, J.I. (2015). New avenues for ligand-mediated processes – expanding metal reactivity by the use of redox-active catechol, o-aminophenol and o-phenylenediamine ligands. Chem. Soc. Rev. *44*, 6886–6915.

Chaudhuri, P., Hess, M., Flörke, U., and Wieghardt, K. (1998). From structural models of Galactose oxidase to homogeneous catalysis: efficient aerobic oxidation of alcohols. Angew. Chem. Int. Ed. *37*, 2217–2220.

Chaudhuri, P., Verani, C.N., Bill, E., Bothe, E., Weyhermüller, T., and Wieghardt, K. (2001). Electronic structure of Bis(o-iminobenzosemiquinonato)metal complexes (Cu, Ni, Pd). The art of establishing physical oxidation states in transition-metal complexes containing radical ligands. J. Am. Chem. Soc. *123*, 2213–2223.

Chirik, P.J., and Wieghardt, K. (2010). Radical ligands confer nobility on base-metal catalysts. Science *327*, 794–795.

Coelho, P.S., Brustad, E.M., Kannan, A., and Arnold, F.H. (2013). Olefin cyclopropanation via carbene transfer catalysed by engineered cytochrome P450 enzymes. Science *339*, 307–310.

Comba, P. (2000). Coordination compounds in the entatic state. Coord. Chem. Rev. *200–202*, 217–245.

Comba, P., Fukuzumi, S., Koke, C., Martin, B., Löhr, A.M., and Straub, J. (2016). A bispidine iron(IV)–Oxo complex in the entatic state. Angew. Chem. Int. Ed. *55*, 11129–11133.

Corona, T., Ribas, L., Rovira, M., Farquhar, E.R., Ribas, X., Ray, K., and Company, A. (2016). Characterization and reactivity studies of a terminal copper–nitrene species. Angew. Chem. Int. Ed. *55*, 14005–14008.

Davidson, V.L. (2018). Protein-derived cofactors revisited: empowering amino acid residues with new functions. Biochemistry *57*, 3115–3125.

Dicke, B., Hoffmann, A., Stanek, J., Rampp, M.S., Grimm-Lebsanft, B., Biebl, F., Rukser, D., Maerz, B., Göries, D., Naumova, M., et al. (2018). Transferring the entatic-state principle to copper photochemistry. Nat. Chem. *10*, 355–362.

Dzik, W.I., Xu, X., Zhang, X.P., Reek, J.N.H., and de Bruin, B. (2010). 'Carbene radicals' in Co^{II}(por)-catalyzed olefin cyclopropanation. J. Am. Chem. Soc. *132*, 10891–10902.

Dzik, W.I., Zhang, X.P., and de Bruin, B. (2011). Redox noninnocence of carbene ligands: carbene radicals in (catalytic) C−C bond formation. Inorg. Chem. *50*, 9896–9903.

Farwell, C.C., Zhang, R.K., McIntosh, J.A., Hyster, T.K., and Arnold, F.H. (2015). Enantioselective enzyme-catalyzed aziridination enabled by active-site evolution of a Cytochrome P450. ACS Cent. Sci. *1*, 89–93.

Freiberger, M.I., Guzovsky, A.B., Wolynes, P.G., Parra, R.G., and Ferreiro, D.U. (2019). Local frustration around enzyme active sites. Proc. Natl. Acad. Sci. U S A *116*, 4037–4043.

Fujita, D., Sugimoto, H., Morimoto, Y., and Itoh, S. (2018). Noninnocent ligand in Rhodium(III)-Complex-Catalyzed C–H bond amination with tosyl azide. Inorg. Chem. *57*, 9738–9747.

Garcia, L., Cisnetti, F., Gillet, N., Guillot, R., Aumont-Nicaise, M., Piquemal, J.P., Desmadril, M., Lambert, F., and Policar, C. (2015). Entasis through hook-and-loop fastening in a glycoligand with cumulative weak forces stabilizing Cu^{I}. J. Am. Chem. Soc. *137*, 1141–1146.

Goswami, M., Lyaskovskyy, V., Domingos, S.R., Buma, W.J., Woutersen, S., Troeppner, O., Ivanović-Burmazović, I., Lu, H., Cui, X., Zhang, X.P., et al. (2015). Characterization of porphyrin-Co(III)-'Nitrene radical' species relevant in catalytic nitrene transfer reactions. J. Am. Chem. Soc. *137*, 5468–5479.

Grützmacher, H. (2008). Cooperating ligands in catalysis. Angew. Chem. Int. Ed. *47*, 1814–1818.

Hoffmann, A., Binder, S., Jesser, A., Haase, R., Flörke, U., Gnida, M., Salomone Stagni, M., Meyer-Klaucke, W., Lebsanft, B., Grünig, L.E., et al. (2013). Catching an entatic state—a pair of copper complexes. Angew. Chem. Int. Ed. *53*, 299–304.

Jacquet, J., Blanchard, S., Derat, E., Desage-El Murr, M., and Fensterbank, L. (2016a). Redox-ligand sustains controlled generation of CF_3 radicals by well-defined copper complex. Chem. Sci. *7*, 2030–2036.

Jacquet, J., Chaumont, P., Gontard, G., Orio, M., Vezin, H., Blanchard, S., Desage-El Murr, M., and Fensterbank, L. (2016b). C−N bond formation from a masked high-valent copper complex stabilized by redox non-innocent ligands. Angew. Chem. Int. Ed. *55*, 10712–10716.

Jacquet, J., Cheaib, K., Ren, Y., Vezin, H., Orio, M., Blanchard, S., Fensterbank, L., and Desage-El Murr, M. (2017). Circumventing intrinsic metal reactivity: radical generation with redox-active ligands. Chemistry *23*, 15030–15034.

Kaim, W. (2011). Manifestations of noninnocent ligand behavior. Inorg. Chem. *50*, 9752–9765.

Knight, A.M., Kan, S.B.J., Lewis, R.D., Brandenberg, O.F., Chen, K., and Arnold, F.H. (2018). Diverse engineered heme proteins enable stereodivergent cyclopropanation of unactivated alkenes. ACS Cent. Sci. *4*, 372–377.

Kuijpers, P., van der Vlugt, J.I., Schneider, S., and de Bruin, B. (2017). Nitrene radical intermediates in catalytic synthesis. Chemistry *23*, 13819–13829.

Luca, O.R., and Crabtree, R.H. (2012). Redox-active ligands in catalysis. Chem. Soc. Rev. *42*, 1440–1459.

Lyaskovskyy, V., and de Bruin, B. (2012). Redox non-innocent ligands: versatile new tools to control catalytic reactions. ACS Catal. *2*, 270–279.

Malachowski, M.R., Adams, M., Elia, N., Rheingold, A.L., and Kelly, R.S. (1999). Enforcing geometrical constraints on metal complexes using biphenyl-based ligands: spontaneous reduction of copper(II) by sulfur-containing ligands. J. Chem. Soc. Dalton Trans. 2177–2182.

Mara, M.W., Hadt, R.G., Reinhard, M.E., Kroll, T., Lim, H., Hartsock, R.W., Alonso-Mori, R., Chollet, M., Glownia, J.M., Nelson, S., et al. (2017). Metalloprotein entatic control of ligand-metal bonds quantified by ultrafast x-ray spectroscopy. Science *356*, 1276–1280.

Mukherjee, C., Weyhermüller, T., Bothe, E., and Chaudhuri, P. (2008). Targeted oxidase reactivity with a new redox-active ligand incorporating N2O2 Donor atoms. Complexes of Cu(II), Ni(II), Pd(II), Fe(III), and V(V). Inorg. Chem. *47*, 11620–11632.

Müller, E., Bernardinelli, G., and Reedijk, J. (1996). 2,2′-Bis(3-(2-pyridyl)-1-methyltriazolyl)biphenyl: A tetracoordinating wrapping ligand inducing similar Skew coordination geometries at copper(I) and copper(II). Inorg. Chem. *35*, 1952–1957.

Müller, E., Piguet, C., Bernardinelli, G., and Williams, A.F. (1988). 2,2′-Bis(6-(2,2′-bipyridyl)) biphenyl (TET), a sterically constricted tetradentate ligand: structures and properties of its complexes with copper(I) and copper(II). Inorg. Chem. *27*, 849–855.

Praneeth, V.K.K., Ringenberg, M.R., and Ward, T.R. (2012). Redox-active ligands in catalysis. Angew. Chem. Int. Ed. *51*, 10228–10234.

Ren, Y., Cheaib, K., Jacquet, J., Vezin, H., Fensterbank, L., Orio, M., Blanchard, S., and Desage-El Murr, M. (2018). Copper-catalyzed aziridination with redox-active ligands: molecular spin catalysis. Chemistry *24*, 5086–5090.

Rudroff, F., Mihovilovic, M.D., Gröger, H., Snajdrova, R., Iding, H., and Bornscheuer, U. (2018). Opportunities and challenges for combining chemo- and biocatalysis. Nat. Catal. *1*, 12–22.

Schrempp, D.F., Leingang, S., Schnurr, M., Kaifer, E., Wadepohl, H., and Himmel, H.J. (2017). Inter- and intramolecular electron transfer in copper complexes: electronic entatic state with redox-active guanidine ligands. Chemistry *23*, 13607–13611.

Snyder, B.E.R., Vanelderen, P., Bols, M.L., Hallaert, S.D., Böttger, L.H., Ungur, L., Pierloot, K., Schoonheydt, R.A., Sels, B.F., and Solomon, E.I. (2016). The active site of low-temperature methane hydroxylation in iron-containing zeolites. Nature *536*, 317–321.

Stanek, J., Hoffmann, A., and Herres-Pawlis, S. (2018). Renaissance of the entatic state principle. Coord. Chem. Rev. *365*, 103–121.

Stanek, J., Sackers, N., Fink, F., Paul, M., Peters, L., Grunzke, R., Hoffmann, A., and Herres-Pawlis, S. (2017). Copper guanidinoquinoline complexes as entatic state models of electron-transfer proteins. Chemistry *23*, 15738–15745.

Stubbe, J., and van der Donk, W.A. (1998). Protein radicals in enzyme catalysis. Chem. Rev. *98*, 705–762.

Suarez, A.I.O., Lyaskovskyy, V., Reek, J.N.H., van der Vlugt, J.I., and de Bruin, B. (2013). Complexes with nitrogen-centered radical ligands: classification, spectroscopic features, reactivity, and catalytic applications. Angew. Chem. Int. Ed. *52*, 12510–12529.

Vallee, B.L., and Williams, R.J. (1968). Metalloenzymes: the entatic nature of their active sites. Proc. Natl. Acad. Sci. U S A *59*, 498–505.

van der Vlugt, J.I. (2012). Cooperative catalysis with first-row late transition metals. Eur. J. Inorg. Chem. 363–375.

van der Vlugt, J.I. (2019). Radical-type reactivity and catalysis by single-electron transfer to or from redox-active ligands. Chemistry *25*, 2651–2662.

Wang, Y., DuBois, J.L., Hedman, B., Hodgson, K.O., and Stack, T.D.P. (1998). Catalytic Galactose oxidase models: biomimetic Cu(II)-Phenoxyl-Radical reactivity. Science *279*, 537–540.

Williams, R.J.P. (1971). Catalysis by metallo-enzymes: the entatic state. Inorg. Chim. Acta Rev. *5*, 137–155.

Williams, R.J.P. (1995). Energised (entatic) states of groups and of secondary structures in proteins and metalloproteins. Eur. J. Biochem. *234*, 363–381.

iScience, Volume *23*

Supplemental Information

Optimizing Group Transfer Catalysis by Copper Complex with Redox-Active Ligand in an Entatic State

Yufeng Ren, Jeremy Forté, Khaled Cheaib, Nicolas Vanthuyne, Louis Fensterbank, Hervé Vezin, Maylis Orio, Sébastien Blanchard, and Marine Desage-El Murr

SUPPLEMENTAL INFORMATION

Transparent methods

Transparent methods

General Information

All reactions were performed under argon atmosphere, in flame dried glassware with magnetic stirring using standard Schlenk techniques, unless otherwise mentioned. MeCN and CH_2Cl_2 were distilled over calcium hydride and were purged with argon prior to use. All other reagents were purchased from commercial sources (Sigma-Aldrich, Alfa Aesar, Fluorochem, Strem Chemicals) and were used without purification, unless otherwise noted. Thin layer chromatography (TLC) was performed on Merck 60 F254 silica gel and visualized with a UV lamp (254 nm) or with a potassium permanganate solution. ^{1}H NMR and ^{13}C NMR spectra were recorded at room temperature unless otherwise required on a Bruker Avance 300 MHz or a Bruker Avance 400 MHz spectrometer. Trimethoxybenzene was used as an internal standard to determine ^{1}H NMR yield. Shifts (δ) are given in parts per million (ppm) and coupling constants (*J*) are given in Hertz (Hz). High-resolution mass spectrometry was performed on a BrukermicroTOF (ESI) spectrometer. UV-Vis-NIR was recorded using JASCO

V670 spectrophotometer or a Cary 5000 spectrophotometer (kinetic follow of the aziridination of *trans*-chalcone). Wavelengths (λ) are given in nanometer (nm) and molar extinction coefficients (ε) are given in $M^{-1}.cm^{-1}$. The circular dichroism was performed on a JASCOJ-815 CD spectrometer equipped with a JASCO CDF-426L Peltier thermostat (2 mm quartz cell). Preparative chiral HPLC of HELIXOL was achieved on an Agilent 1260 infinity unit with pump, autosampler, oven, DAD and JASCO CD-2095 circular dichroism detector, controlled by SRA Instrument software. X-band EPR spectra were recorded in non-saturating conditions on a Bruker ELEXSYS 500 spectrometer equipped with an Oxford instrument continuous-flow liquid-helium cryostat and a temperature control system. CW in situ experiments were performed using an X band ELEXSYS 500 E spectrometer. The spectra were measured at room temperature using a 2mm quartz cell. Microwave power and amplitude modulation were respectively set to 2 mW and 1 G. Cyclic voltammograms were recorded using OrigaFlex-Pack OGF500, and were performed in dichloromethane solutions containing 0.1 M $TBAPF_6$ as the supporting electrolyte at a glassy carbon working electrode, a KCl saturated calomel reference electrode, and a platinum wire as a counter electrode. X-Ray crystal structure determination: a single crystal was selected, mounted and transferred into a cold nitrogen gas stream. Intensity data was collected with a Bruker Kappa-APEX2 system using micro-source Cu-Kα radiation. Unit-cell parameters determination, data collection strategy and integration were carried out with the Bruker APEX2 suite of programs. Multi-scan absorption correction was applied. The structure was solved with SHELXS-86 and refined anisotropically by full-matrix least-squares methods using CRYSTALS. Structures were deposited at the International Union of Crystallography and can be obtained free of charge via checkcif.iucr.org

Synthesis and characterization of H_4BINap ligand 2

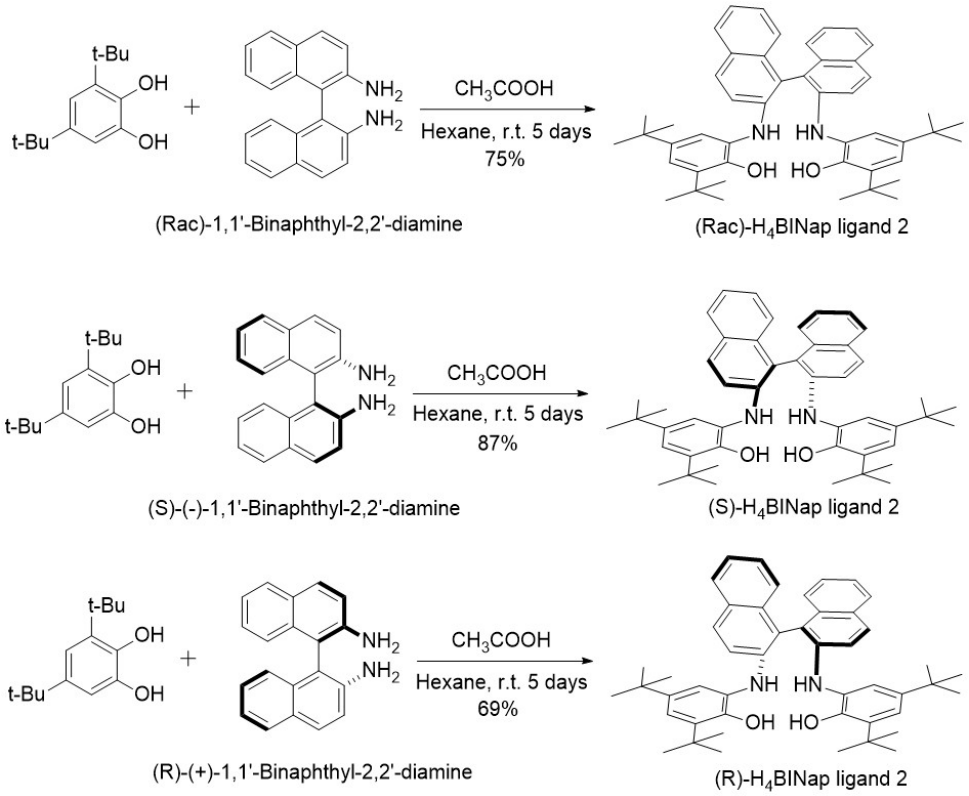

Scheme S1. Synthesis of ligand **2**, related to Figure 2.

A 100 mL round bottomed flask with stirrer bar was charged with 1,1'-binaphthyl-2,2'-diamine (1.136 g, 4 mmol) and 3,5-di-*tert*-butylcatechol (1.776 g, 8 mmol). Hexane (40 mL) was added and 0.2 mL glacial acetic acid was added after 10 minutes. The reaction was stirred for 5 days at room temperature. The reaction mixture was filtered to remove the precipitate and the filtrate was evaporated under reduced pressure to afford the crude product. Recrystallization in acetonitrile provided the final product as a pale white powder. (Procedure adapted from the literature)[1]

^{1}H NMR (400 MHz, $CDCl_3$) δ = 7.88 – 7.81 (m, 4H), 7.38 – 7.27 (m, 6H), 7.18 (d, *J*=2.4, 2H), 7.04 (d, *J*=9.0, 2H), 6.91 (d, *J*=2.4, 2H), 6.43 (s, 2H), 1.40 (s, 18H), 1.20 (s, 18H).

^{13}C NMR (101 MHz, $CDCl_3$) δ = 149.7, 144.0, 142.3, 135.4, 133.5, 130.1, 129.3, 128.5, 127.9, 127.3, 123.9, 123.6, 122.3, 122.0, 116.9, 114.6, 34.9, 34.3, 31.5, 29.5.

HRMS (ESI) calculated for $C_{48}H_{56}N_2O$ 692.4342, found $[M+Na]^+$ 715.4233.

[1] F. D. Lesh, R. L. Lord, M. J. Heeg, H. B. Schlegel, C. N. Verani, *Eur. J. Inorg. Chem.***2012**, 463–466.

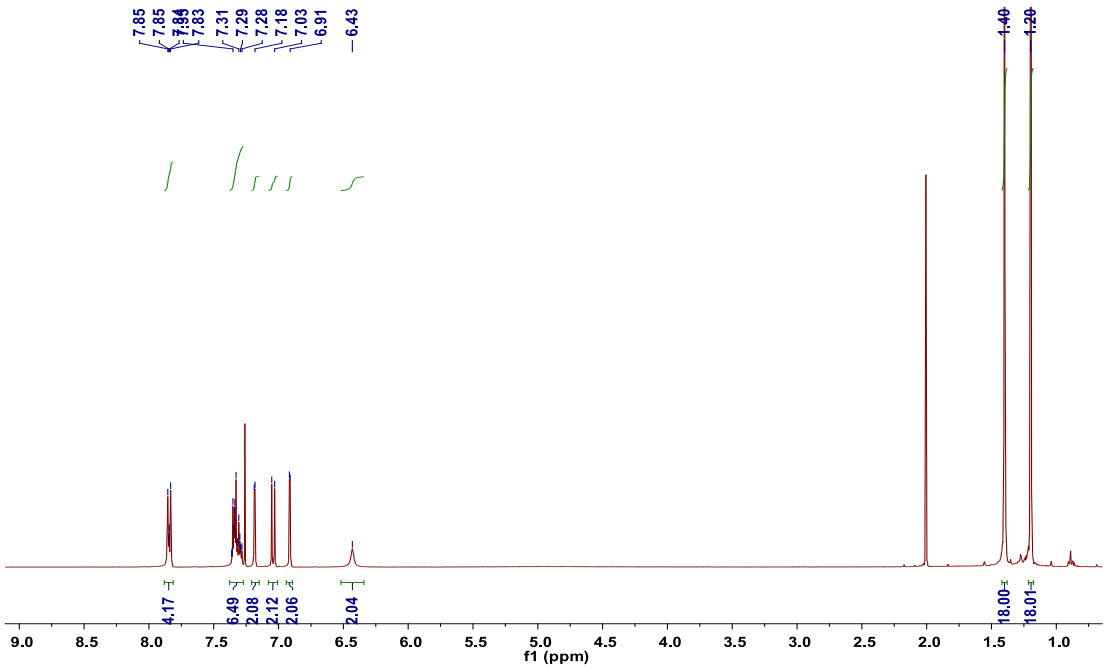

Figure S1. ^{1}H NMR spectrum of **2**, related to Figure 2.

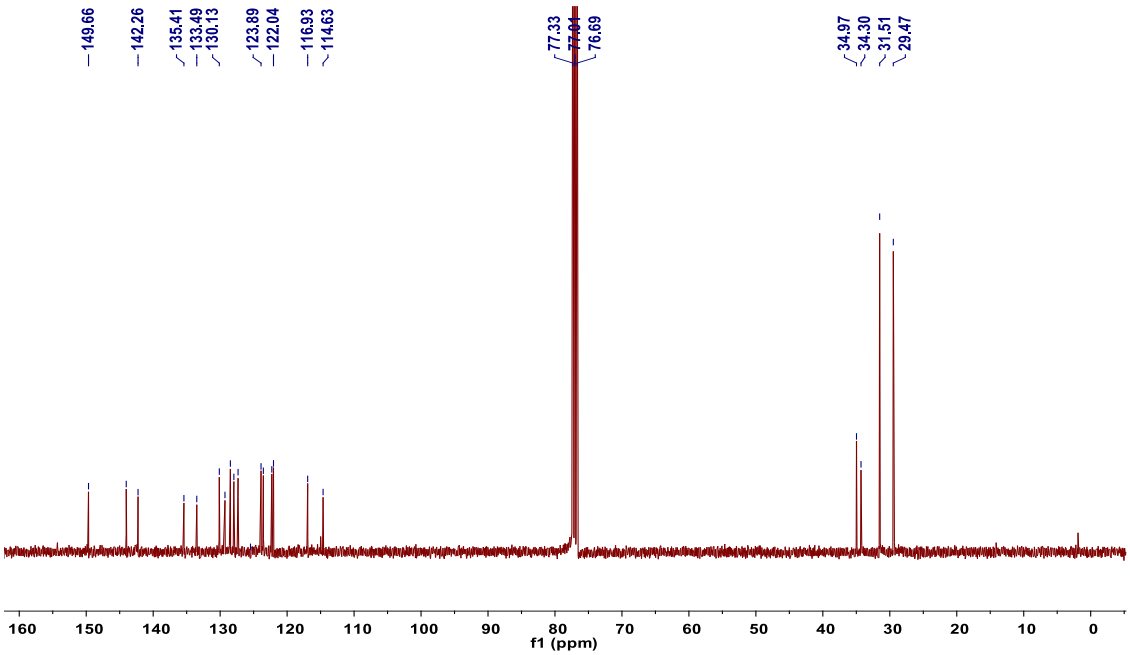

Figure S2. ^{13}C NMR spectrum of **2**, related to Figure 2.

Circular dichroism of H_4BINap ligand 2

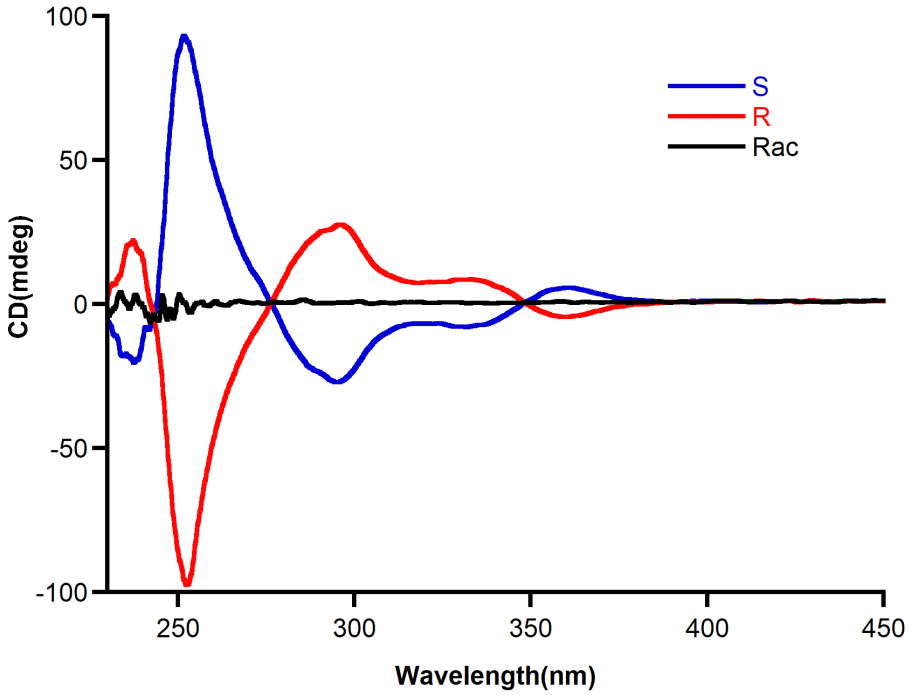

Figure S3. Circular dichroism spectra of enantiopure (R), (S), and racemic H_4BINap ligand **2** (c=0.3 mM) in DCM, related to Figure 2.

CD spectrum of S-ligand **2** (blue line) exhibits an intense positive band around (+) 251 nm, and a broad negative band at (-) 294 nm accompanied with a shoulder at 332 nm. CD spectrum of R-ligand **2** (red line) shows the opposite trend. It disclosed an intense negative band around (-) 252 nm, and a broad positive band at (+) 295 nm accompanied with a shoulder at 333 nm. CD spectrum of racemate-ligand **2** (black line) is almost a straight line, no absorption band.

Synthesis and characterization of [Cu(BINap-SQ_2)] 3

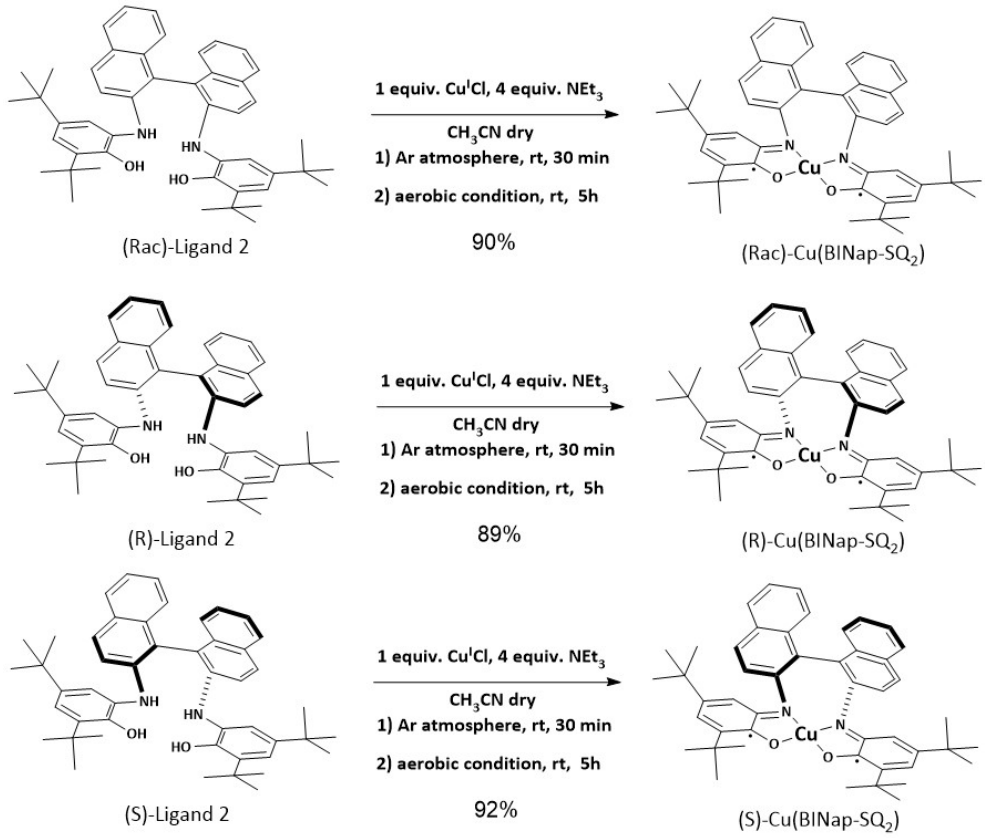

Scheme S2. Synthesis of complex [Cu(BINap-SQ_2)] **3**, related to Figure 2.

H_4BINap Ligand **2** (500 mg, 0.722 mmol, 1 equiv.) was introduced in a flame-dried schlenk, which was back-filled three times with argon. Degassed MeCN (30 mL) and Et_3N (0.4ml, 4 equiv.) were added at room temperature and the mixture was left to stir for 10 minutes. CuCl (71 mg, 0.722 mmol, 1 equiv.) was added and the mixture was stirred for 30 minutes under argon. The resulting light green suspension was left to stir for 5 h under air at room temperature. The suspension turned dark green and the precipitate slowly disappeared. As the time went, a dark green precipitate appeared. The dark green complex was filtered and washed with cold acetonitrile. (Procedure adapted from the literature[2]).

HRMS (ESI) calculated for $C_{48}H_{52}CuN_2O_2$ 751.3325, found $[M]^+$ 751.34.

[2] C. Mukherjee, T. Weyhermüller, E. Bothe, P. Chaudhuri, *Inorg. Chem.* **2008**, 47, 11620-11632.

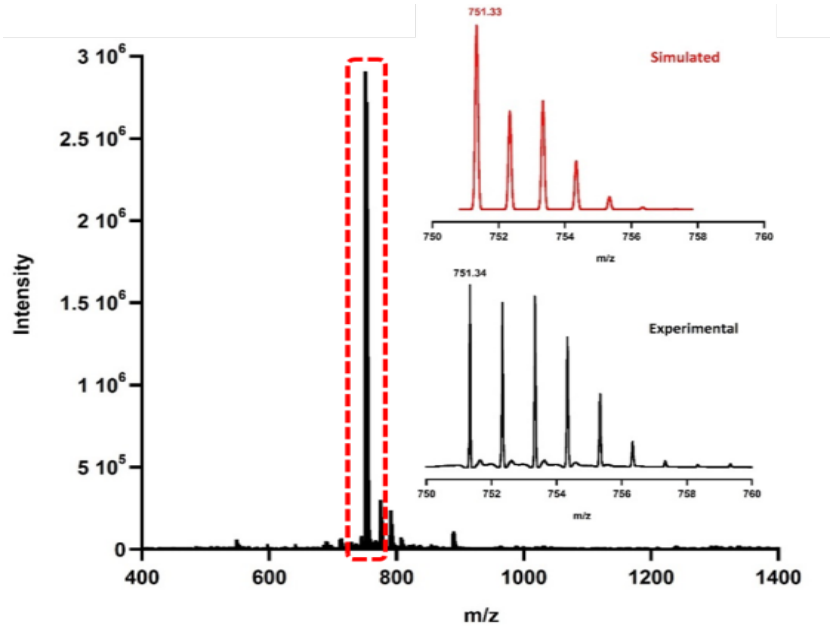

Figure S4. HRMS mass spectrum of [Cu(BINap-SQ_2)], related to Figure 2.

Circular dichroism study of [Cu(BINap-SQ_2)] 3

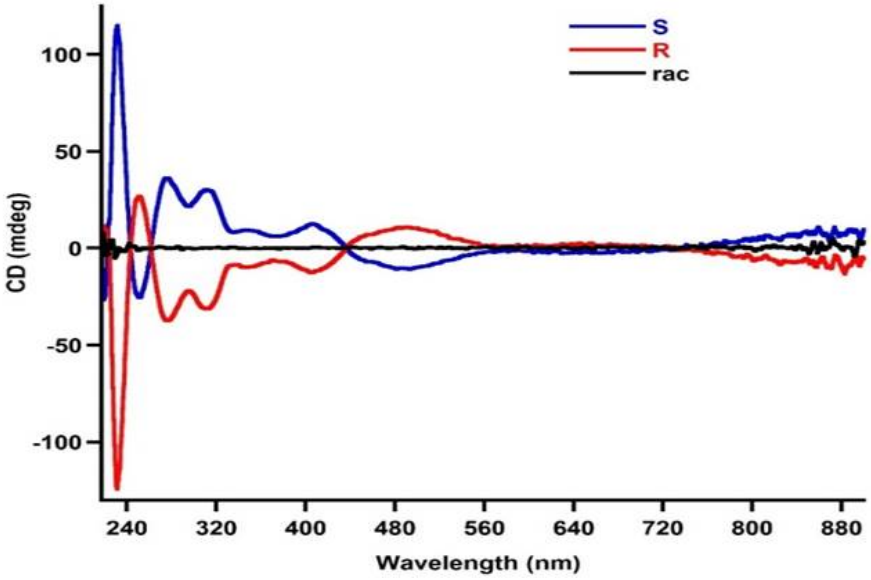

Figure S5. Circular Dichroism spectrum of [Cu(BINap-SQ_2)] (C=0.3 mM), related to Figure 2.

CD spectrum of S-[Cu(BINap-SQ_2)] (blue line) disclosed an intense positive band around (+) 231 nm, and a broad positive band with 4 shoulders at (+) 275, 310, 347 and 406 nm. Besides, it has two small negative bands at (-) 251 and 493 nm. The curve of R-[Cu(BINap-SQ_2)] (red line) is exactly the opposite and the strength of absorption bands are very similar with S-[Cu(BINap-SQ_2)]. CD spectrum of Racemate-[Cu(BINap-SQ_2)] (black line) is silence.

Figure S6. Chiral HPLC report of racemic [Cu(BINap-SQ_2)] **3**, related to Figure 2.

Sample name: Rac-[Cu(BINap-SQ_2)]
Column: Chiralpak IE
Temperature: 10 degres
Mobile phase: Heptane/dichloromethane (90/10), 1 mL/min

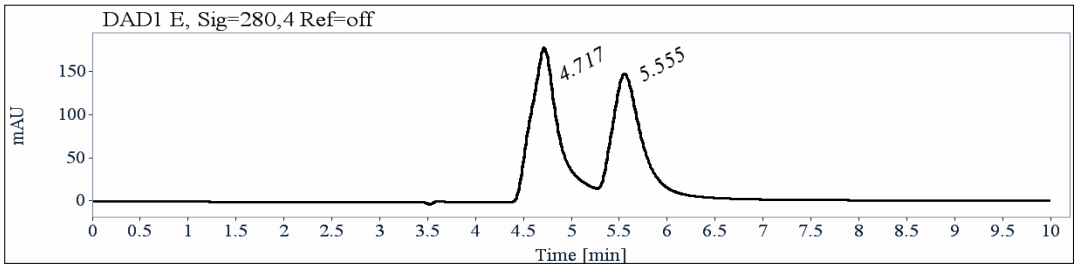

Signal: DAD1 E, Sig=280,4 Ref=off

RT [min]	Area	Area%	Capacity Factor	Enantioselectivity	Resolution (USP)
4.72	3659	52.70	0.60		
5.56	3284	47.30	0.88	1.47	1.56
Sum	6943	100.00			

Figure S7. Chiral HPLC report of S-[Cu(BINap-SQ_2)] **3**, related to Figure 2.

Sample name: S-[Cu(BINap-SQ_2)]
Column: Chiralpak IE
Temperature: 10 degres
Mobile phase: Heptane/dichloromethane (90/10), 1 mL/min

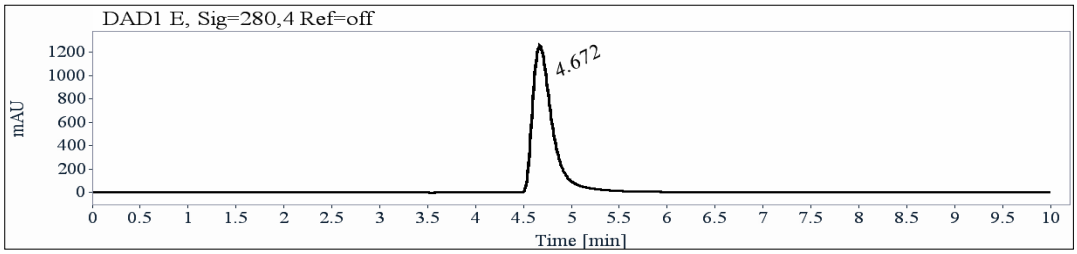

Signal: DAD1 E, Sig=280,4 Ref=off

RT [min]	Area	Area%	Capacity Factor	Enantioselectivity	Resolution (USP)
4.67	18470	100.00	0.58		
Sum	18470	100.00			

Figure S8. Chiral HPLC report of R-[Cu(BINap-SQ_2)] **3**, related to Figure 2.

Sample name: R-[Cu(BINap-SQ_2)]
Column: Chiralpak IE
Temperature: 10 degres
Mobile phase: Heptane/dichloromethane (90/10), 1 mL/min

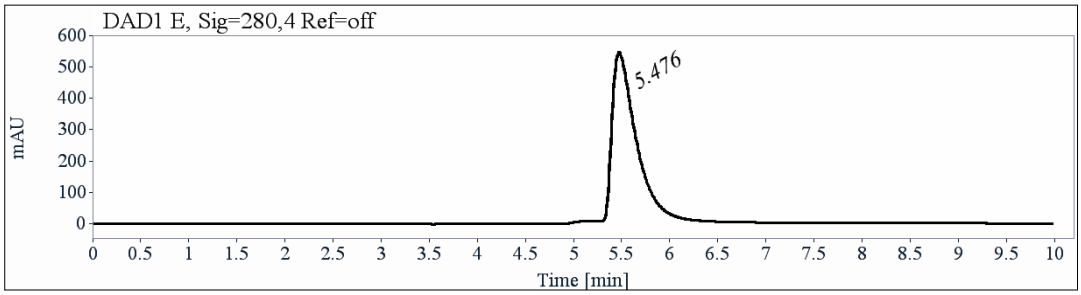

Signal: DAD1 E, Sig=280,4 Ref=off

RT [min]	Area	Area%	Capacity Factor	Enantioselectivity	Resolution (USP)
5.48	9944	100.00	0.86		
Sum	9944	100.00			

Cyclic voltammetry and redox potentials of [Cu(BINap-SQ_2)] 3

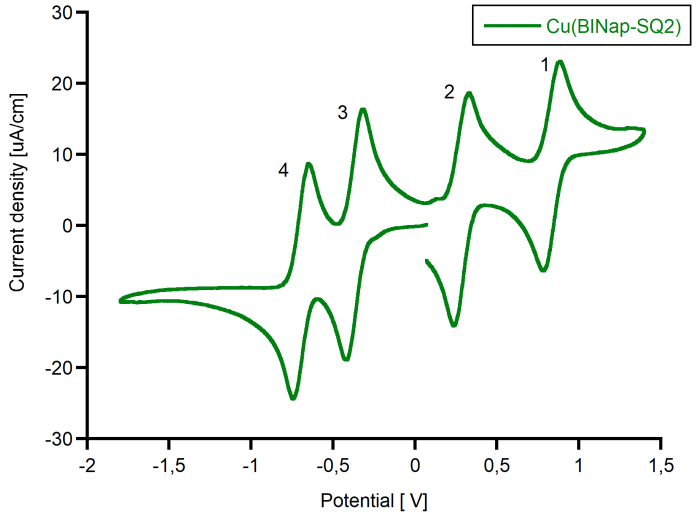

Figure S9. Cyclic voltammogram of [Cu(BINap-SQ_2)] (C=1.10^{-3}M) in a 0.1M $TBAPF_6/CH_2Cl_2$ electrolyte, scan rate: 100 mV/s, related to Figure 2.

Table S1. Summary of the redox potentials for the various waves of the CV of [Cu(BINap-SQ_2)], related to Figure 2.

Wave	Ep(red) V/SCE	Ep(ox) V/SCE	Ep(ox) - Ep(red)	½(Ep(ox)+Ep(red)) V/SCE
1	0.786	0.887	101 mV	0.84
2	0.237	0.333	96 mV	0.29
3	-0.415	-0.316	99 mV	-0.37
4	-0.745	-0.650	95 mV	-0.70

Table S2. Comparison of the half wave potentials of $Cu(SQ)_2$, $Cu(L_{Biphen}SQ_2)$ and $Cu(BINap\text{-}SQ_2)$. a) $E°_{Fc+/Fc}$ taken as +0.6V/SCE in DCM/ 0.1 $TBAPF_6$[3] related to Figure 2.

	½($E_p^{(ox)}$+E_p(red)) V/SCE[a]			
Compound	Wave 1	Wave 2	Wave 3	Wave 4
$Cu(SQ)_2$	0.97	0.34	-0.42	-0.72
$Cu(L_{Biphen}SQ_2)$	0.94	0.44	-0.06	-0.38
$Cu(BINap\text{-}SQ_2)$	0.84	0.29	-0.37	-0.70

CW X-band EPR study of [$Cu(BINap\text{-}SQ_2)$] 3

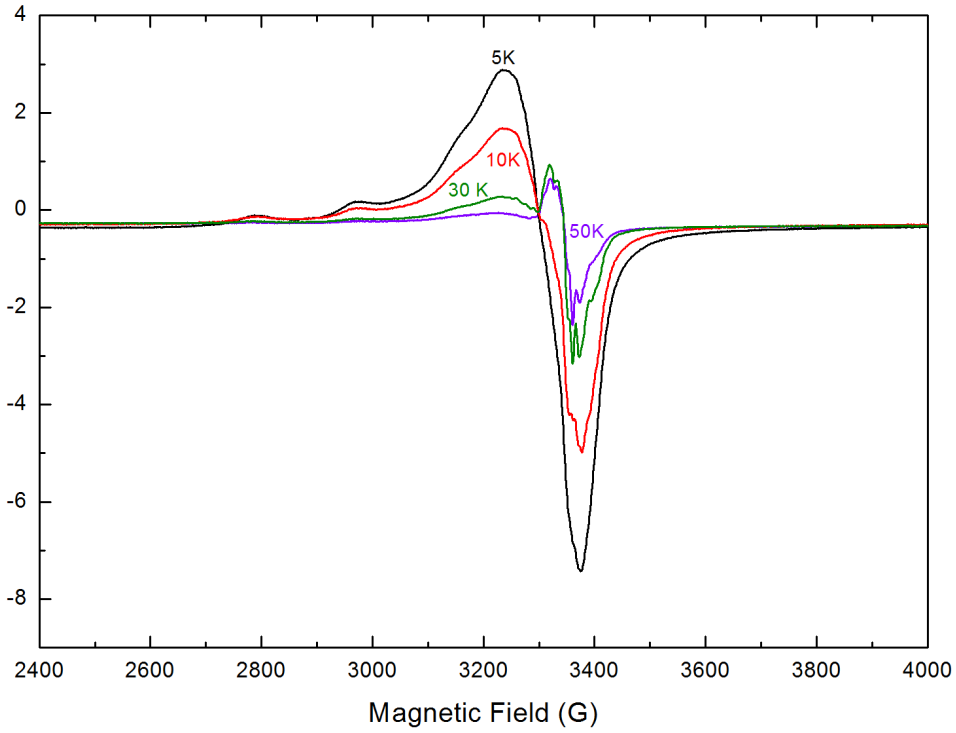

Figure S10. Temperature evolution (5K to 50K) of the X-band EPR spectrum of a 1 mM, frozen solution of [$Cu(BINap\text{-}SQ_2)$] **3** in dichloromethane. v=9.407GHz, 5G amplitude modulation, 0.2 mW power, related to Figure 2.

The 5K spectrum is in agreement with a Cu-based S=1/2 ground state (large g anisotropy). Change of the profile with T is indicative of the progressive population of excited states, in agreement with a three spin system involving Cu(II) and two radical ligands.

[3]: D. Bao, B. Millare, W. Xia, B. G. Steyer, A. A. Gerasimenko, A. Ferreira, A. Contreras, V. I. Vullev, *J. Phys. Chem. A* **2009**, *113*, 1259–1267)

^{1}H-NMR spectrum of [Cu(BINap-SQ_2)] 3

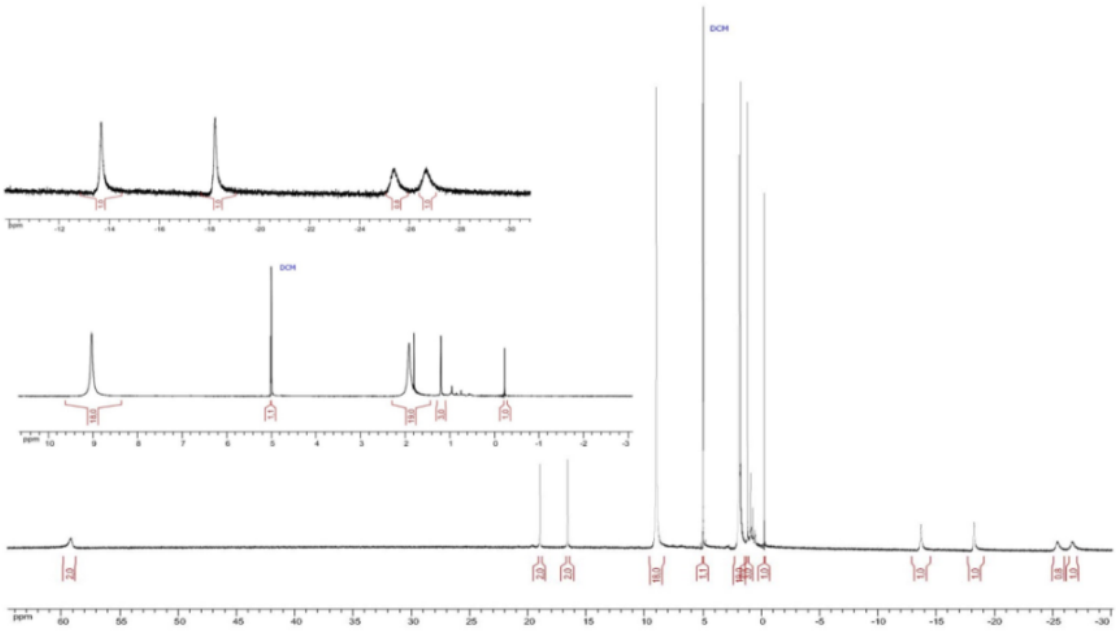

Figure S11. Paramagnetic ^{1}H-NMR spectrum of [Cu(BINap-SQ_2)] **5**, related to Figure 2.

Synthesis and characterization of $[Cu(BINap\text{-}BQ_2)]^{2+}$ 5

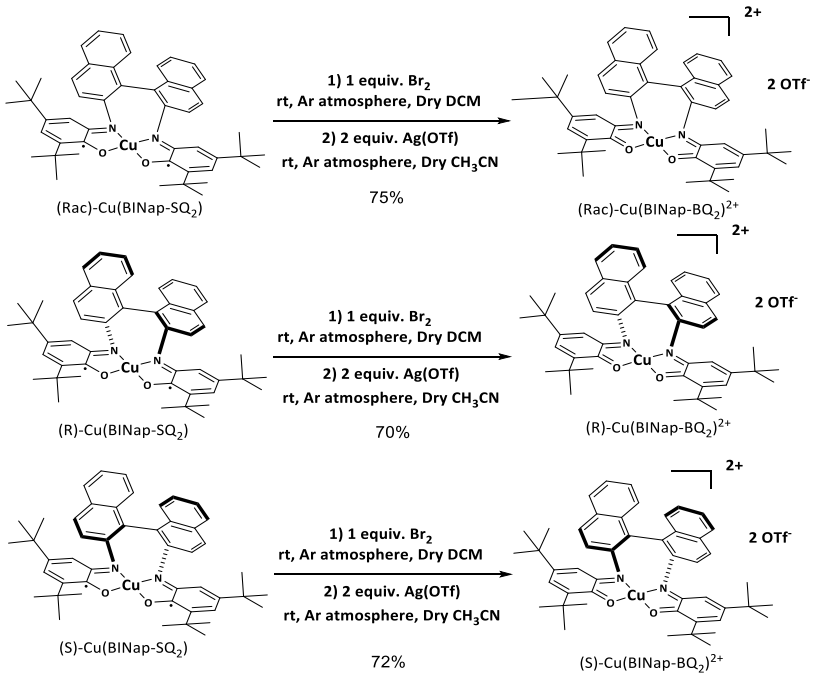

Scheme S3. Synthesis and characterization of $[Cu(BINap\text{-}BQ_2)]^{2+}$ **3**, related to Figure 2.

To flame-dried schlenk flask, was introduced [Cu(BINap-SQ_2)] complex (100 mg, 0.133 mmol, 1 equiv.). The flask was back-filled three times with argon and degassed CH_2Cl_2 (5 mL) was added. A 2.8 M solution of bromine in CH_2Cl_2 (47.5 µL, 0.133 mmol, 1 equiv.) was added dropwise and the resulting dark-red solution was stirred for 1 h at room temperature. The solution of silver triflate (71.8 mg, 0.28 mmol, 2 equiv.) in degassed MeCN was introduced into the schlenk flask under argon atmosphere. The resulting mixture was stirred for 10 minutes at room temperature. The suspension was filtered, and the filtrate was evaporated to a little solution left. Then the solution was added slowly to cold pentane to collect the dark brown precipitation.

Cyclic voltammetry and redox potentials of $[Cu(BINap\text{-}BQ_2)]^{2+}$ 5

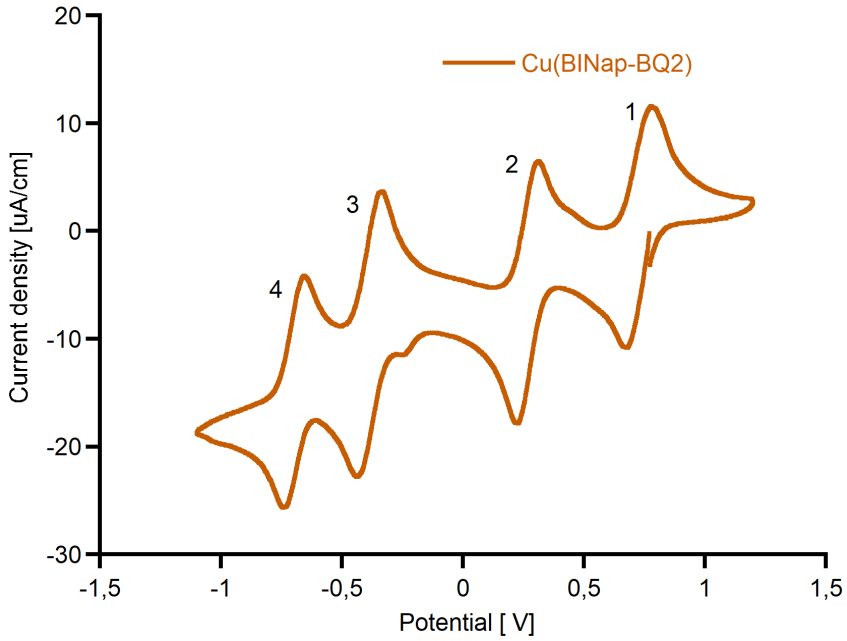

Figure S12. Cyclic voltammogram of $[Cu(BINap\text{-}BQ_2)]^{2+}$ ($C=1.10^{-3}M$) in a 0.1M $TBAPF_6/CH_2Cl_2$ electrolyte, scan rate: 100mV/s, related to Figure 2.

Table S3. Summary of the redox potentials for the various waves of the CV of $[Cu(BINap\text{-}BQ_2)]^{2+}$

Wave	Ep(red) V/SCE	Ep(ox) V/SCE	Ep(ox) - Ep(red)	½(Ep(ox)+Ep(red)) V/SCE
1	0.673	0.777	104 mV	0.73
2	0.220	0.315	95 mV	0.27
3	-0.437	-0.339	98 mV	-0.39
4	-0.746	-0.655	91 mV	-0.70

CW X-band EPR study of $[Cu(BINap\text{-}BQ_2)]^{2+}$ 5

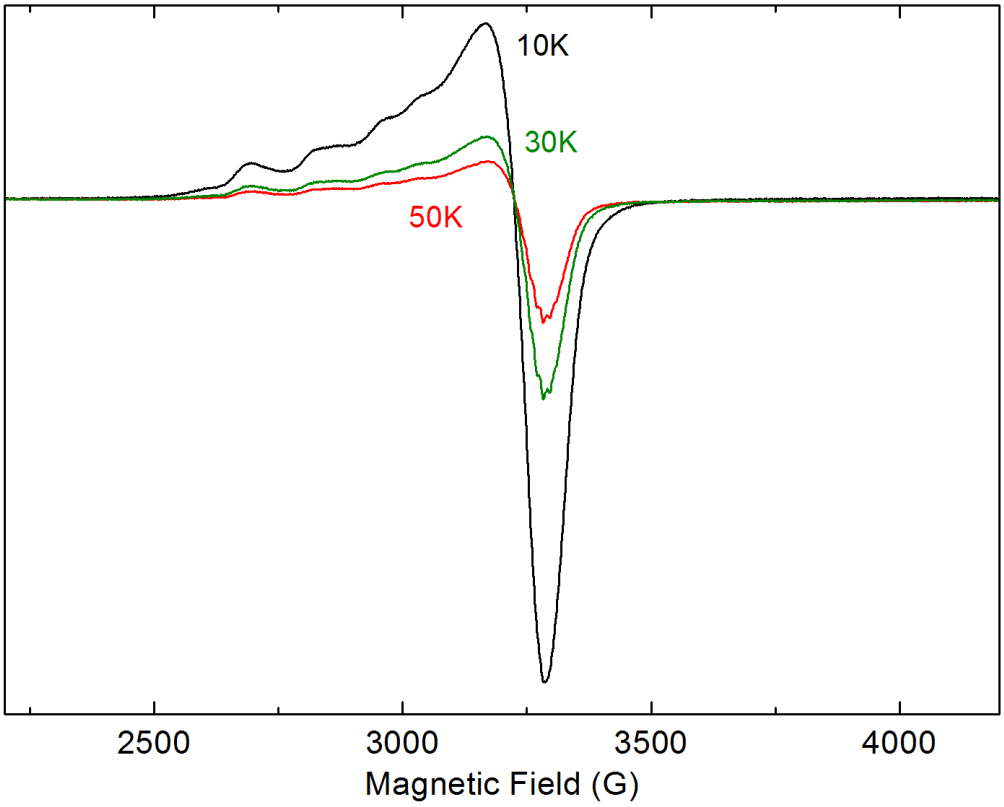

Figure S13. Temperature evolution (5K to 50K) of the X-band EPR spectrum of a 1 mM frozen solution of $[Cu(BINap\text{-}BQ_2)]$ in CH_2Cl_2. v=9.405GHz, 5G amplitude modulation, 0.04 mW power, related to Figure 2.

The temperature evolution of the spectrum is classical of the Curie law behavior of a pure S=1/2 system. The large anisotropy indicates that the spin density is essentially on the copper.

Synthesis and characterization of $[Cu(BINap\text{-}SQ\text{-}BQ)]^+$ 1

Method A:

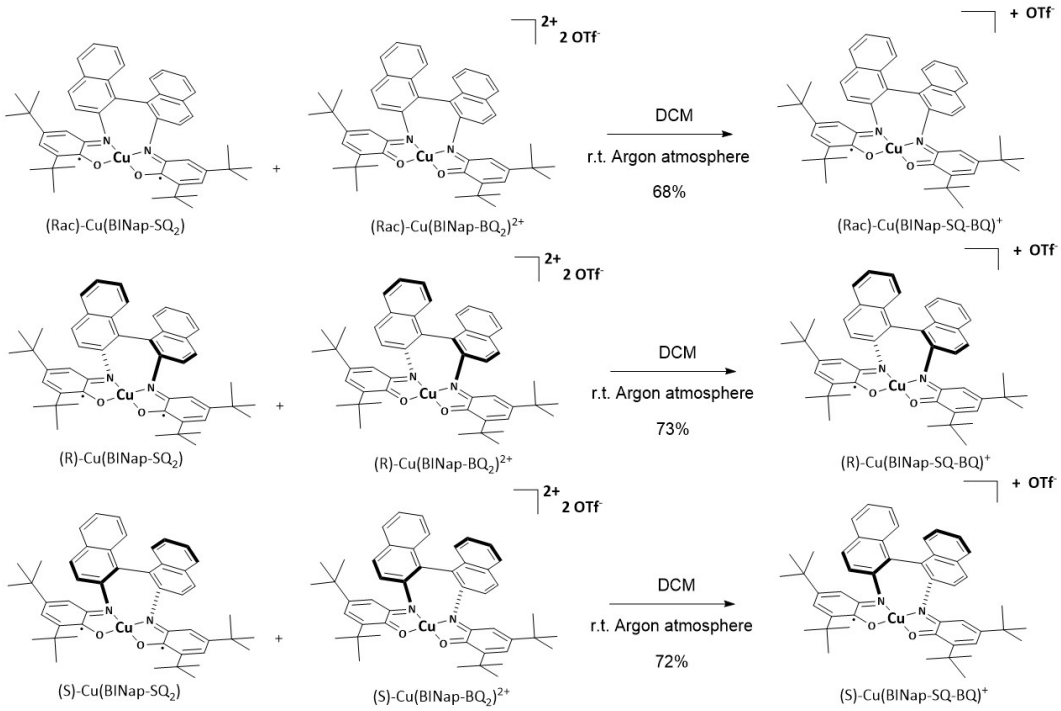

Scheme S4. Synthesis of complex $[Cu(BINap\text{-}SQ\text{-}BQ)]^+$ **1**, related to Figure 2.

To a schlenk flask, were introduced [Cu(BINap-SQ_2)] complex (50 mg, 0.066mmol, 1 equiv.) and $[Cu(BINap\text{-}BQ_2)]^{2+}$ complex (69.8 mg, 0.066 mmol, 1 equiv.). The flask was back-filled three times with argon, degassed CH_2Cl_2 (10 ml) was added and the resulting mixture was stirred for 2 h at room temperature. The solvent was evaporated to give $[Cu(BINap\text{-}SQ\text{-}BQ)]^+$. Then it was washed with cold hexane.

Method B:

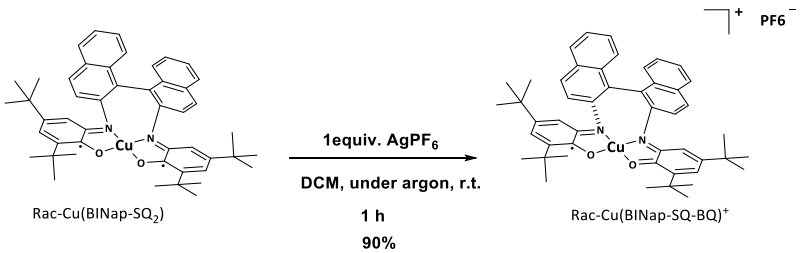

Scheme S5. Other pathway for the synthesis of complex $[Cu(BINap\text{-}SQ\text{-}BQ)]^+$ **1**, related to Figure 2.

To a flame-dried schlenk flask, were introduced [Cu(BINap-SQ_2)]complex (50 mg, 0.066mmol, 1 equiv.) and $AgPF_6$ (16.8 mg, 0.066 mmol, 1 equiv.). The flask was back-filled three times with argon, degassed CH_2Cl_2 (3 ml) was added and the resulting mixture was stirred for 1 h at room temperature. Then the solution was filtered to remove the precipitation. The solvent was evaporated to give $[Cu(BINap\text{-}SQ\text{-}BQ)]^+$. Then it was washed with cold hexane.

HRMS (ESI) calculated for $C_{48}H_{52}CuN_2O_2$ 751.3325, found $[M]^+$ 751.33

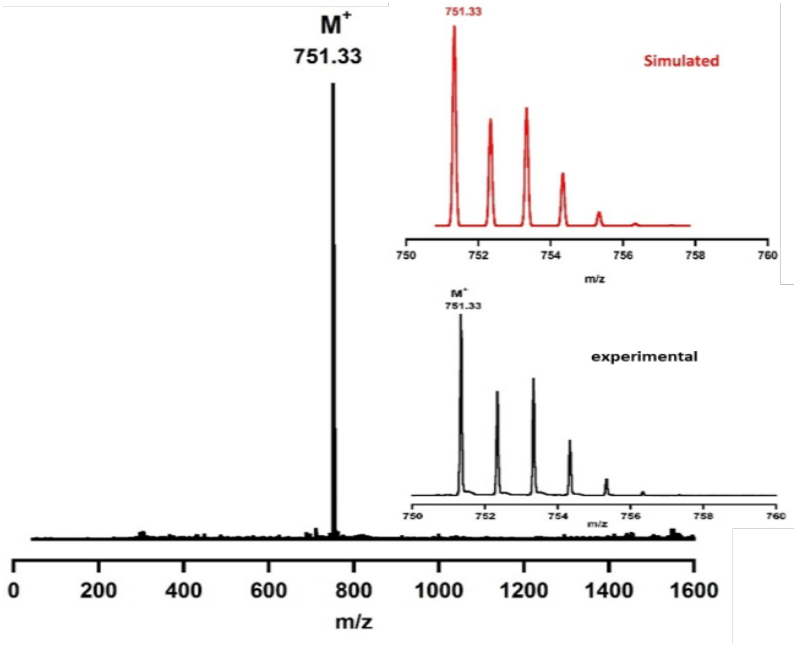

Figure S14. Mass spectrum of $[Cu(BINap\text{-}SQ\text{-}BQ)]^+$, related to Figure 2.

Circular dichroism study of $[Cu(BINap\text{-}SQ\text{-}BQ)]^+$ 1

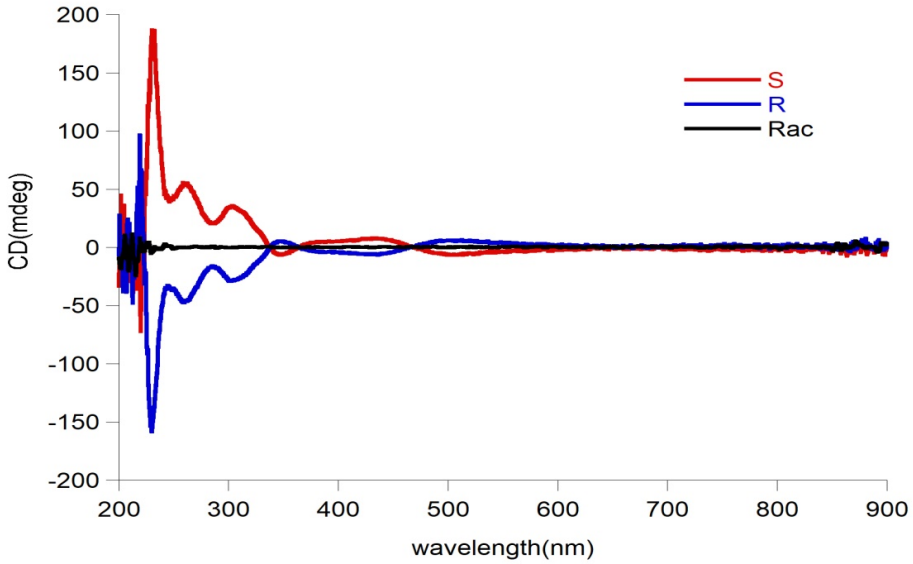

Figure S15. Circular Dichroism spectrum of $[Cu(BINap\text{-}SQ\text{-}BQ)]^+$ (C=0.3 mM) in DCM, related to Figure 2.

CD spectrum of S-$[Cu(BINap\text{-}SQ\text{-}BQ)]^+$ (red line) disclosed a broad positive band with 3 shoulders at (+) 232, 258 and 303 nm. The curve of R-$[Cu(BINap\text{-}SQ\text{-}BQ)]^+$ (blue line) has a negative band with 3 shoulders at (-) 232, 259, and 304 nm . CD spectrum of Racemate-$[Cu(BINap\text{-}SQ\text{-}BQ)]^+$ (black line) is silence.

Cyclic voltammetry and redox potentials of [Cu(BINap-SQ-BQ)]$^+$ 1

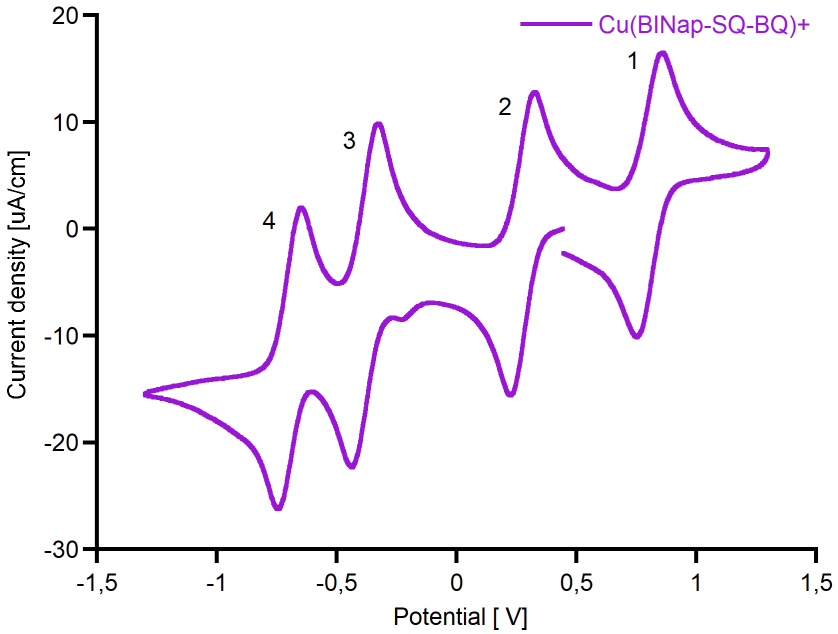

Figure S16. Cyclic voltamogramm of [Cu(BINap-SQ-BQ)]$^+$ (C=1.10^{-3}M) in a 0.1M $TBAPF_6/CH_2Cl_2$ electrolyte, scan rate: 100 mV/s, related to Figure 2.

Table S4. Summary of the redox potentials for the various waves of the CV of [Cu(BINap-SQ-BQ)]$^+$, related to Figure 2.

Wave	Ep(red) V/SCE	Ep(ox) V/SCE	Ep(ox) - Ep(red)	½(Ep(ox)+Ep(red)) V/SCE
1	0.664	0.773	109 mV	0.72
2	0.220	0.312	92 mV	0.27
3	-0.443	-0.342	101 mV	-0.39
4	-0.743	-0.643	100 mV	-0.69

^{1}H-NMR spectrum of [Cu(BINap-SQ-BQ)]$^{+}$ 1

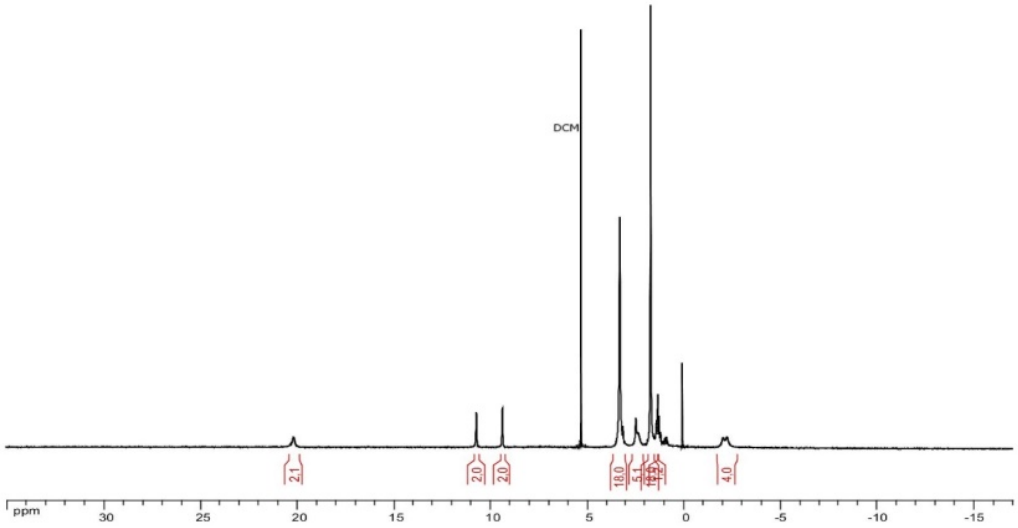

Figure S17. ^{1}H-NMR spectrum of [Cu(BINap-SQ-BQ)] **1**, related to Figure 2.

X-Ray crystal diffraction studies

Single crystals of Ligand **2** were grown by acetonitrile.

Using a mixture of hexane and DCM single crystals of **1** both as a racemate (C2/C space group) and in the pure (S) form (P1 space group) have been obtained.

Attempt to grow crystals of **3** by a mixture of acetonitrile and DCM lead to low quality crystals (vide infra).

For complex **rac -1** and ligand **2**, a single crystal of each compound was selected, mounted onto a cryoloop and transferred into a cold nitrogen gas stream. Intensity data were collected with a Bruker Kappa APEX-II CCD diffractometer using a micro-focused Cu-Kα radiation (λ = 1.54178 Å). Data collections were performed at 200K and 150K respectively, with the Bruker APEXIII suite. Unit-cell parameters determinations, integrations and data reductions were carried out with SAINT program. SADABS was used for scaling and absorption corrections. The structures were solved with SHELXT[1] and refined by full-matrix least-squares methods with SHELXL[2] using Olex2 software package[3] or WinGX suite[4] respectively. All non-hydrogen atoms were refined anisotropically. These structures were deposited at the Cambridge Crystallographic Data Centre with numbers CCDC 1906978 and 1908272 respectively and can be obtained free of charge via www.ccdc.cam.ac.uk.

For complex **S-1**, a single crystal was selected, mounted onto a cryoloop and transferred into a cold nitrogen gas stream. Intensity data were collected with a Bruker Kappa APEX-II CCD diffractometer using a graphite-monochromated Mo-Kα radiation (λ = 0.71073 Å). Data collection was performed at 200K with the Bruker APEXII suite. Unit-cell parameters determination, integration and data reduction were carried out with SAINT program. SADABS was used for scaling and absorption correction. The structure was solved with SHELXT[1] and refined by full-matrix least-squares methods with SHELXL[2] using Olex2 software package[3]. All non-hydrogen atoms were refined anisotropically. This structure was deposited at the Cambridge Crystallographic Data Centre with number CCDC 1906977 and can be obtained free of charge via www.ccdc.cam.ac.uk.

Table S5. Crystallographic data for compounds **1** (racemate and enantiopure form) and **2**, related to Figure 1.

	Complex **1** (racemate)	Complex **1** (pure S-enantiomer)	Ligand **2**
CCDC number	1906978	1906977	1908272
Empirical formula[a]	$C_{52}H_{61}CuF_3N_2O_6S$	$C_{52}H_{61}CuF_3N_2O_6S$	$C_{50}H_{59}N_3O_2$
Moiety Formula	$C_{48}H_{54}CuN_2O_3^+$, $CF_3O_3S^-$, $0.5(C_6H_{14})$	$C_{48}H_{54}CuN_2O_3^+$, $CF_3O_3S^-$, $0.5(C_6H_{14})$	$C_{48}H_{56}N_2O_2$, C_2H_3N
Formula weight (g/mol)	962.62	962.62	734.00
Temperature (K)	200	200	150
Crystal system	Monoclinic	Triclinic	Triclinic
Space group	C2/c	P1	P-1
a (Å)	22.1629(4)	13.5427(4)	9.5701(3)
b (Å)	15.9038(3)	13.6654(5)	14.0551(4)
c (Å)	30.8951(6)	16.2706(6)	17.8824(6)
α (°)	90	66.046(2)	94.091(2)
β (°)	94.4380(10)	73.780(2)	104.344(2)
γ (°)	90	70.417(2)	107.147(2)
Volume (Å^3)	10857.1(4)	2556.49(16)	2199.52(12)
Z	8	2	2
ρ_{calc} (g/cm^3)	1.178	1.251	1.108
Absorption coefficient μ (mm^{-1})	1.387 (CuKα)	0.527 (MoKα)	0.515 (CuKα)
F(000)	4056	1014	792
Crystal size (mm²)	0.24 x 0.10 x 0.03	0.42 x 0.11 x 0.07	0.15 x 0.10 x 0.05
Wavelength λ (Å)	1.54178	0.71073	1.54178
2Θ range (°)	12.528 – 133.274	3.552 – 51.56	6.662 – 133.5
Miller indexes ranges	-26 ≤ h ≤ 26, -17 ≤ k ≤ 18, -36 ≤ l ≤ 36	-16 ≤ h ≤ 16, -16 ≤ k ≤ 16, -19 ≤ l ≤ 19	-11 ≤ h ≤ 11, -16 ≤ k ≤ 16, -21 ≤ l ≤ 17
Measured reflections	42714	57248	17999
Unique reflections	9582	19327	7499
R_{int} / R_{sigma}	0.0848 / 0.0943	0.0629 / 0.0911	0.0406 / 0.0507
Reflections [I ≥ 2σ(I)]	6480	13873	5945
Restraints	34	44	0
Parameters	628	1199	499
Goodness-of-fit F²	1.024	1.011	1.053
Final R indexes[b c] **[all data]**	R1 = 0.0984, wR2 = 0.1942	R1 = 0.0911, wR2 = 0.0965	R1 = 0.0765, wR2 = 0.1588
Final R indexes[b c] **[I ≥ 2σ(I)]**	R1 = 0.0625 wR2 = 0.1675	R1 = 0.0522, wR2 = 0.0861	R1 = 0.0608, wR2 = 0.1498
Largest diff. peak/hole (e/Å^3)	0.84/-0.38	0.42/-049	0.40/-0.34
Flack parameter	-	0.055(5)	-

[a] Including solvent molecules

[b] $R1 = \sum\left||F_o| - |F_c|\right| / \sum |F_o|$ [c] $wR2 = \sqrt{\sum\left(w(F_o^2 - F_c^2)\right) / \sum (w(F_o^2)^2)}$

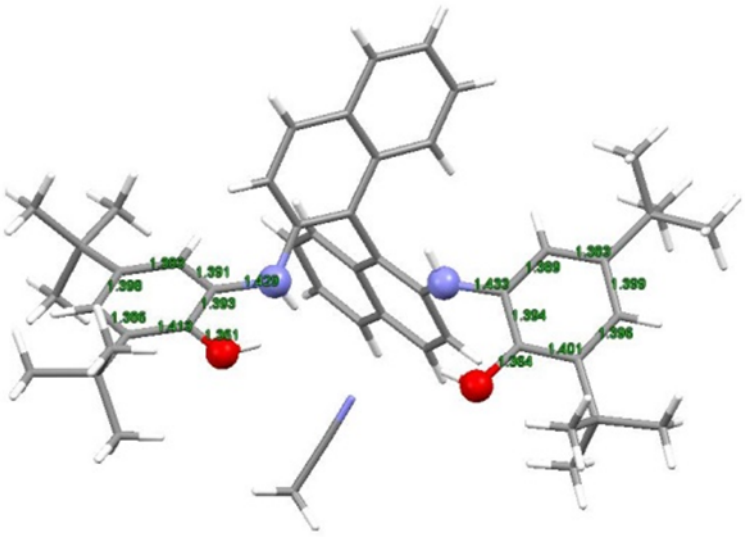

Figure S18. Crystal structure of ligand **2.**CH_3CN, related to Figure 1.

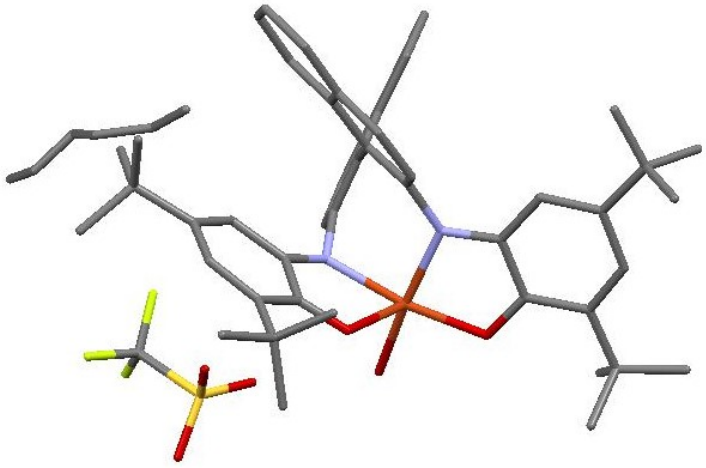

Figure S19. Crystal structure of **1**.(*n*-C_6H_{14}), related to Figure 1.

*N.B. : The geometry (bond distances and angles) of the molecule in the rac-**1** crystals and S-**1** crystals is almost identical*

Representation of [Cu(BINap-SQ_2)] obtained from very poorly diffracting crystals

Despite several recrystallization attempts, diffraction efficiency of the obtained single crystals was very weak. Nevertheless, a single crystal was selected, mounted onto a cryoloop and transferred into a cold nitrogen gas stream. One phi-scan was launched to collect data for unit-cell parameters determination. The measure was performed at 200K with a Bruker Kappa APEXII CCD diffractometer using a graphite-monochromated Mo-Kα radiation (λ = 0.71073 Å) and Bruker APEX2 suite. The 2θmax value did not exceed 32°. Unit cell determination was carried out with SAINT program. A data integration with SAINT and scaling and absorption correction with SADABS were performed with this incomplete dataset.

Table S6. Crystal data for compound [Cu(BINap-SQ_2)] at 200K, related to Figure 1.

Crystal system	Triclinic
Space group	P-1
a (Å)	11.105(18)
b (Å)	19.53(3)
c (Å)	23.28(4)
α (°)	104.23(2)
β (°)	98.09(3)
γ (°)	90.15(3)
Volume ($Å^3$)	4842(14)
Z	2

2θ range for unit cell data collection was 2.152-31.858°.

The structure was solved by SHELXT[1] **but could not be refined** because of the incomplete and poor quality dataset (maximum resolution: 1.29 Angströms).
It gave access to the connectivity between atoms.

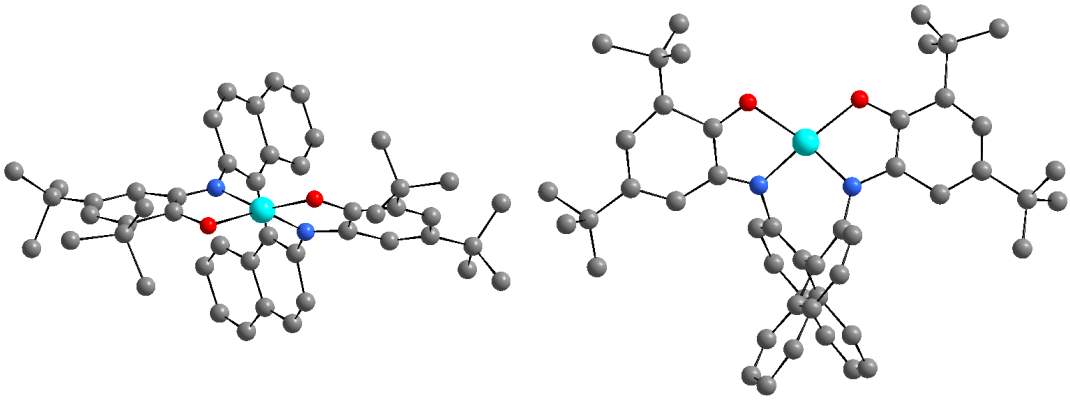

Figure S20. Ball and stick representation of [Cu(BINap-SQ_2)], related to Figure 1.

Optimization condition of aziridination and enantiomeric excess measurement

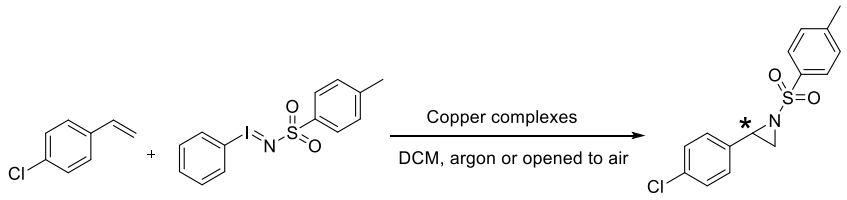

Table S7. Influence of the dilution, related to Scheme 1.

Entry	complex	Temp. (°C)	Time	Solvent	Yield	E.e
1	S-Cu(BINap-SQ-BQ)$^+$(1%)	20	50 min	DCM (0.4 mL)	>99%	4%
2	S-Cu(BINap-SQ-BQ)$^+$(1%)	20	15 min	DCM (10 mL)	>99%	17%
3	S-Cu(BINap-SQ-BQ)$^+$(1%)	20	30 min	DCM (20 mL)	97%	22%
4	S-Cu(BINap-SQ-BQ)$^+$(1%)	20	30 min	DCM (30 mL)	>99%	17%
5	S-Cu(BINap-SQ-BQ)$^+$(1%)	20	30 min	DCM (40 mL)	87%	21%

Table S8. Influence of the temperature and the amount of copper complex, related to Scheme 1.

Entry	complex	Temp. (°C)	Time	Solvent	Yield	E.e
1	S-Cu(BINap-SQ-BQ)$^+$(1%)	20	30 min	DCM(20 mL)	>99%	22%
2	S-Cu(BINap-SQ-BQ)$^+$(1%)	0	20 h	DCM(20 mL)	56%	28%
3	S-Cu(BINap-SQ-BQ)$^+$(3%)	0	1 h	DCM(20 ml)	99%	35%
4	S-Cu(BINap-SQ-BQ)$^+$(3%)	-20	2 h	DCM(20 ml)	70%	34%
4	S-Cu(BINap-SQ-BQ)$^+$(5%)	0	1 h	DCM(20 ml)	99%	33%

HPLC (Chiralcel OJ; 1.0 ml/min; i-PrOH/n-hexane 30:70; λ = 254 nm)[4]

[4] Y. Takeda, Y. Ikeda, A Kuroda, S Tanaka, and S Minakata, *J. Am. Chem. Soc.* **2014**, *136*, 24, 8544-8547.

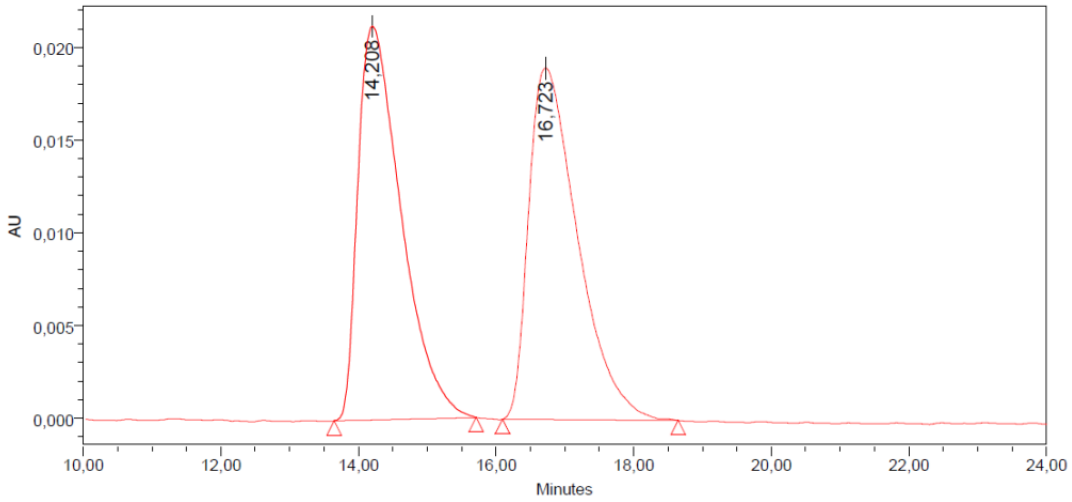

Peak Results

	RT	Area	% Area
1	14,208	928452	49,77
2	16,723	936925	50,23

Figure S21. HPLC analysis profile for S-Cu(BINap-SQ-BQ)$^{+}$, related to Scheme 1 and Table S7.

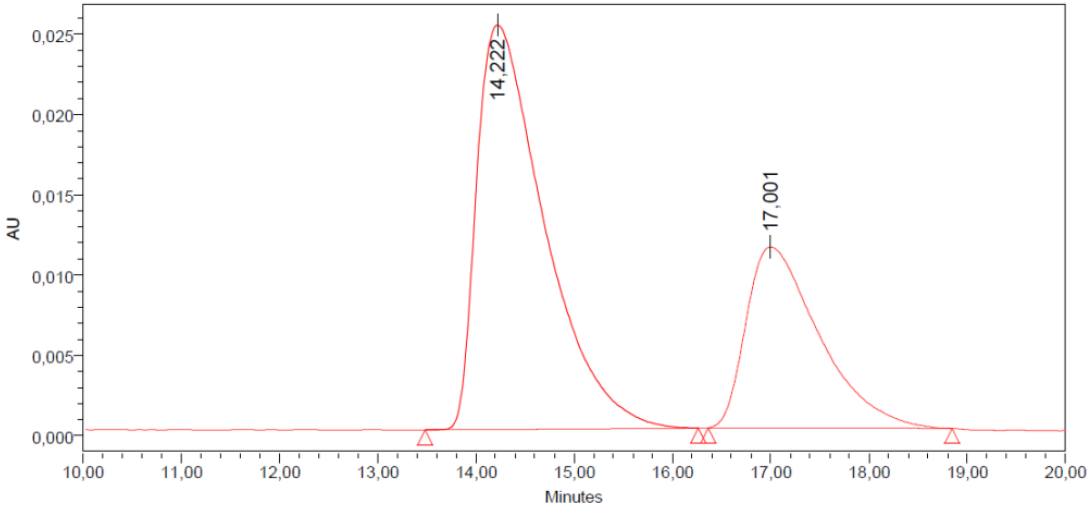

Peak Results

	RT	Area	% Area
1	14,222	1206566	67,43
2	17,001	582837	32,57

Figure S22. HPLC analysis profile for S-Cu(BINap-SQ-BQ)$^{+}$, related to Scheme 1 and Table S8.

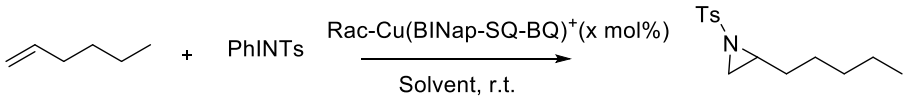

Table S9. Optimization study for the aziridination of 1-hexene, related to Scheme 1.

Entry	[Cu(BINap-SQ-BQ)]+ X mol%	Styrene/PhINTs (equiv./equiv.)	Slovent	T	Yield
1	1 mol%	4/1	DCM(10 ml)	6 h	29%
2	3 mol%	4/1	DCM(10 ml)	6 h	38%
3	3 mol %	4/1	DCM(0.4 ml)	7 h	40%
5	5 mol%	4/1	DCM(10 ml)	35 min	47%
4	1 mol%	4/1	MeCN(0.4 mL)	24 h	71%
6	5 mol%	4/1	MeCN(10 ml)	30 min	62%
7	5mol %	1/2	MeCN(0.4 ml)	2 h	80%

Representative procedure for the aziridination

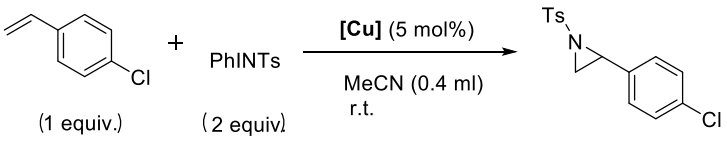

Scheme S6. Aziridination of 4-chlorostyrene, related to Scheme 1.

In a Schlenk flask (under argon or opened to air) were introduced copper complex (0.025 mmol, 5 mol%), 4-chlorostyrene (63 µL, 0.5 mmol, 1 equiv.) and MeCN (400 µL). The nitrene source PhINTs was then added (373 mg, 1 mmol, 2 equiv.) and the reaction mixture was stirred for 2 min at room temperature. The reaction was quenched with a saturated NH_4Cl aqueous solution and the aqueous phase was extracted with CH_2Cl_2. The combined organic layers were washed with brine, dried over Na_2SO_4, filtered and concentrated under vacuum. Purification by silica gel column chromatography (elution: pentane/dichloromethane) afforded the final product as a white powder.

^{1}H NMR yields were determined using trimethoxybenzene as internal standard and calculated considering styrene as limiting reactant.

Benchmarking reactivity for the aziridination

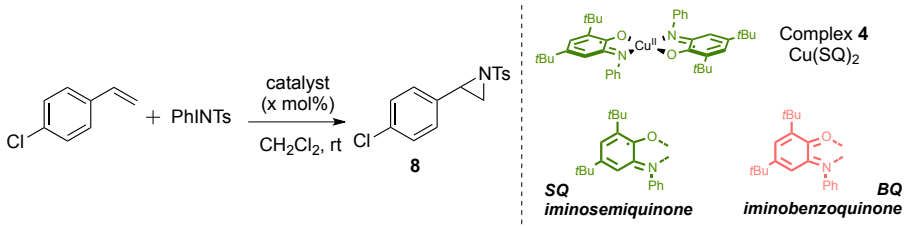

Table S10. Reactivity of strained (**3**, **1** and **5**) and unstrained (**4**, **6** and **7**) complexes in aziridination of 4-chlorostyrene, related to Scheme 1.

entry [a]	1	2	3	4	5	6
Redox state	SQ/SQ		SQ/BQ		BQ/BQ	
Ligand	L_2	BINap	L_2	BINap	L_2	BINap
Complex	**4**	**3**	**6**	**1**	**7**	**5**
Yield (%)	52	11	19	>99	20	74

[a] Reaction conditions: 4-chlorostyrene (4 equiv.), PhINTs (1 equiv.), complex (3 mol%), DCM, 0°C, 1h. Yields were determined by ^{1}H NMR using trimethoxybenzene as internal standard and calculated considering nitrene source as limiting reactant.

N-tosyliminobenzyliodinane synthesis

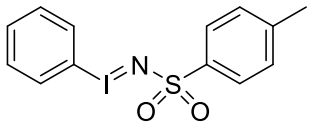

To a stirred solution of tosylamide (1.71 g, 10 mmol, 1 equiv.) in methanol (40 mL) was added portionwise, at 0 °C, KOH (1.40 g, 25 mmol, 2.5 equiv.). After complete dissolution of KOH, iodobenzene diacetate (3.22 g, 10 mmol, 1 equiv.) was added. The reaction mixture was stirred for 3 h at room temperature and then poured into ice water. After 4 h, the suspension was filtered and the resulting solid was washed with cold methanol, to afford PhINTs as a yellow pale solid (1.21 g, 33 %). The characterization data were identical to those previously reported.[5]

^{1}H NMR (d_6-DMSO, 400 MHz) δ 2.27 (s, 3H,), 7.06 (d, *J* = 7.9 Hz, 2H), 7.29 (t, *J* = 7.7 Hz, 2H), 7.40-7.50 (m, 3H), 7.69 (d, *J* = 7.8 Hz, 2H).

^{13}C NMR (d_6-DMSO, 101 MHz) δ 20.9, 117.2, 126.1, 128.6, 130.2, 130.5, 133.2, 140.1, 142.2.

[5] A. Yoshimura, M. W. Luedtke, V. V. Zhdankin, *J. Org. Chem.* **2012**, *77*, 2087–2091.

Mechanistic studies of aziridination by mass spectrometry, UV-vis and ^{1}H NMR spectroscopies

Mass spectrometry

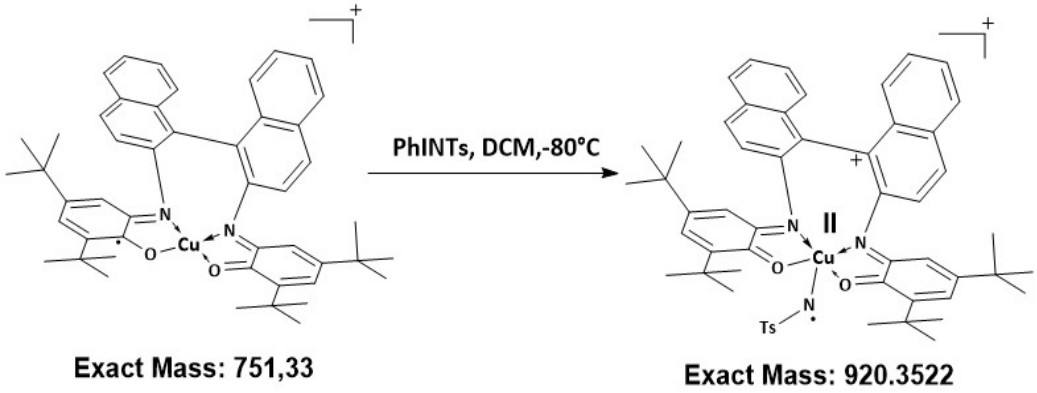

Scheme S8. Proposed structures for reactive intermediate, related to Figure 3.

Protocol: To a solution of [Cu(BINap-SQ-BQ)]$^{+}$ **2** in DCM (0.2 mg/2 ml) kept at -80 °C, PhINTs (10 mg) was added. After 20 min, the solution was filtered quickly and diluted 2 times at -80 °C and quickly injected in the mass spectrometer.

A control experiment was performed at room temperature. The same solution of [Cu(BINap-SQ-BQ)]$^{+}$ **2** was prepared and PhINTs (10 mg) was added at room temperature. The color of the solution changed from green to yellow very quickly. The solution was filtered quickly, diluted 2 times and and quickly injected in the mass spectrometer.

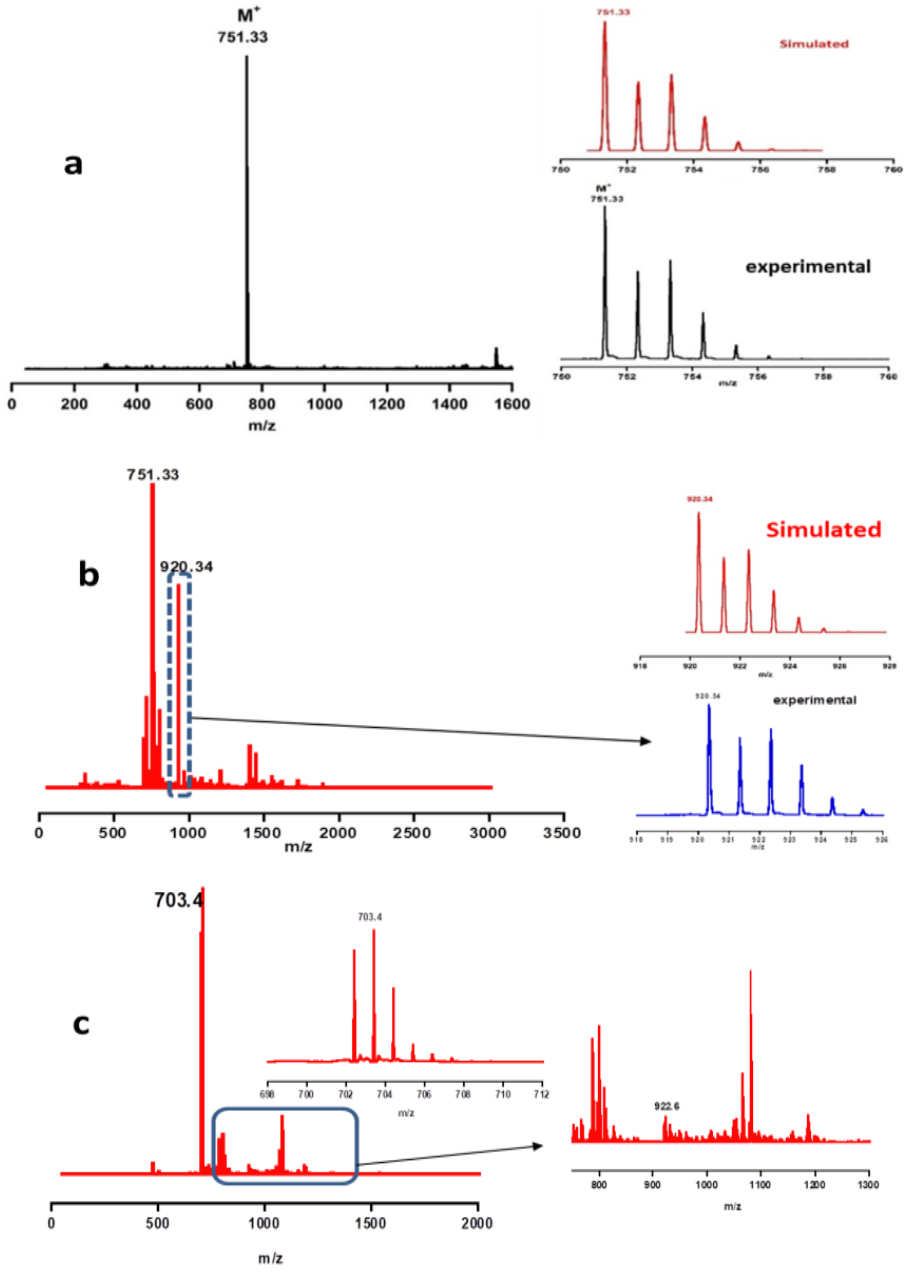

Figure S23. (a) Original mass spectrum of $[Cu(BINap\text{-}SQ\text{-}BQ)]^{+}$ **1** and after addition of PhINTs at (b) -80°C, (c) rt, related to Figure 3.

UV-vis spectroscopy studies

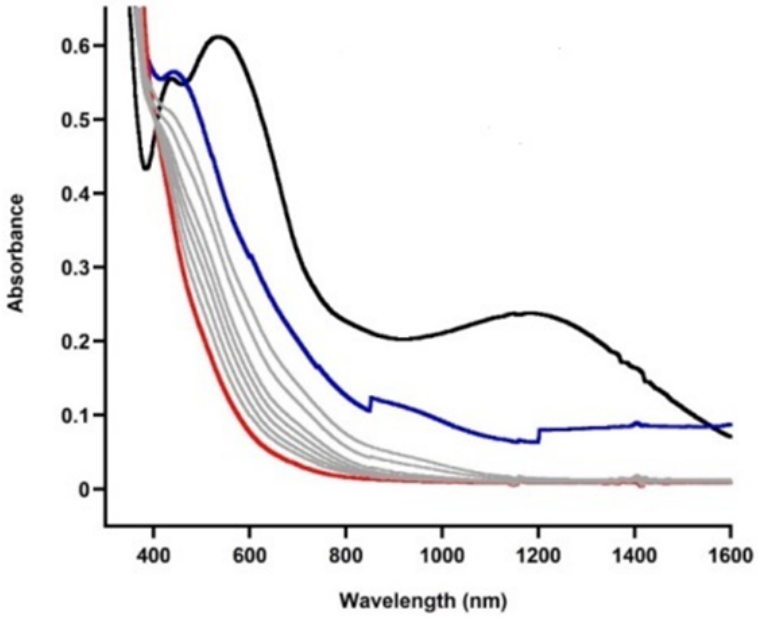

Figure S24. Evolution of the reaction (0.05 mM of $[Cu(BINap\text{-}SQ\text{-}BQ)]^+$ **1** + 1 equiv. of PhINTs) monitored by UV-Vis-NIR spectroscopy in distilled DCM at 0°C under argon atmosphere. Black trace: initial spectrum $Cu(BINap\text{-}SQ\text{-}BQ)^+$. Blue trace: 1.38 min after addition of PhINTs. Red trace: final decay of the intermediate, related to Figure 3.

^{1}H NMR kinetic studies

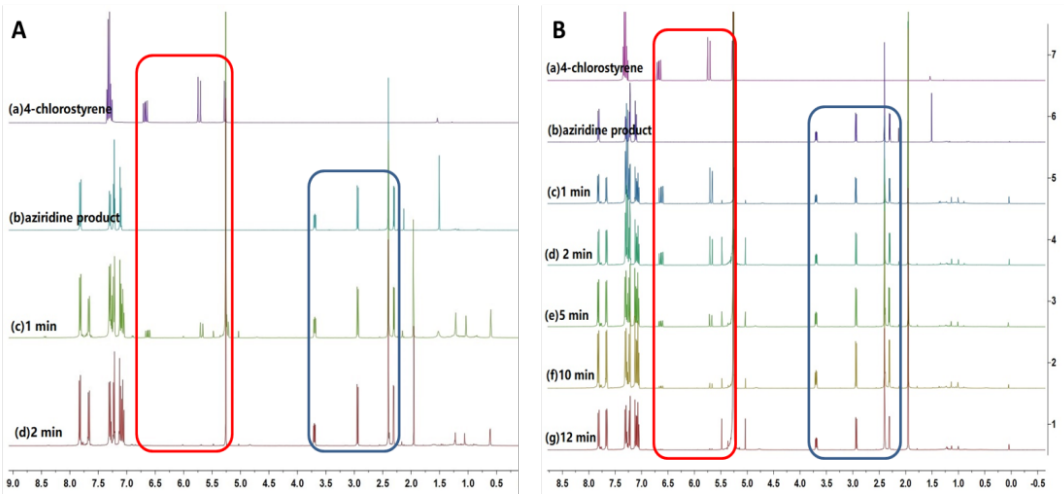

Figure S25. ^{1}H NMR kinetic study of the aziridination reaction catalyzed by: A) complex $Cu(BINap\text{-}SQ\text{-}BQ)^+$ **1** , and B) $Cu(SQ)_2$. Reaction conditions: 4-chlorostyrene (1 equiv.), PhINTs (2 equiv.), copper complex (5 mol%), acetonitrile, rt, related to Figure 3.

Comparative study of the reaction rate of *trans*-chalcone aziridination with complex 1 and complex 4, related to Figure 3.

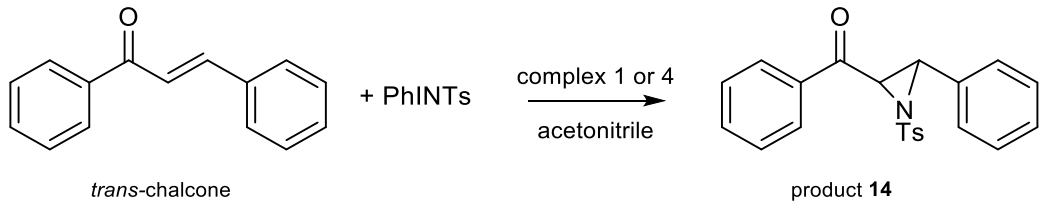

In order to compare the initial rate of the aziridination reaction when catalyzed with **1** or **4**, we choose the *trans*-chalcone as a UV-vis probe as it presents an absorbance around 350 nm where the other species do not abosrb. Note that, to keep the absorbance within the CARY specifications (A<5 in this part of the UV spectrum), the experiment had to be performed at more dilute concentrations than the one performed in the catalytic tests (0.83 mM in chalcone, in a 0.1cm cell) and in acetonitrile, resulting in much slower experiments that did not go to completion during the analysis time.

The diminution at 350 nm (*trans*-chalcone*)*, and also the diminution around 220 nm of a composite peak originating from the consumption of *trans*-chalcone and PhINTS and the formation of **14** is much faster in the case of complex **1** compare to complex **4**, in agreement with **1** being the faster catalyst.

Individual UV-Vis of the different reactants

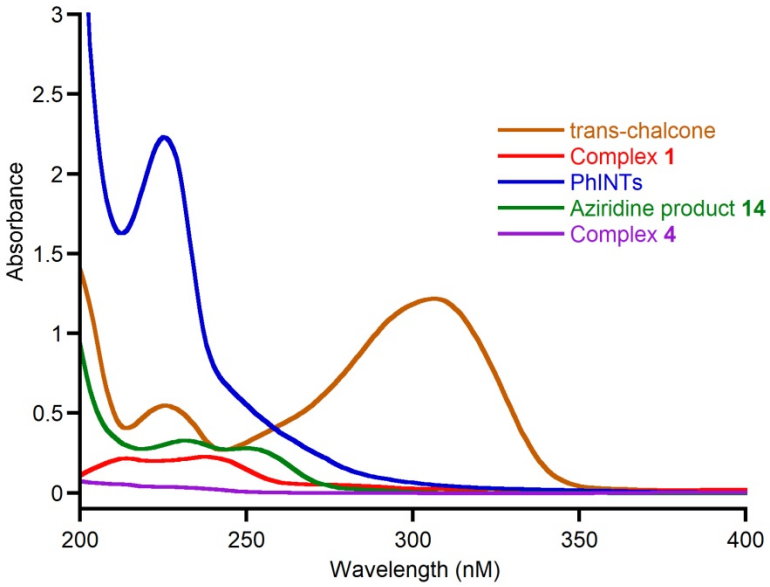

Figure S26. UV-Vis spectra of *trans*-chalcone (0.05mM), PhINTs (0.1mM), complex **1** Cu(BINap-SQ-BQ) (0.0025 mM) and complex **4** $Cu(SQ)_2$ (0.0025 mM) in acetonitrile (1 cm cell), related to Figure 3.

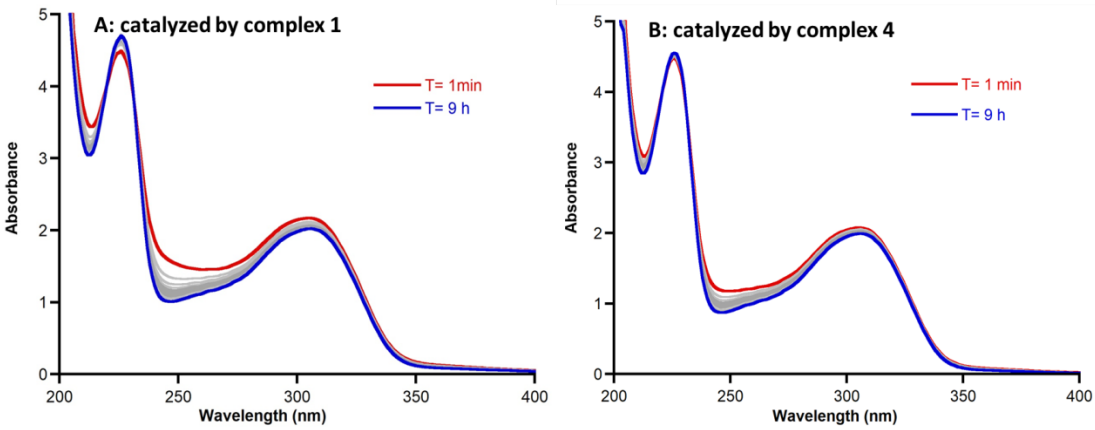

Figure S27. Evolution over 6h of the UV-Vis spectrum in acetonitrile (0.1 cm cell) of the reaction of *trans*-chalcone (0.83mM) with PhINTs (1.67 mM) catalyzed by either **A)** complex **1** Cu(BINap-SQ-BQ) (0.0042 mM) or **B)** complex **4** $Cu(SQ)_2$ (0.0042 mM), related to Figure 3.

Indeed, when plotting the instantaneous rate of reaction at 352nm over time, the initial rate is about twice higher for complex **1**.

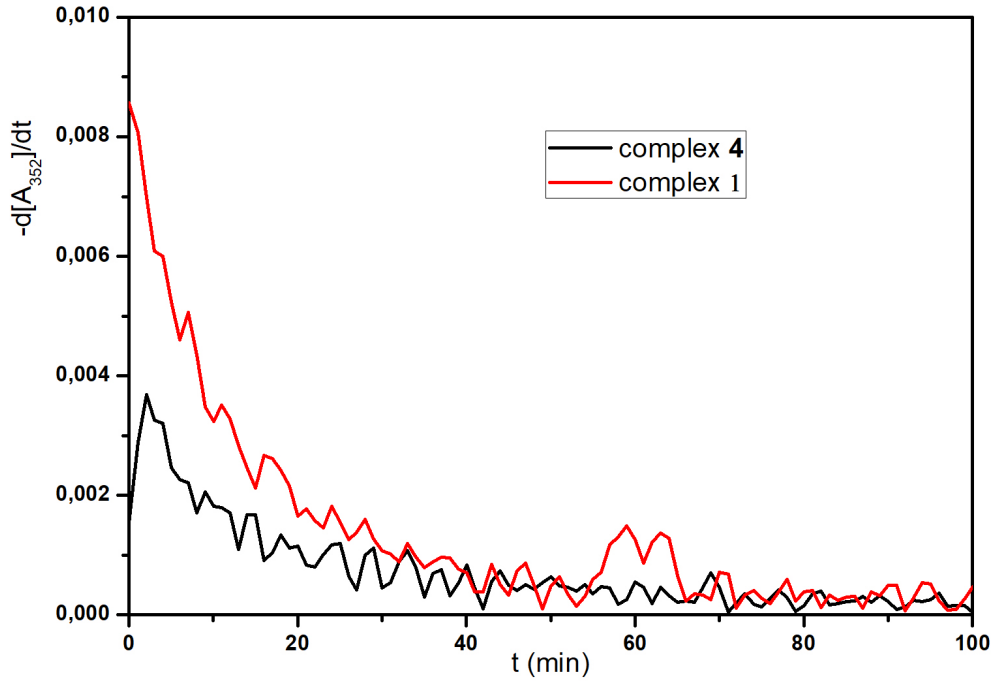

Figure S28. Comparison of the instantaneous rate of disappearance of the *trans*-chalcone band at 352 nm for complex **1** Cu(BINap-SQ-BQ) (red) and complex **4** $Cu(SQ)_2$ (black) over 100 minutes in the aziridination reaction, related to Figure 3.

Optimization condition of cyclopropanation reaction

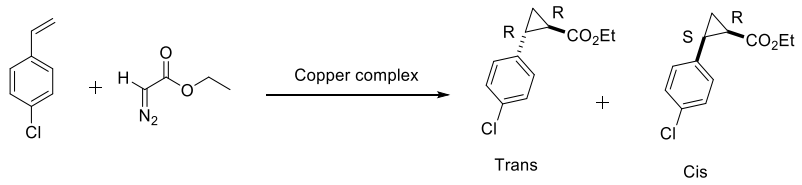

Table S11. The influence of the amount of copper complex, related to Scheme 2.

Entry	complex	Styrene/EDA (equiv./equiv.)	Slovent	Temp.	T	Yield	Trans/Cis
1	S-Cu(BINap-SQ-BQ) (1%)	2/1	DCM	20℃	2 h	86%	1.26:1
2	S-Cu(BINap-SQ-BQ) (0.5%)	2/1	DCM	20℃	2 h	59%	1.27:1
3	S-Cu(BINap-SQ-BQ) (2%)	2/1	DCM	20℃	2 h	83%	1.06:1

Table S12. The influence of the concentration of substrates and reaction time, related to Scheme 2.

Entry	complex	Styrene/EDA (equiv./equiv.)	Slovent	Temp.	T	Yield	Trans/Cis
1	S-Cu(BINap-SQ-BQ) (1%)	2/1	DCM	20℃	2 h	86%	1.26:1
2	S-Cu(BINap-SQ-BQ) (1%)	1/2	DCM	20℃	2 h	99%	1.25:1
3	S-Cu(BINap-SQ-BQ) (1%)	1/2	DCM	20℃	20 min	99%	1.25:1

Table S13. The influence of different of solvent, related to Scheme 2.

Entry	complex	Styrene/EDA (equiv./equiv.)	Slovent	Temp.	T	Yield	Trans/Cis
1	S-Cu(BINap-SQ-BQ) (1%)	1/2	DCM	20℃	2 h	99%	1.25:1
2	S-Cu(BINap-SQ-BQ) (1%)	1/2	Toluene	20℃	2 h	40%	1:1
3	S-Cu(BINap-SQ-BQ) (1%)	1/2	MeCN	20℃	2 h	29%	1:1.12
4	S-Cu(BINap-SQ-BQ) (1%)	1/2	(CH2Cl)2	20℃	2 h	99%	1.44:1
5	S-Cu(BINap-SQ-BQ) (1%)	1/2	CHCl3	20℃	2 h	80%	1.36:1

Table S14. The influence of different complexes, related to Scheme 2.

Entry	Complex	Solvent	Time	Temp.	Yield
1	Cu(BINap-SQ_2)(1%)	DCM(1 ml)	2 h[a]/20min[b]	r.t.	33%/0%
2	Cu(BINap-SQ-BQ)(1%)	DCM(1 ml)	2 h[a]/20min[b]	r.t.	99%/99%
3	Cu(BINap-BQ_2) (1%)	DCM(1ml)	2 h[a]/20min[b]	r.t	76%/67%
4	$Cu(SQ)_2$(1%)	DCM(1ml)	2 h[a]/20min[b]	r.t.	41%/12%
5	Cu(SQ)(BQ)(1%)	DCM(1ml)	2 h[a]/20min[b]	r.t.	93%/75%
6	Cu(BQ)2(1%)	DCM(1ml)	2 h[a]/20min[b]	r.t.	90%/70%

[a]EDA was added in 2 hours, [b]EDA was added in 20 minutes.

Representative procedure for the cyclopropanation, related to Scheme 2.

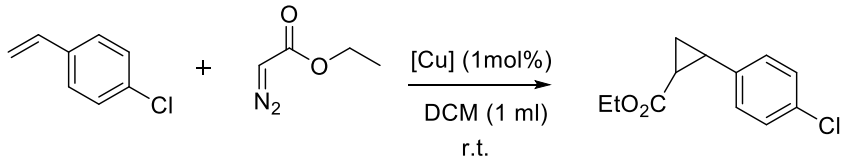

In a Schlenk flask (under argon or opened to air) were introduced copper complex (0.01 mmol, 1 mol%), 4-chlorostyrene (126 µL, 1 mmol, 1 equiv.) and DCM(1 mL). Ethyl diazoacetate(EDA) was then added (210 µL, 2 mmol, 2 equiv.) in 20 minutes. Then the solution was concentrated under vacuum. Purification by silica gel column chromatography (elution: Petroleum ether / Ethyl acetate) afforded the final product as a colorless oil.

^{1}H NMR yields were determined using trimethoxybenzene as internal standard and calculated considering styrene as limiting reactant.

Mechanistic studies of cyclopropanation by mass spectrometry, UV-vis and ^{1}H NMR spectroscopies

Mass spectrometry

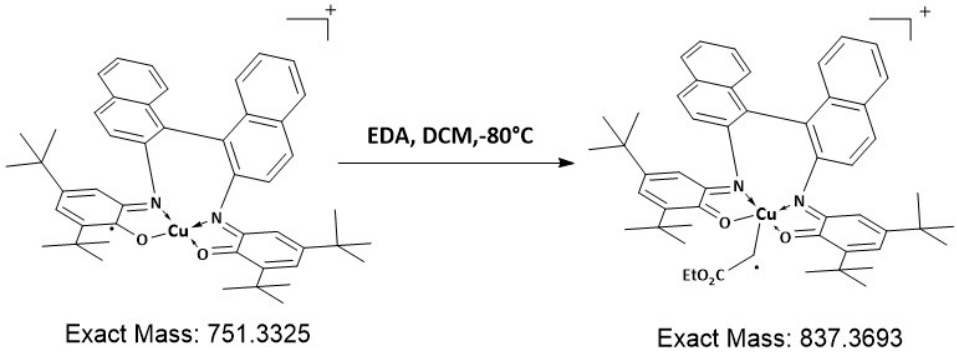

Scheme S9. Proposed structures for reactive intermediate, related to Figure 3.

Protocol: To a solution of $[Cu(BINap\text{-}SQ\text{-}BQ)]^+$ in DCM (0.2 mg/2 ml) kept at -80 °C, EDA (10 mg) was added. After 10 min and 45 min, the solution was filtered quickly and diluted 10 times at -80 °C and quickly injected in the mass spectrometer. The intermediate was formed after 10 min at -80 °C, however the signal was weak. As time going on 45 min, the signal of the intermediate increase and the signal of $[Cu(BINap\text{-}SQ\text{-}BQ)]^+$ decrease.

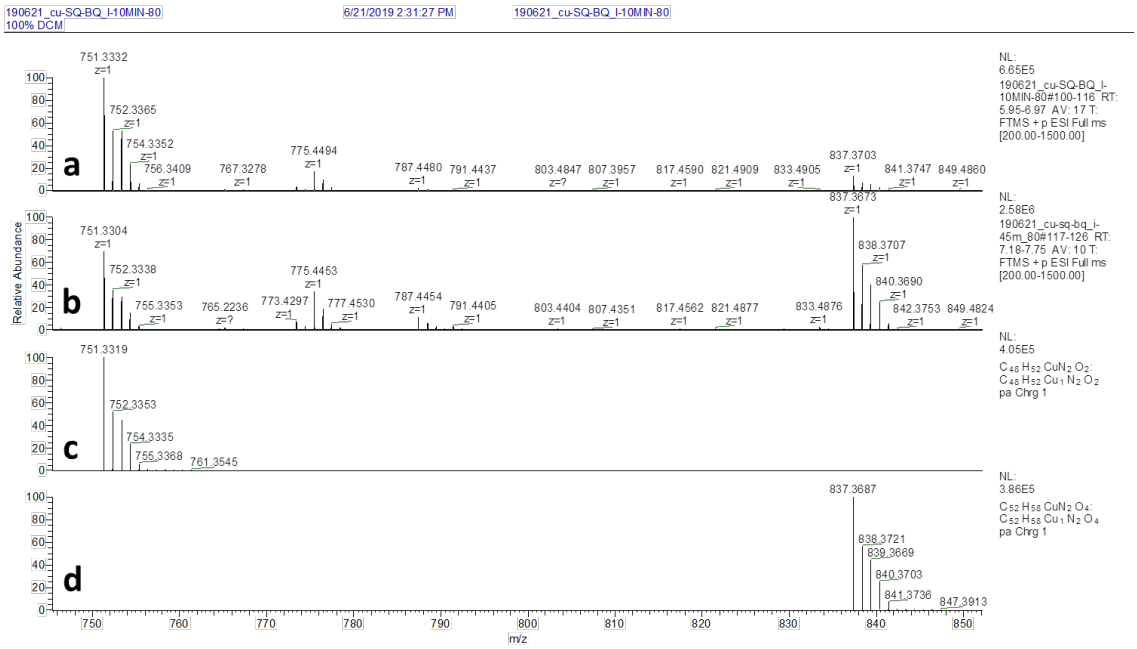

Figure S29. (a) 10 minutes after the EDA is added at -80°C, (b) 45 minutes after the EDA is added at -80°C, (c) simulated data of $[Cu(BINap\text{-}SQ\text{-}BQ)]^+$, (d) simulated data of intermediate.

UV-vis spectroscopy studies

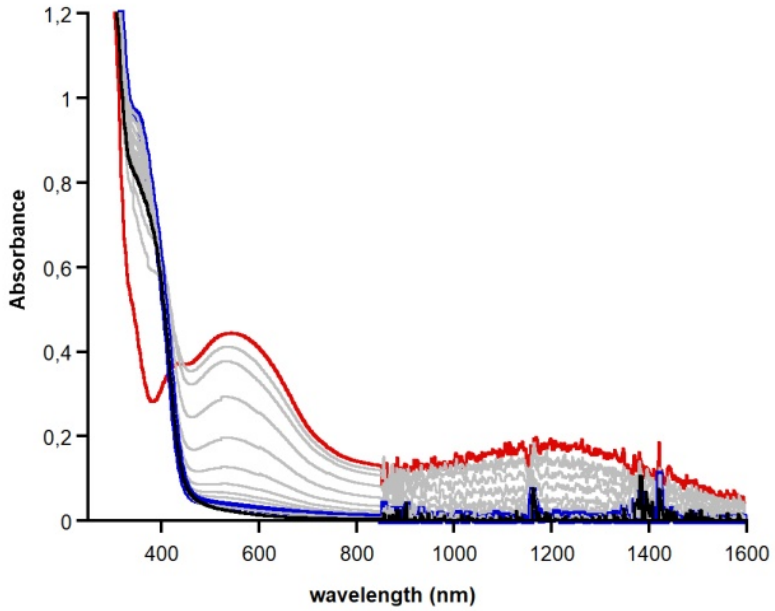

Figure S30. Evolution of the reaction of 0.05 mM $[Cu(BINap\text{-}SQ\text{-}BQ)]^+$ with 10 mg of EDA monitored by UV-Vis-NIR spectroscopy in distilled DCM at 0°C under argon atmosphere. Red trace: initial spectrum $CuL(SQ)(BQ)^+$. Blue trace: 21 min after addition of EDA in a total volume of 2.5 ml at 0 °C. Black trace: the final decay product of the immediate, related to Figure 3.

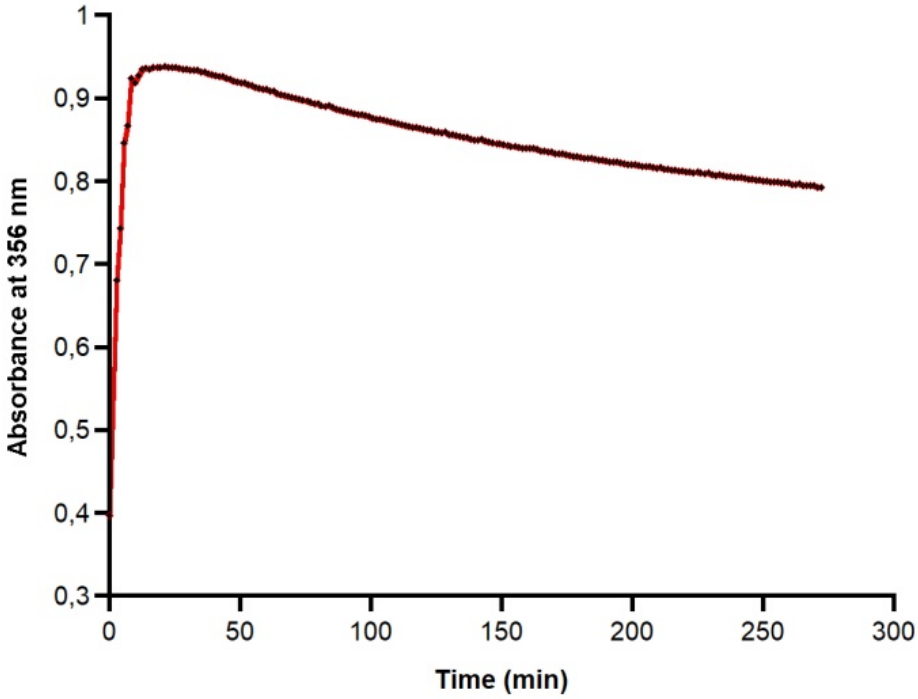

Figure S31. The degradation of the intermediate at 356 nm, related to Figure 3.

^{1}H NMR kinetic studies

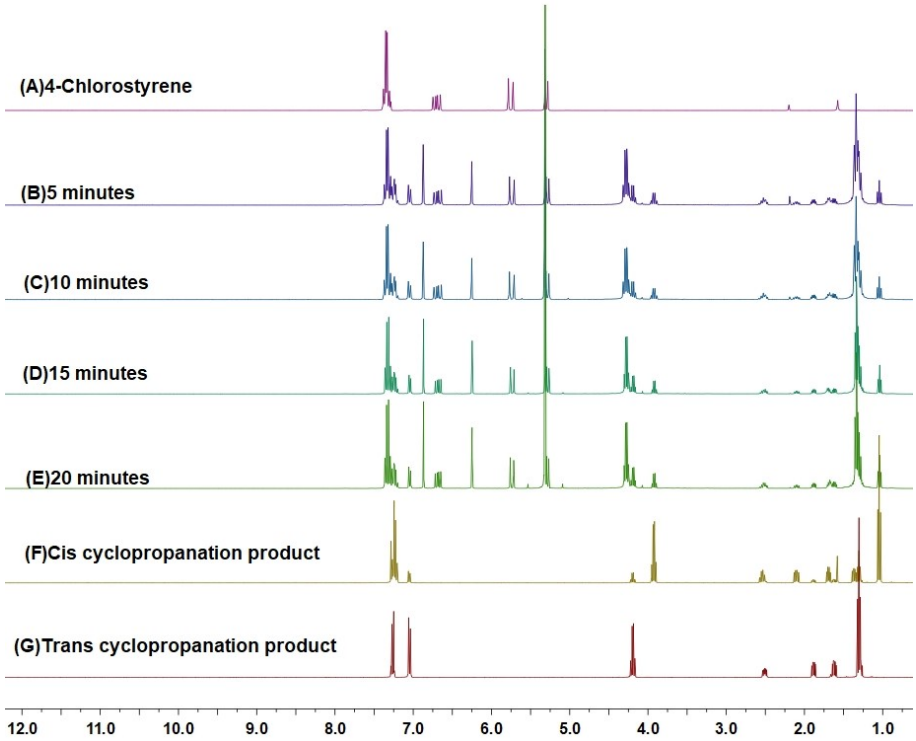

Figure S32. ^{1}H NMR kinetic study of the cyclopropanation reaction catalyzed by [Cu(BINap-SQ-BQ)]$^+$. Reaction conditions: 4-chlorostyrene (1 equiv.), EDA (2 equiv.), copper complex (1 mol%), DCM, rt. EDA was added totally at the beginning, related to Figure 3.

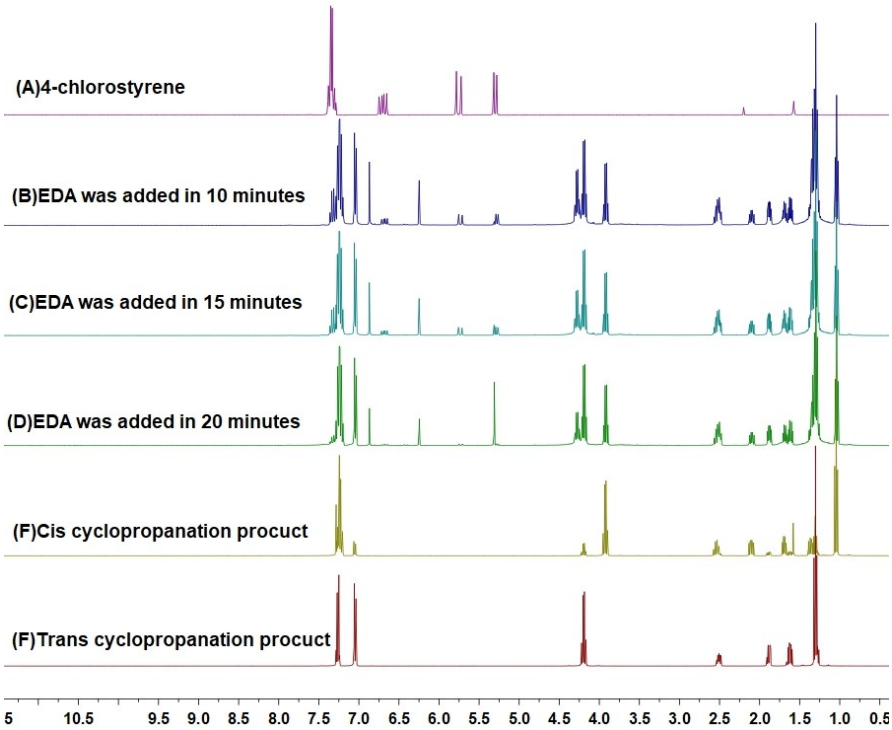

Figure S33. ^{1}H NMR kinetic study of the cyclopropanation reaction catalyzed by [Cu(BINap-SQ-BQ)]$^+$. Reaction conditions: 4-chlorostyrene (1 equiv.),EDA (2 equiv.), copper complex (1 mol%), DCM, rt. EDA was added slowly and finished in different times, related to Figure 3.

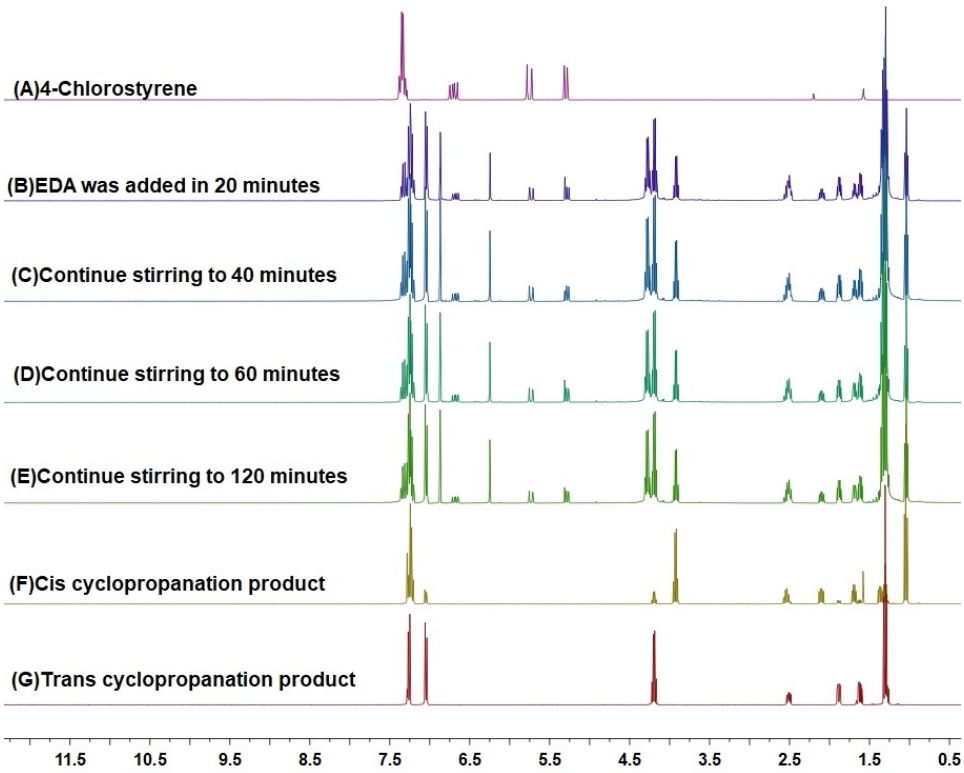

Figure S34. ^{1}H NMR kinetic study of the cyclopropanation reaction catalyzed by [Cu(SQ)(BQ)]$^{+}$. Reaction conditions: 4-chlorostyrene (1 equiv.), EDA (2 equiv.), copper complex (1 mol%), DCM, rt. EDA was added slowly over 20 minutes, related to Figure 3.

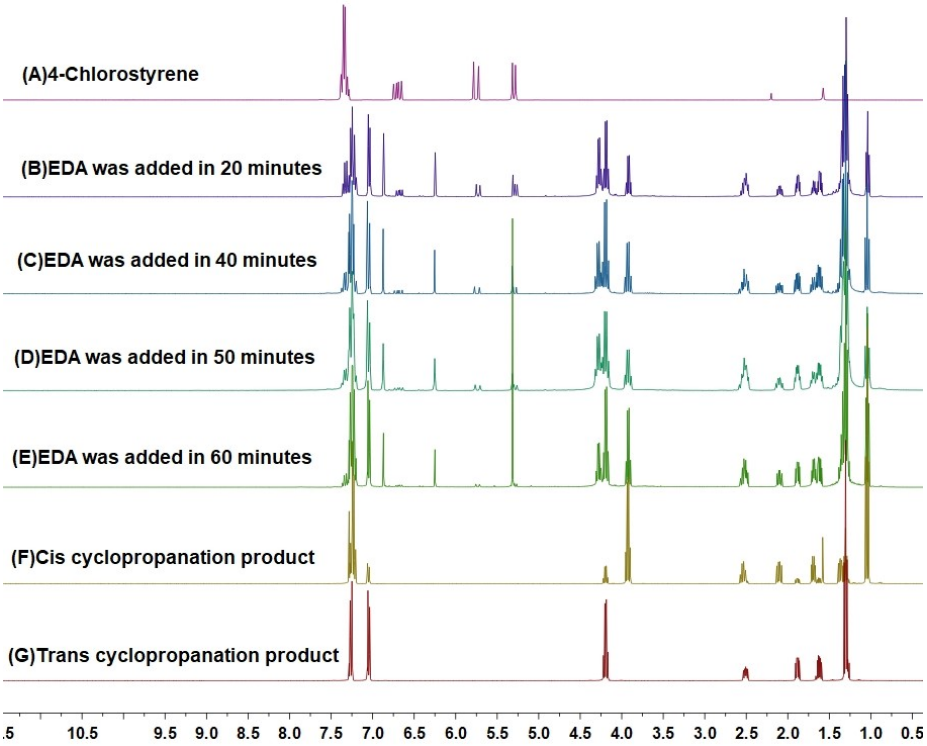

Figure S35. ^{1}H NMR kinetic study of the cyclopropanation reaction catalyzed by [Cu(SQ)(BQ)]$^{+}$. Reaction conditions: 4-chlorostyrene (1 equiv.), EDA (2 equiv.), copper complex (1 mol%), DCM, rt. EDA was added slowly and finished in different times, related to Figure 3.

^{1}H and ^{13}C spectra of aziridination products

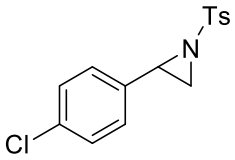

8: **^{1}H NMR** (400 MHz, $CDCl_3$) δ 7.88-7.83 (m, 2H), 7.34 (d, *J* = 8.0 Hz, 2H), 7.29-7.27 (m, 1H), 7.25 (d, *J* = 2.4 Hz, 1H), 7.17-7.13 (m, 2H), 3.73 (dd, *J* = 7.1, 4.4 Hz, 1H), 2.98 (d, *J* = 7.2 Hz, 1H), 2.44 (s, 3H), 2.34 (d, *J* = 4.4 Hz, 1H); **^{13}C NMR** (101 MHz, $CDCl_3$) δ 144.8, 134.88, 134.2, 133.7, 129.8, 128.8, 127.9, 40.2, 36.0, 21.7.

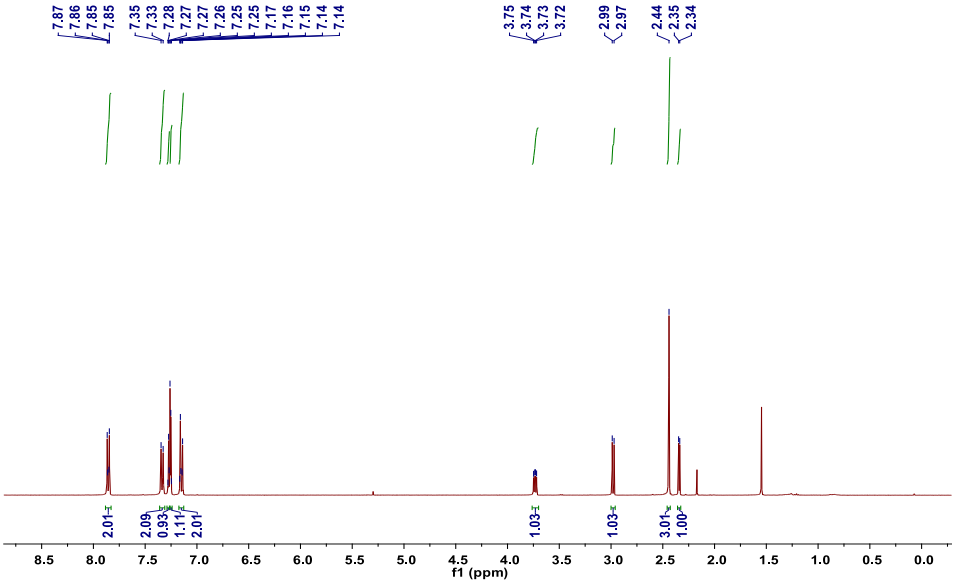

Figure S36. ^{1}H NMR spectrum of **8**, related to Scheme 1.

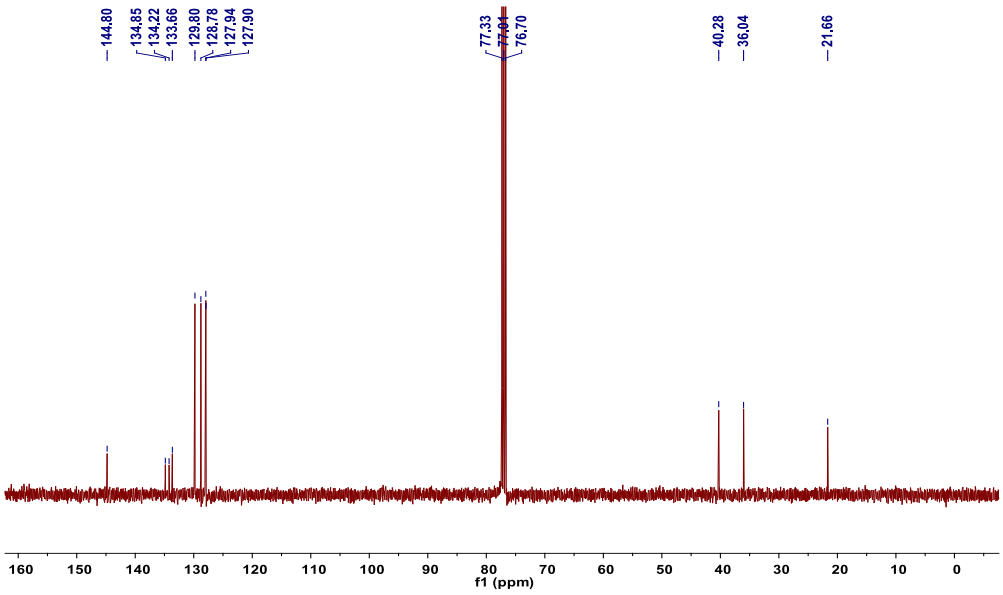

Figure S37. ^{13}C NMR spectrum of **8**, related to Scheme 1.

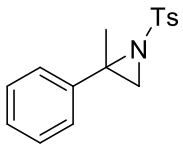

9: ^{1}H NMR (400 MHz, $CDCl_3$) δ 7.90 – 7.85 (m, 2H), 7.38 (dq, *J* = 2.9, 2.0 Hz, 2H), 7.35 – 7.29 (m, 4H), 7.27 (ddd, *J* = 8.6, 3.0, 1.5 Hz, 1H), 2.96 (s, 1H), 2.52 (s, 1H), 2.43 (s, 3H), 2.05 (s, 3H); **^{13}C NMR** (101 MHz, $CDCl_3$) δ 143.9, 141.0, 137.8, 129.5, 128.4, 127.7, 127.5, 126.5, 51.8, 41.8, 21.6, 20.9.

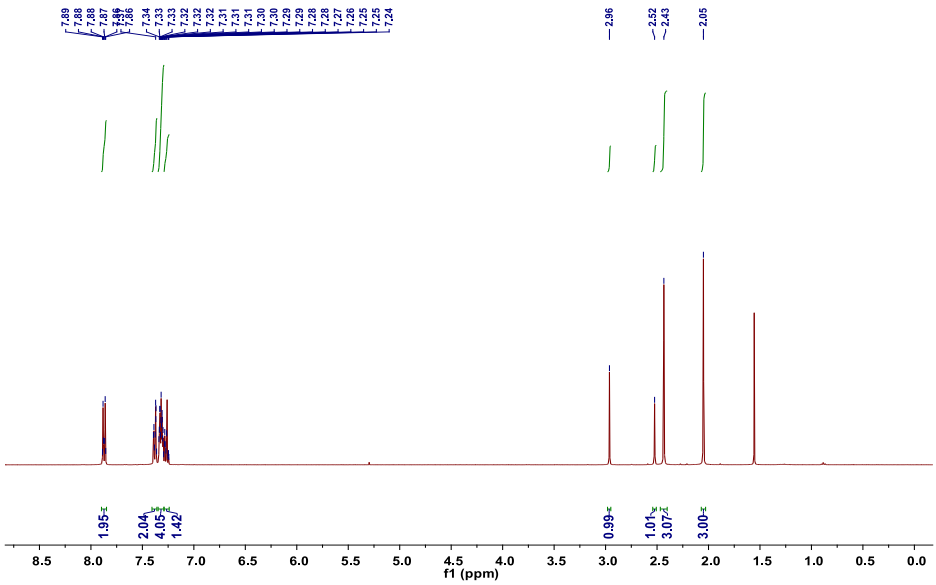

Figure S38. ^{1}H NMR spectrum of **9**, related to Scheme 1.

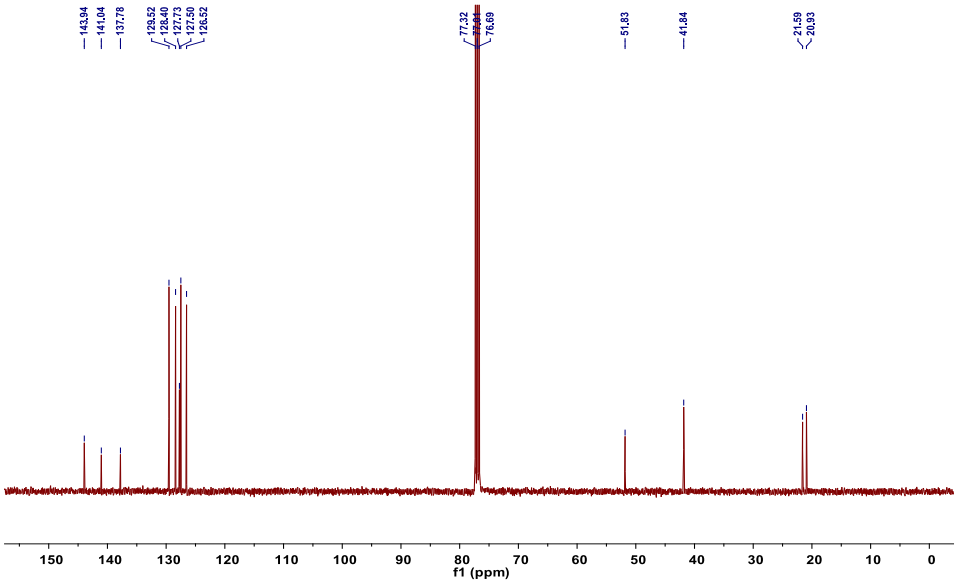

Figure S39. ^{13}C NMR spectrum of **9**, related to Scheme 1.

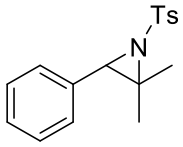

10: ^{1}H NMR (400 MHz, $CDCl_3$) δ 7.89 - 7.84 (m, 2H), 7.30 (dd, J = 8.6, 0.6 Hz, 2H), 7.24 - 7.20 (m, 2H), 7.06 - 7.00 (m, 2H), 4.04 (s, 1H), 2.43 (s, 3H), 1.90 (s, 3H), 1.06 (s, 3H); **^{13}C NMR** (101 MHz, $CDCl_3$) δ 143.8, 138.3, 134.2, 129.5, 128.2, 127.6, 127.3, 127.0, 53.8, 53.6, 21.6, 21.2, 21.1.

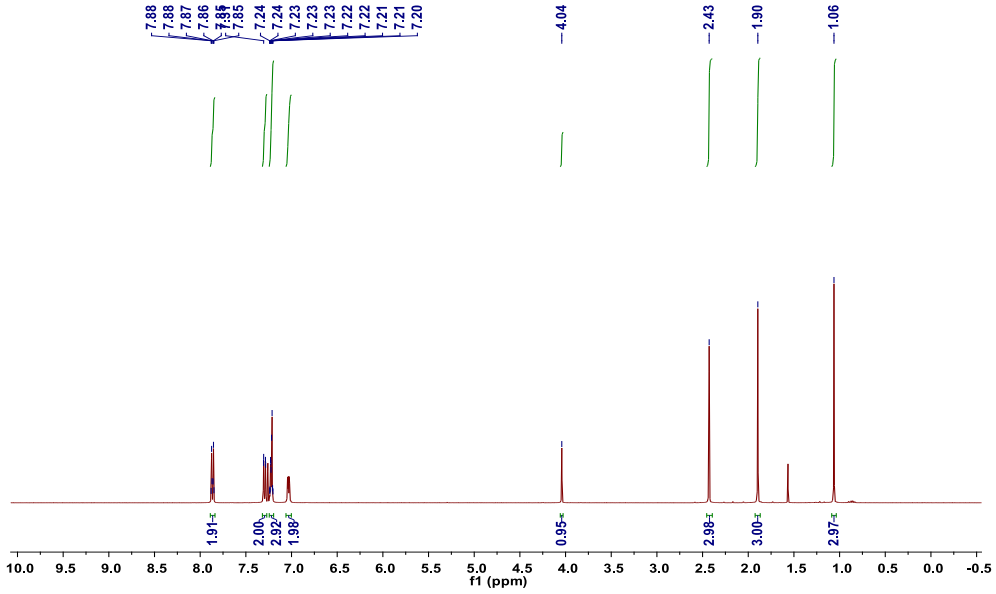

Figure S40. ^{1}H NMR spectrum of **10**, related to Scheme 1.

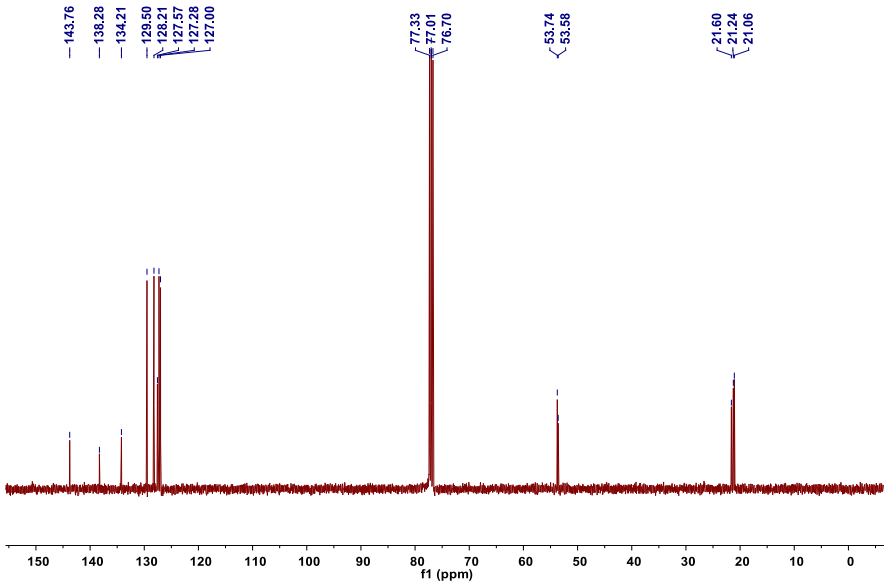

Figure S41. ^{13}C NMR spectrum of **10**, related to Scheme 1.

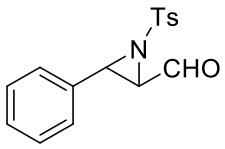

11: ^{1}H NMR (400 MHz, $CDCl_3$) δ 8.78 (d, J = 9.4 Hz, 1H), 7.88 - 7.83 (m, 2H), 7.57 - 7.53 (m, 2H), 7.49 (d, J = 15.8 Hz, 1H), 7.46 - 7.39 (m, 3H), 7.34 (d, J = 8.0 Hz, 2H), 6.99 (dd, J = 15.8, 9.4 Hz, 1H), 2.44 (s, 3H); **^{13}C NMR** (101 MHz, $CDCl_3$) δ 170.8, 153.8, 144.5, 135.4, 134.2, 131.6, 129.8, 129.2, 128.6, 128.0, 124.8, 21.7.

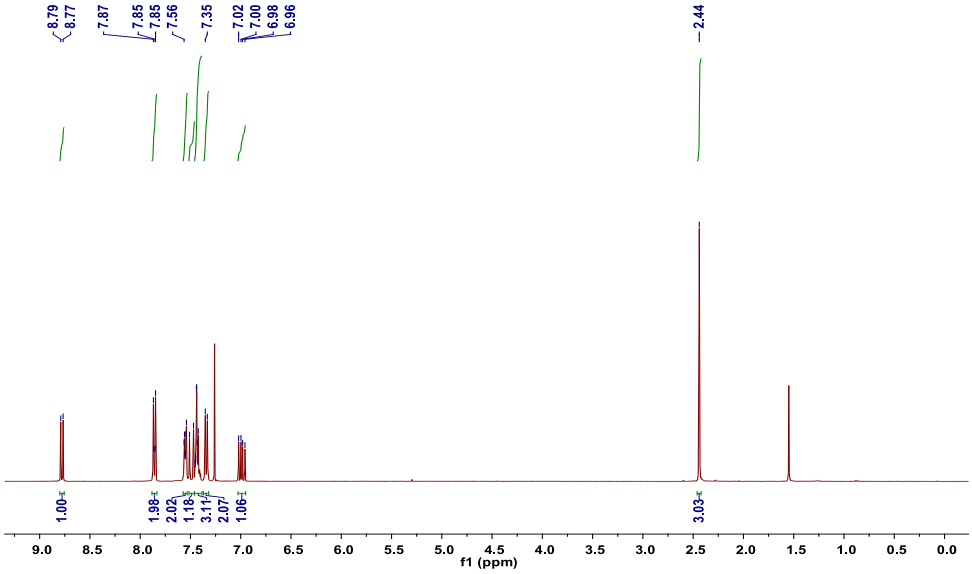

Figure S42. ^{1}H NMR spectrum of **11**, related to Scheme 1.

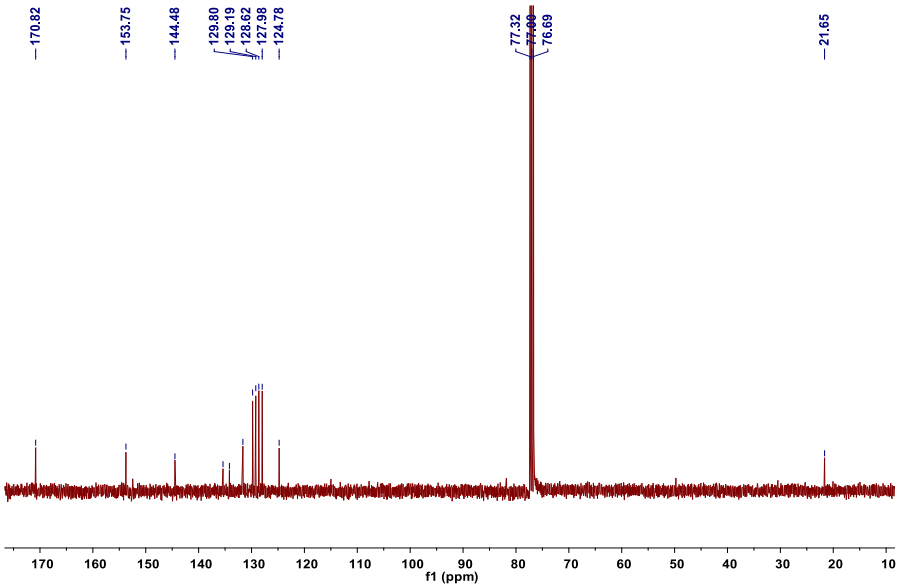

Figure S43. ^{13}C NMR spectrum of **11**, related to Scheme 1.

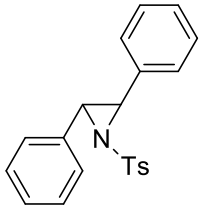

12 : ^{1}H NMR (400 MHz, CDCl3) δ 7.63 (d, J = 8.3 Hz, 2H), 7.42 (dd, J = 6.6, 3.2 Hz, 4H), 7.39 – 7.32 (m, 6H), 7.20 (d, J = 8.1 Hz, 2H), 4.27 (s, 2H), 2.39 (s, 3H); **^{13}C NMR** (101 MHz, $CDCl_3$) δ 143.9, 137.1, 133.1, 129.4, 128.7, 128.4, 127.5, 77.3, 50.4, 21.6.

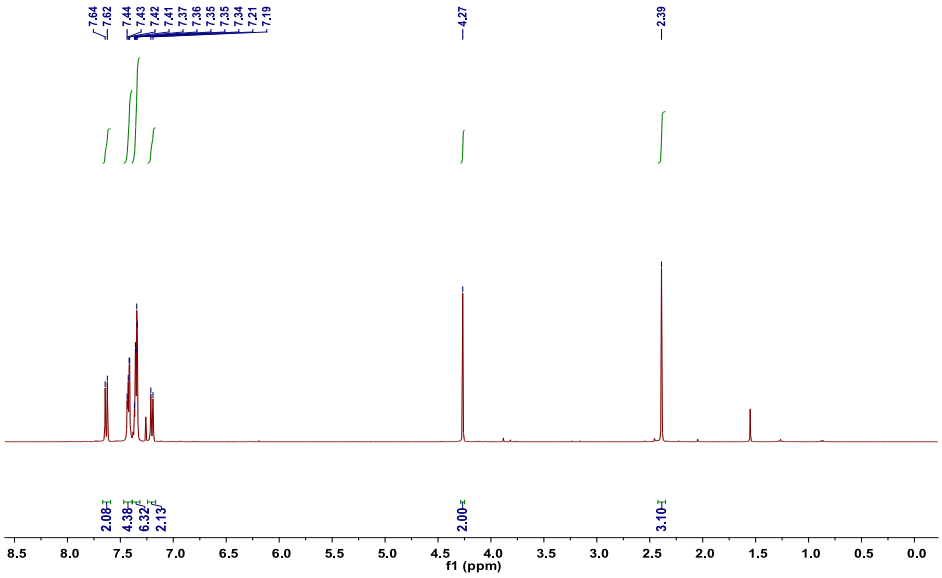

Figure S44. ^{1}H NMR spectrum of **12**, related to Scheme 1.

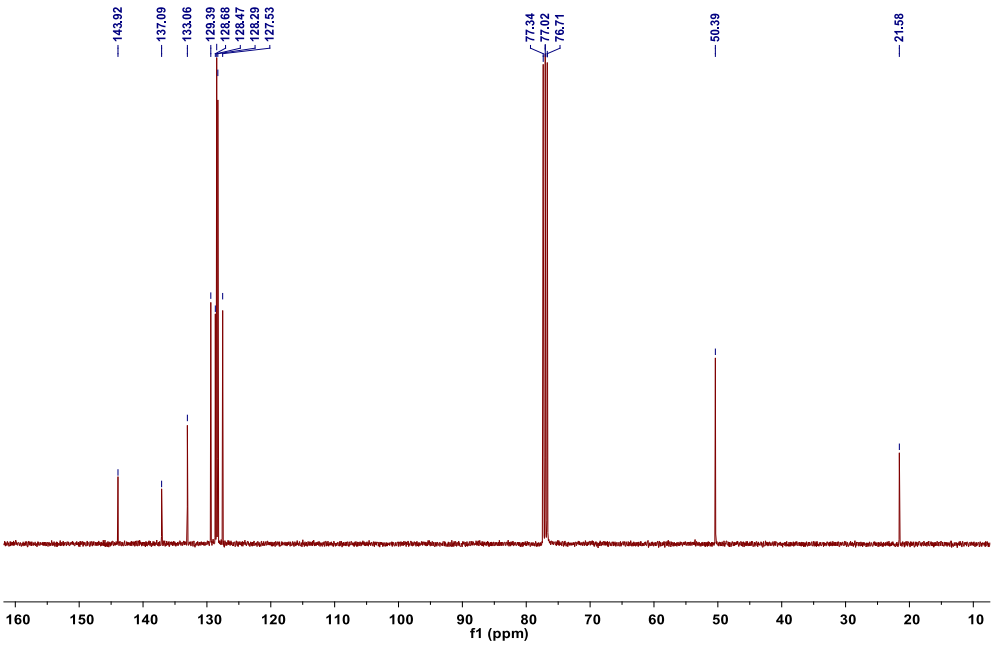

Figure S45. ^{13}C NMR spectrum of **12**, related to Scheme 1.

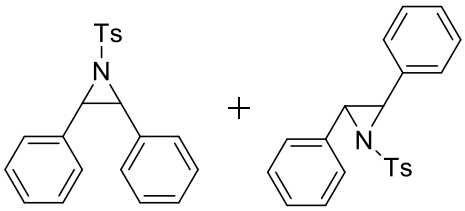

12 and 13: ^{1}H NMR (400 MHz, $CDCl_3$) δ 7.96 (d, J = 8.3 Hz, 2H-cis), 7.63 (d, J = 8.3 Hz, 2H-trans), 7.46 – 7.39 (m, 4H-trans), 7.39 – 7.31 (m, 6H-trans+2H-cis), 7.20 (d, J = 8.2 Hz, 2H-trans), 7.15 – 7.08 (m, 6H-cis), 7.07 – 7.00 (m, 4H-cis), 4.26 (s, 2H-trans), 4.22 (s, 2H-cis), 2.45 (s, 3H-cis), 2.39 (s, 3H-trans).

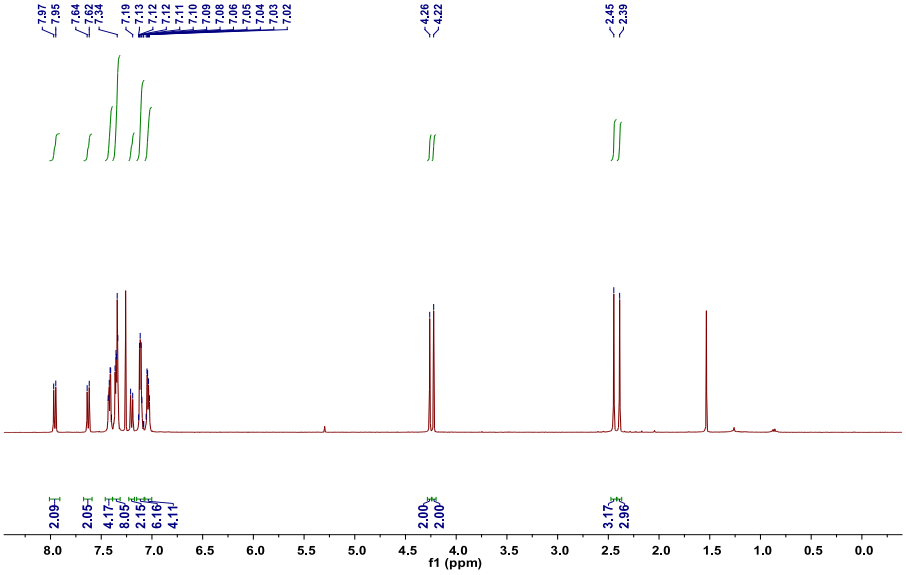

Figure S46. ^{1}H NMR spectrum of a mixture of **12** and **13**, related to Scheme 1.

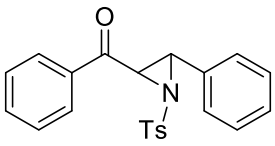

14: ^{1}H NMR (400 MHz, $CDCl_3$) δ 8.10 – 8.00 (m, 2H), 7.76 – 7.69 (m, 2H), 7.66 – 7.59 (m, 1H), 7.49 (dd, *J* = 10.9, 4.5 Hz, 2H), 7.40 – 7.30 (m, 5H), 7.23 (d, *J* = 8.0 Hz, 2H), 4.52 (d, *J* = 4.2 Hz, 1H), 4.29 (d, *J* = 4.2 Hz, 1H), 2.40 (s, 3H); **^{13}C NMR** (101 MHz, $CDCl_3$) δ 190.3, 144.4, 136.7, 136.0, 134.1, 132.9, 129.5, 128.9, 128.9, 128.8, 128.6, 127.7, 127.5, 50.2, 47.5, 21.6.

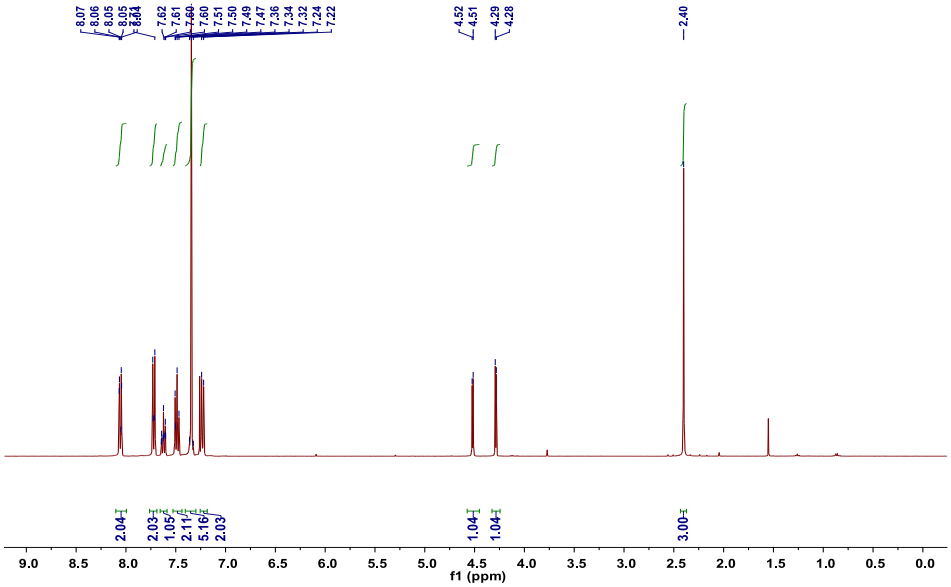

Figure S47. ^{1}H NMR spectrum of **14**, related to Scheme 1.

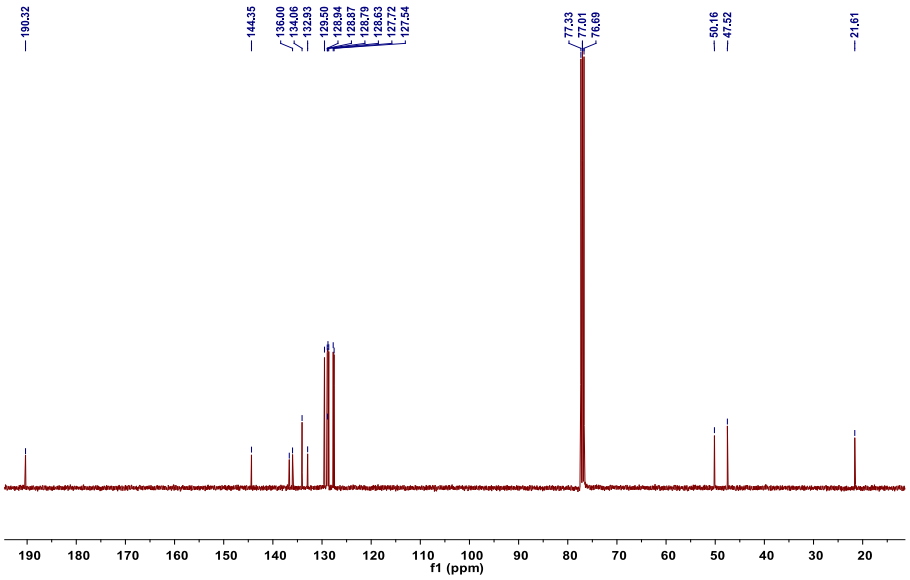

Figure S48. ^{13}C NMR spectrum of **14**, related to Scheme 1.

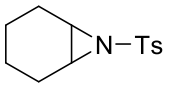

15: **^{1}H NMR** (300 MHz, $CDCl_3$) δ 7.82 (d, J = 8.3 Hz, 2H), 7.32 (d, J = 8.0 Hz, 2H), 3.01 – 2.93 (m, 2H), 2.44 (s, 3H), 1.78 (dd, J = 8.4, 3.3 Hz, 4H), 1.39 (ddd, J = 10.2, 6.8, 2.6 Hz, 2H), 1.19 (ddd, J = 8.8, 6.7, 3.0 Hz, 2H); **^{13}C NMR** (101 MHz, $CDCl_3$) δ 143.9, 135.9, 129.6, 127.6, 39.8, 22.8, 21.6, 19.4.

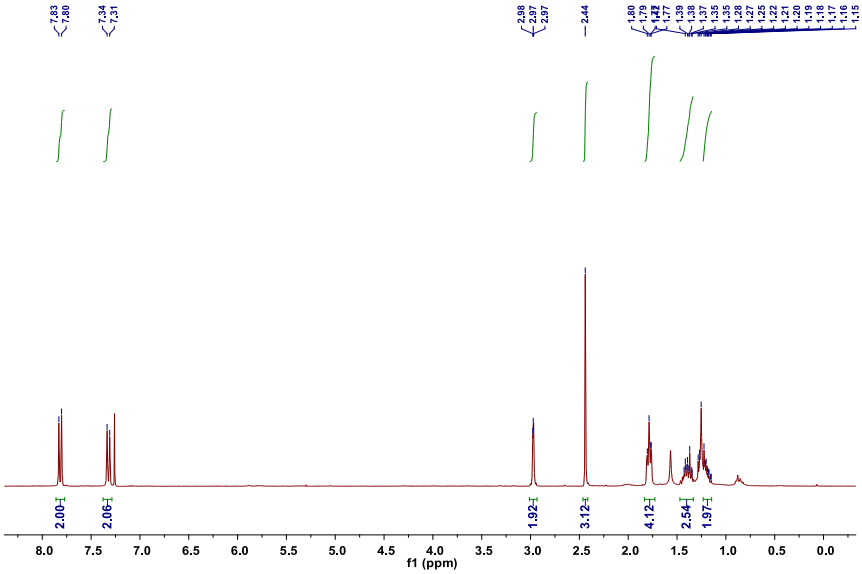

Figure S49. ^{1}H NMR spectrum of **15**, related to Scheme 1.

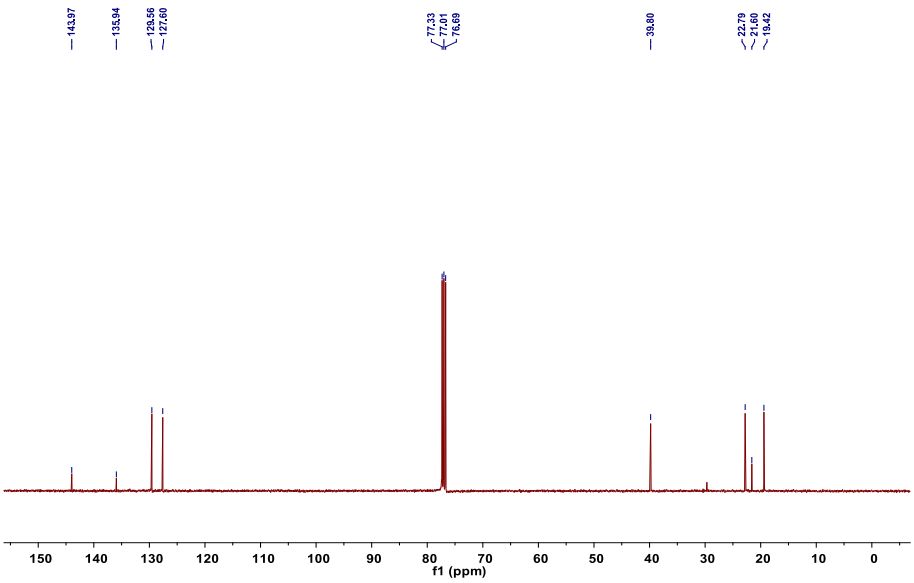

Figure S50. ^{13}C NMR spectrum of **15**, related to Scheme 1.

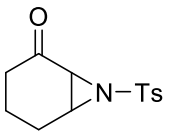

16: ^{1}H NMR (400 MHz, $CDCl_3$) δ 7.83 - 7.79 (m, 2H), 7.35 (dd, J = 8.5, 0.6 Hz, 2H), 3.48 - 3.43 (m, 1H), 3.15 (d, J = 6.6 Hz, 1H), 2.45 (s, 3H), 2.44 - 2.37 (m, 1H), 2.23 - 2.14 (m, 1H), 2.03 (ddd, J = 17.4, 8.7, 3.6 Hz, 1H), 1.96 - 1.80 (m, 2H), 1.67 (ddd, J = 14.5, 7.4, 3.7 Hz, 1H); **^{13}C NMR** (101 MHz, $CDCl_3$) δ 201.3, 145.1, 134.4, 129.9, 127.9, 43.9, 40.9, 37.1, 21.8, 21.7, 17.1.

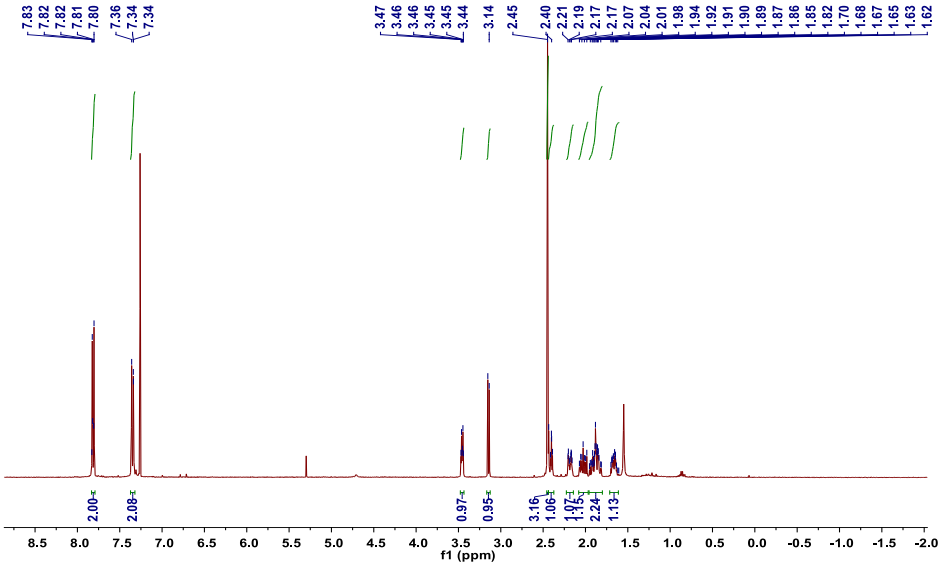

Figure S51. ^{1}H NMR spectrum of **16**, related to Scheme 1.

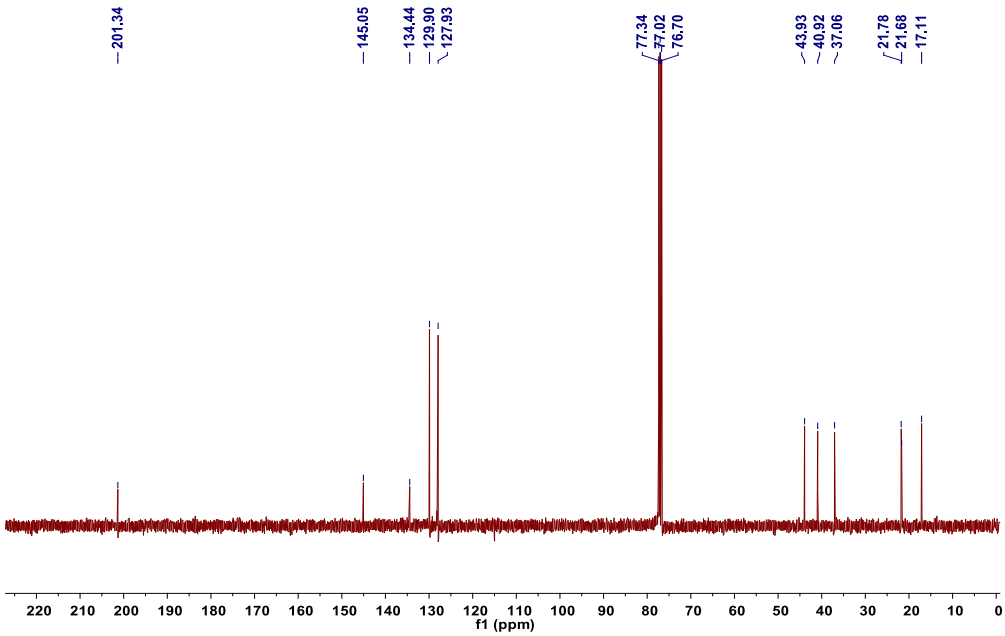

Figure S52. ^{13}C NMR spectrum of **16**, related to Scheme 1.

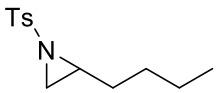

17: ^{1}H NMR (400 MHz, $CDCl_3$) δ 7.86 - 7.78 (m, 2H), 7.32 (d, J = 0.6 Hz, 2H), 2.72 (tt, J = 7.3, 4.8 Hz, 1H), 2.62 (d, J = 7.0 Hz, 1H), 2.44 (s, 3H), 2.05 (d, J = 4.6 Hz, 1H), 1.59 - 1.47 (m, 1H), 1.34 (td, J = 14.1, 7.3 Hz, 1H), 1.28 - 1.15 (m, 4H), 0.81 (dd, J = 8.4, 5.7 Hz, 3H); **^{13}C NMR** (101 MHz, $CDCl_3$) δ 144.4, 135.2, 129.6, 127.9, 40.4, 33.8, 31.0, 28.9, 22.1, 21.6, 13.8.

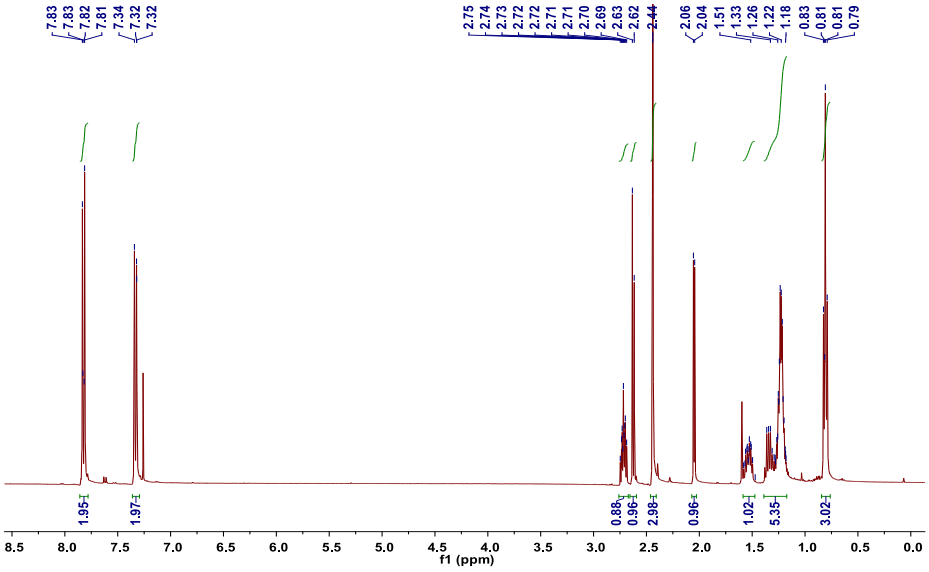

Figure S53. ^{1}H NMR spectrum of **17**, related to Scheme 1.

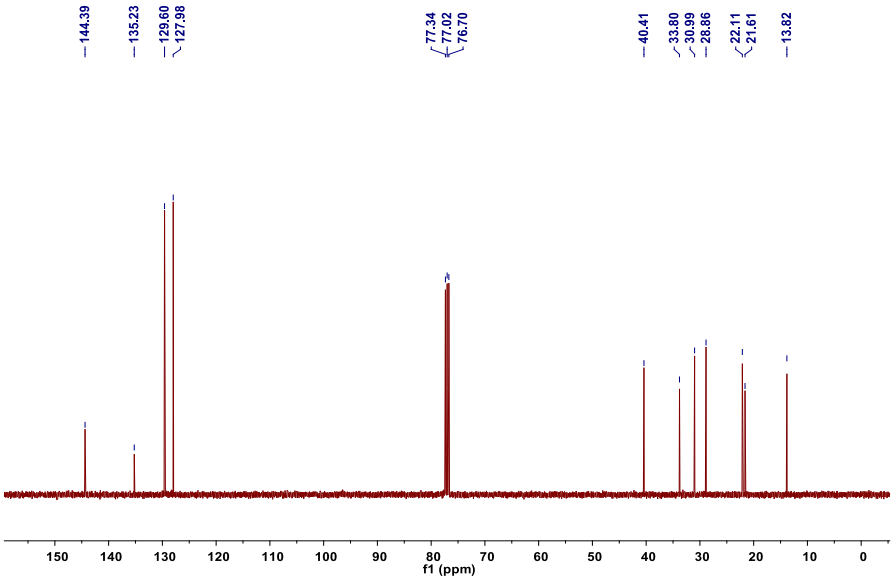

Figure S54. ^{13}C NMR spectrum of **17**, related to Scheme 1.

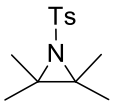

18: **^{1}H NMR** (400 MHz, $CDCl_3$) δ 7.79 (d, J = 8.2 Hz, 2H), 7.28 (d, J = 8.0 Hz, 2H), 2.42 (s, 3H), 1.47 (s, 12H); **^{13}C NMR** (101 MHz, $CDCl_3$) δ 143.1, 139.9, 129.3, 126.8, 53.0, 21.5, 20.2.

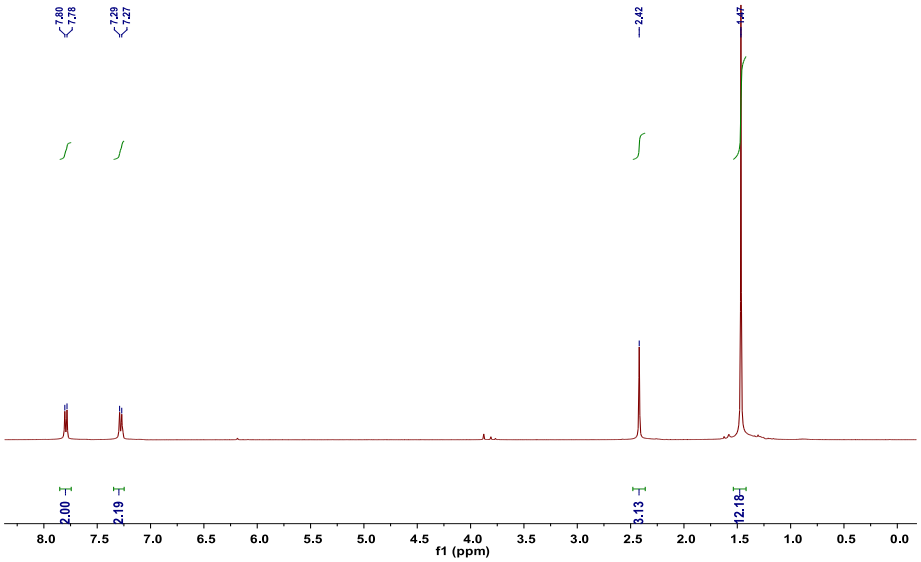

Figure S55. ^{1}H NMR spectrum of **18**, related to Scheme 1.

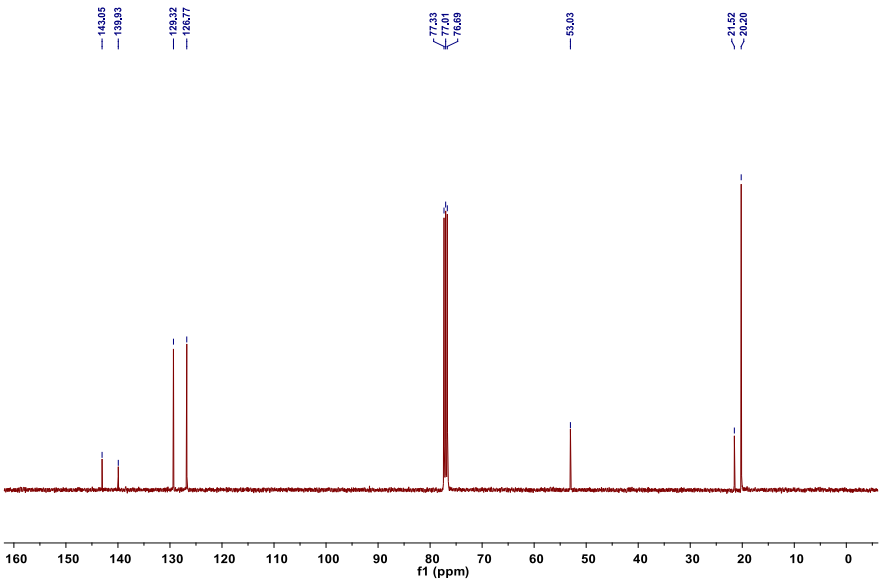

Figure S56. ^{13}C NMR spectrum of **18**, related to Scheme 1.

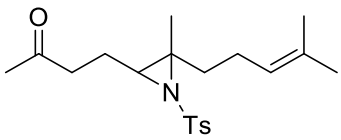

19: ^{1}H NMR (400 MHz, $CDCl_3$) δ 7.84 - 7.79 (m, 2H), 7.30 (dd, *J* = 8.5, 0.6 Hz, 2H), 5.17 - 5.09 (m, 1H), 4.07 (dd, *J* = 11.9, 5.2 Hz, 1H), 3.88 (dd, *J* = 11.9, 7.6 Hz, 1H), 3.12 (dd, *J* = 7.6, 5.2 Hz, 1H), 2.43 (s, 3H), 2.34 - 2.02 (m, 4H), 1.90 (s, 3H), 1.70 (s, 3H), 1.63 (s, 3H), 1.34 (s, 3H); **^{13}C NMR** (101 MHz, $CDCl_3$) δ 170.4, 143.7, 138.2, 132.7, 129.4, 127.4, 122.7, 61.9, 54.8, 48.9, 34.7, 25.7, 25.5, 21.6, 20.5, 18.6, 17.7.

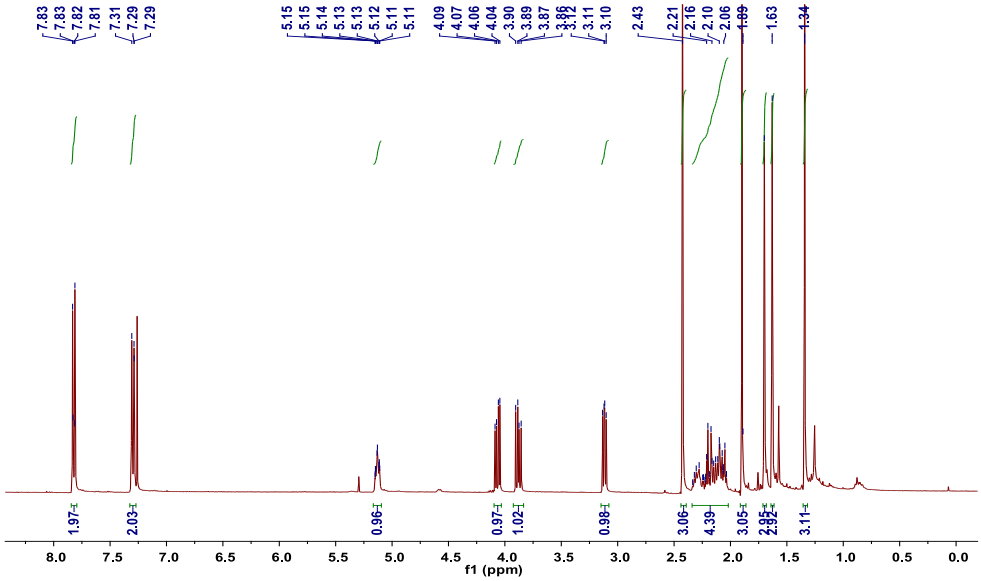

Figure S57. ^{1}H NMR spectrum of **19**, related to Scheme 1.

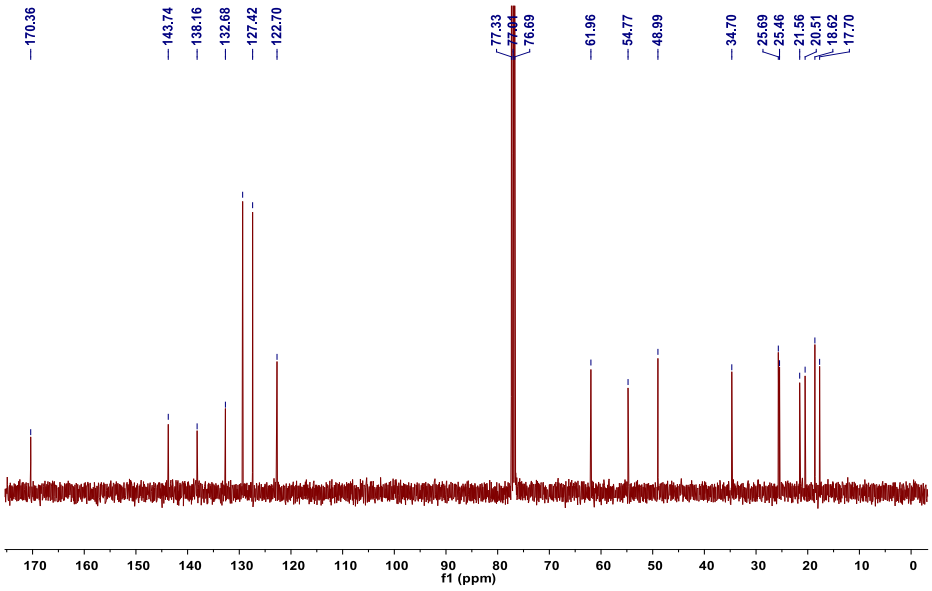

Figure S58. ^{13}C NMR spectrum of **19**, related to Scheme 1.

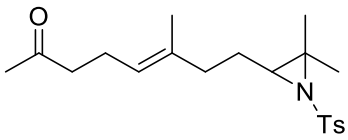

20: **^{1}H NMR** (400 MHz, $CDCl_3$) δ 7.82 - 7.77 (m, 2H), 7.28 (dd, *J* = 8.5, 0.6 Hz, 2H), 5.24 - 5.17 (m, 1H), 4.52 (d, *J* = 7.1 Hz, 2H), 2.78 (dd, *J* = 7.5, 5.8 Hz, 1H), 2.41 (s, 3H), 2.02 (s, 3H), 1.86 (dddd, *J* = 19.8, 14.5, 9.7, 6.0 Hz, 1H), 1.68 (s, 3H), 1.63 - 1.52 (m, 4H), 1.48 - 1.37 (m, 1H), 1.26 (s, 3H); **^{13}C NMR** (101 MHz, $CDCl_3$) δ 170.9, 143.6, 140.7, 138.4, 129.4, 127.4, 118.9, 61.1, 52.1, 51.8, 36.8, 26.0, 21.5, 21.3, 21.2, 20.9, 16.4.

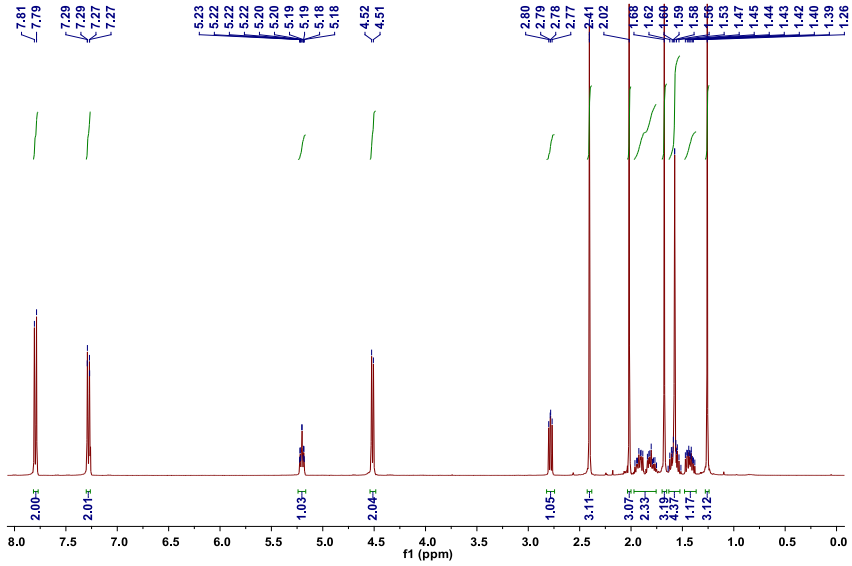

Figure S59. ^{1}H NMR spectrum of **20**, related to Scheme 1.

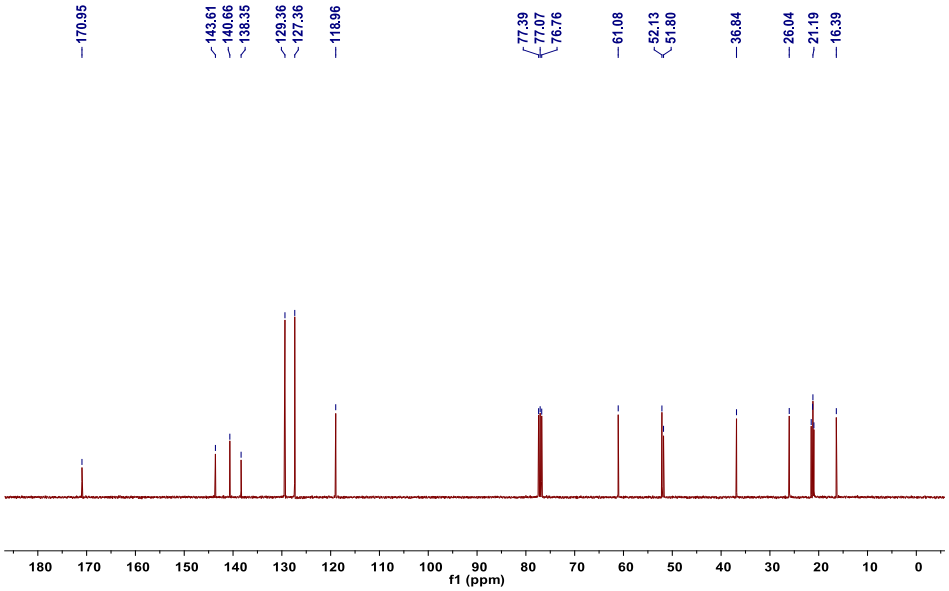

Figure S60. ^{13}C NMR spectrum of **20**, related to Scheme 1.

^{1}H and ^{13}C-NMR Spectra of cyclopropanation products

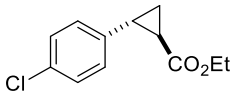

(Trans)

21: ^{1}H NMR (400 MHz, $CDCl_3$) δ 7.26 – 7.21 (m, 2H), 7.05 – 7.00 (m, 2H), 4.18 (tt, J = 7.2, 3.7 Hz, 2H), 2.49 (ddd, *J* = 9.2, 6.5, 4.2 Hz, 1H), 1.86 (ddd, *J* = 8.5, 5.3, 4.2 Hz, 1H), 1.60 (ddd, *J* = 9.2, 5.3, 4.6 Hz, 1H), 1.32 – 1.22 (m, 4H); ^{13}C NMR (101 MHz, $CDCl_3$) δ 173.1, 138.6, 132.2, 128.6, 127.6, 60.8, 25.5, 24.2, 16.9, 14.3.

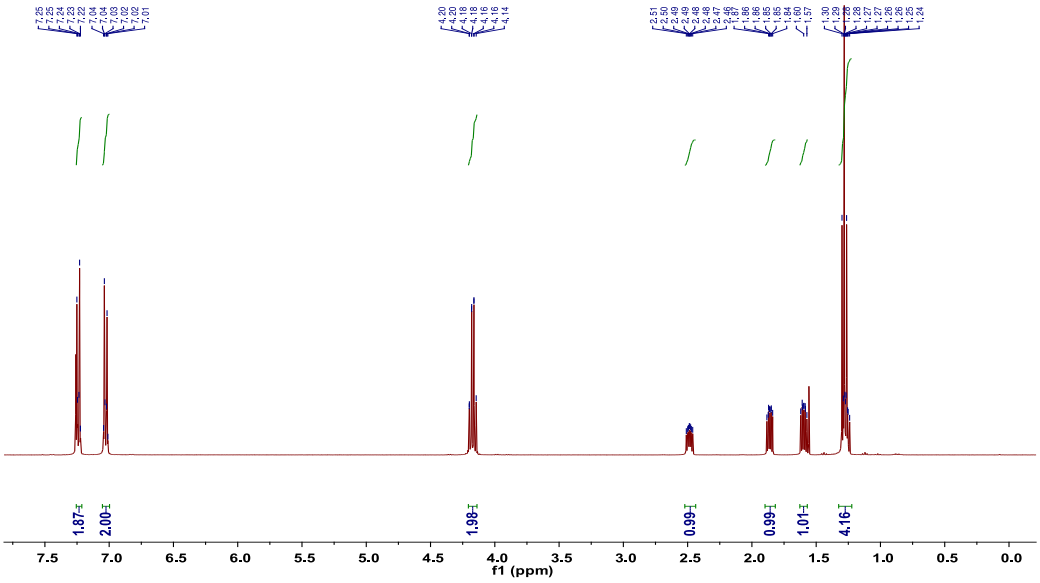

Figure S61. ^{1}H NMR spectrum of **21** ***trans***, related to Scheme 2.

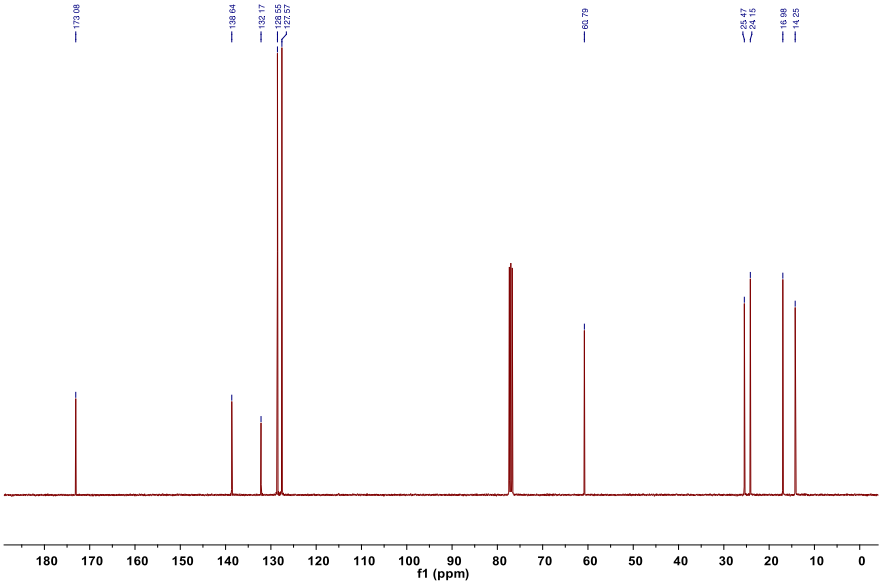

Figure S62. ^{13}C NMR spectrum of **21** ***trans***, related to Scheme 2.

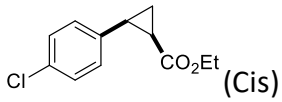

(Cis)

21: ^{1}H NMR (400 MHz, $CDCl_3$) δ 7.25 – 7.17 (m, 4H), 3.90 (q, J = 7.1 Hz, 2H), 2.52 (dd, J = 16.7, 8.7 Hz, 1H), 2.08 (ddd, J = 9.2, 7.9, 5.6 Hz, 1H), 1.70 – 1.63 (m, 1H), 1.39 – 1.31 (m, 1H), 1.02 (t, J = 7.1 Hz, 3H); **^{13}C NMR** (101 MHz, $CDCl_3$) δ 170.7, 135.1, 132.4, 130.6, 128.01, 60.3, 24.8, 21.8, 14.1, 11.3.

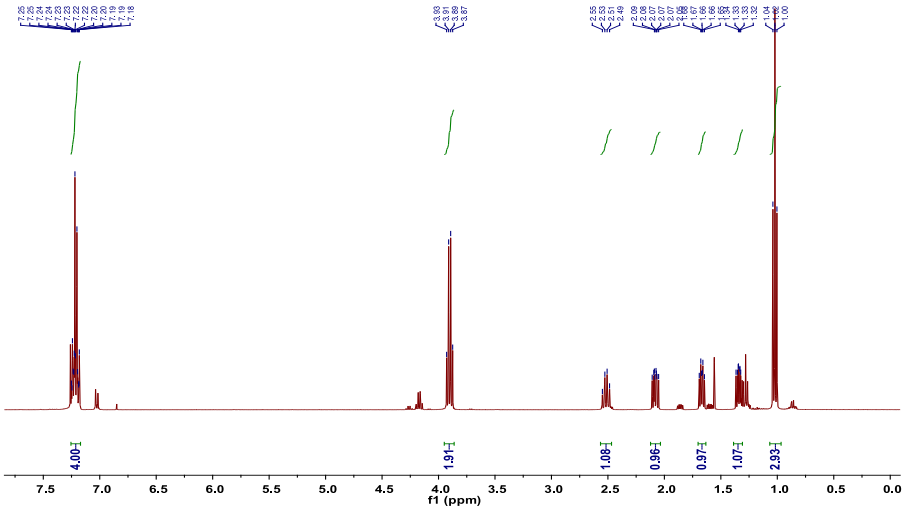

Figure S63. ^{1}H NMR spectrum of **21** ***cis***, related to Scheme 2.

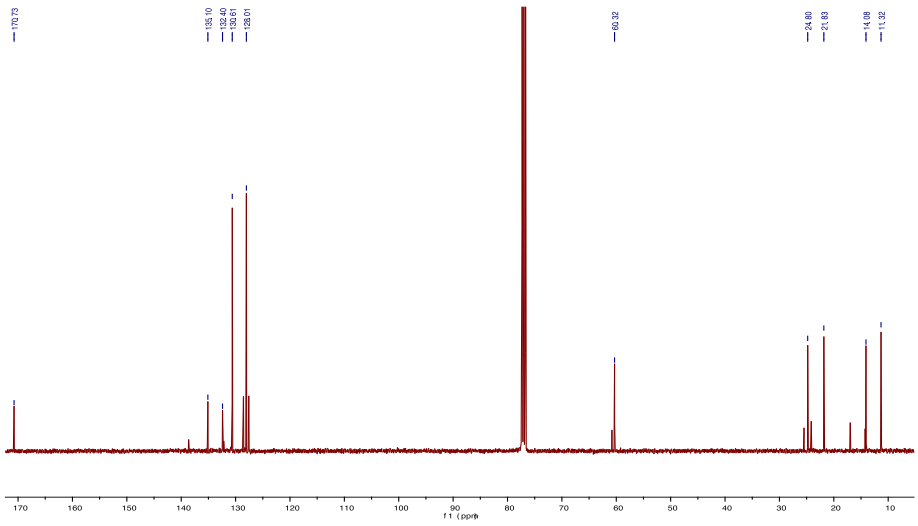

Figure S64. ^{13}C NMR spectrum of **21** ***cis***, related to Scheme 2.

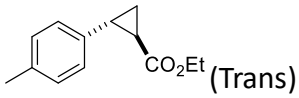

22: ^{1}H NMR (400 MHz, $CDCl_3$) δ 7.08 – 7.10 (m, 2H), 7.04 – 6.96 (m, 2H), 4.17 (q, J = 7.1 Hz, 2H), 2.50 (ddd, J = 9.3, 6.5, 4.2 Hz, 1H), 2.32 (s, 3H), 1.87 (ddd, J = 8.4, 5.3, 4.2 Hz, 1H), 1.57 (ddd, J = 9.3, 5.3, 4.5 Hz, 1H), 1.33 – 1.24 (m, 4H); **^{13}C NMR** (101 MHz, $CDCl_3$) δ 173.5, 137.1, 136.1, 129.1, 126.1, 60.6, 25.9, 24.0, 20.9, 16.9, 14.3.

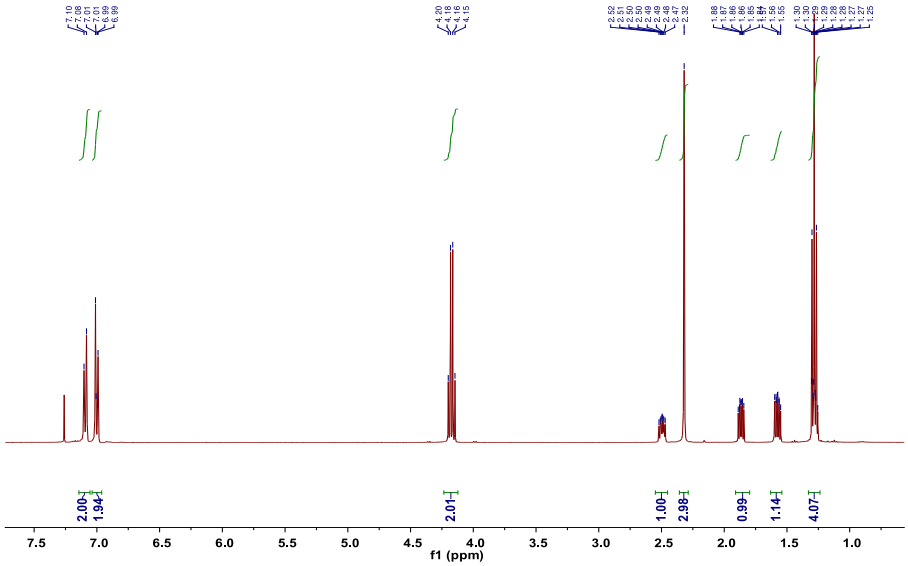

Figure S65. ^{1}H NMR spectrum of **22** ***trans***, related to Scheme 2.

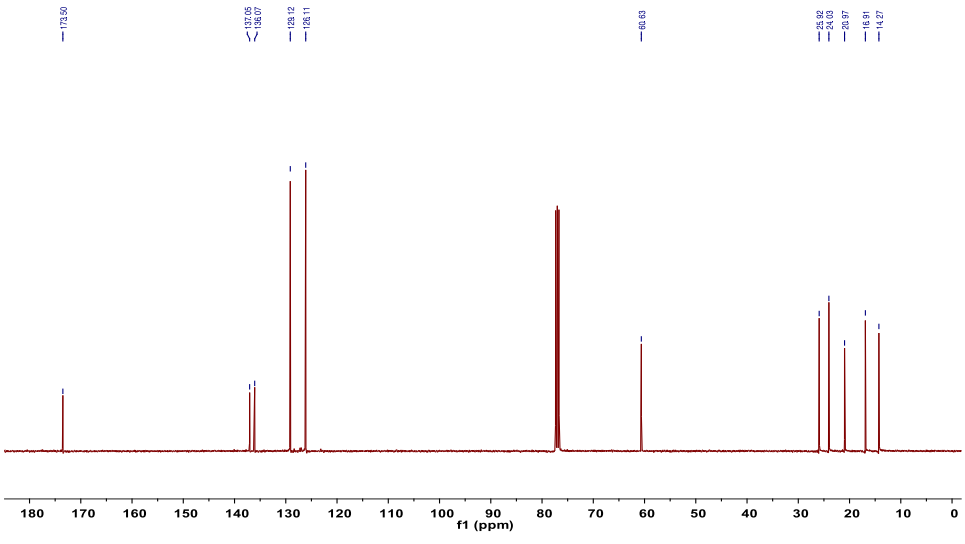

Figure S66. ^{13}C NMR spectrum of **22** ***trans***, related to Scheme 2.

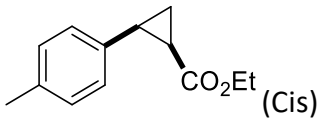

22: **^{1}H NMR** (400 MHz, $CDCl_3$) δ 7.15 (d, J = 8.0 Hz, 2H), 7.07 (d, J = 8.0 Hz, 2H), 3.89 (q, J = 7.1 Hz, 2H), 2.54 (dd, J = 16.8, 8.6 Hz, 1H), 2.30 (s, 3H), 2.05 (ddd, J = 9.2, 7.8, 5.6 Hz, 1H), 1.68 (dt, J = 7.5, 5.3 Hz, 1H), 1.34 – 1.26 (m, 1H), 1.01 (t, J = 7.1 Hz, 3H); **^{13}C NMR** (101 MHz, $CDCl_3$) δ 171.1, 136.1, 133.4, 129.1, 128.6, 60.1, 25.2, 21.7, 21.1, 14.1, 11.2.

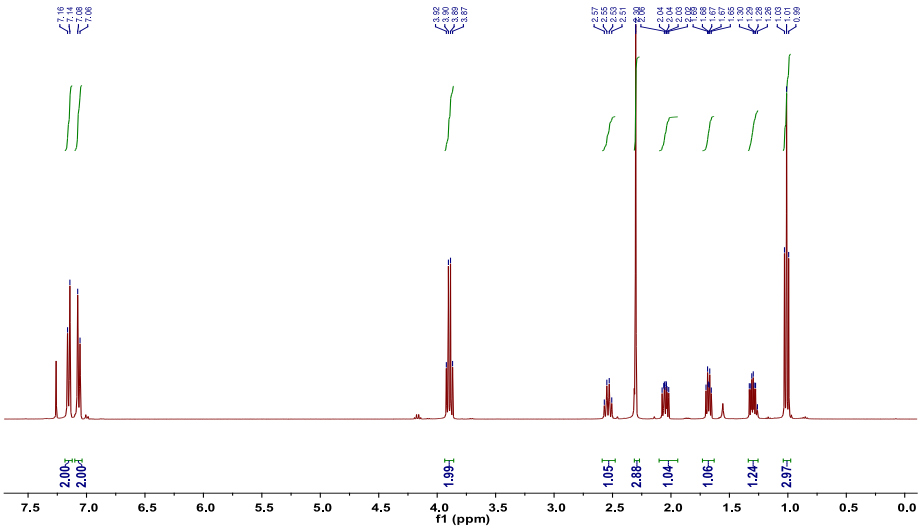

Figure S67. ^{1}H NMR spectrum of **22** ***cis***, related to Scheme 2.

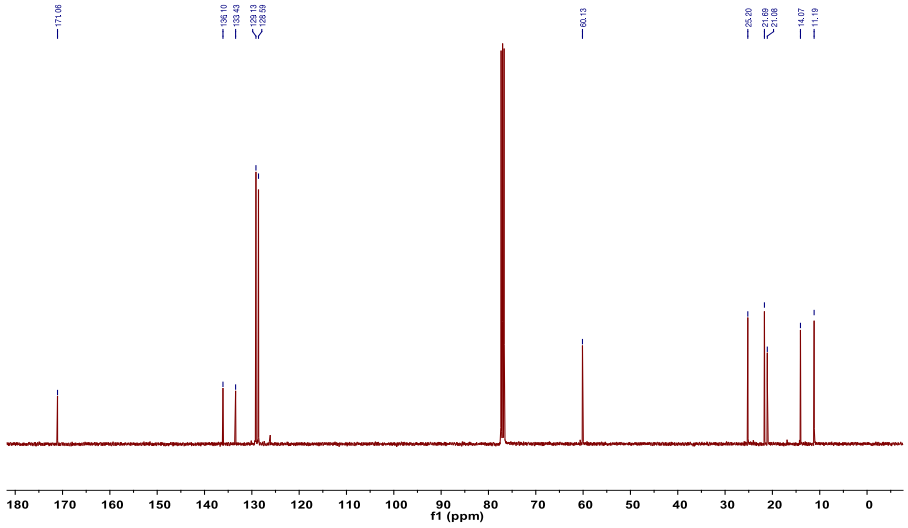

Figure S68. ^{13}C NMR spectrum of **22** ***cis***, related to Scheme 2.

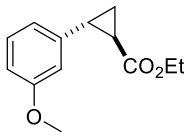

(Trans)

23: **^{1}H NMR** (300 MHz, $CDCl_3$) δ 7.19 (t, J = 7.9 Hz, 1H), 6.71 (ddd, J = 16.1, 8.1, 1.9 Hz, 3H), 4.17 (q, J = 7.1 Hz, 2H), 3.79 (s, 3H), 2.49 (ddd, J = 10.3, 6.5, 4.2 Hz, 1H), 1.90 (dt, J = 12.6, 4.8 Hz, 1H), 1.58 (dt, J = 9.6, 4.9 Hz, 1H), 1.29 (m, 4H); **^{13}C NMR** (75 MHz, $CDCl_3$) δ 173.4, 159.8, 141.8, 129.5, 118.5, 112.2, 111.8, 60.7, 55.2, 26.2, 24.2, 17.1, 14.3.

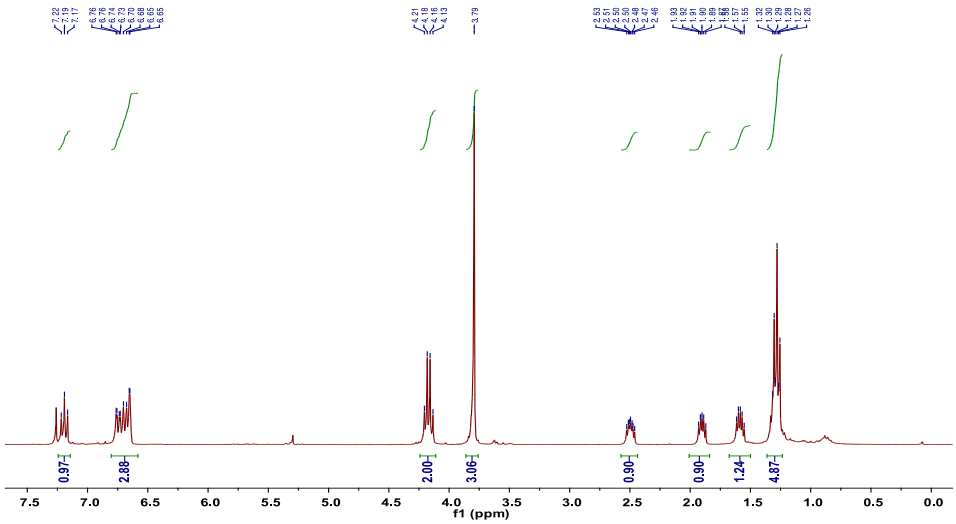

Figure S69. ^{1}H NMR spectrum of **23** ***trans***, related to Scheme 2.

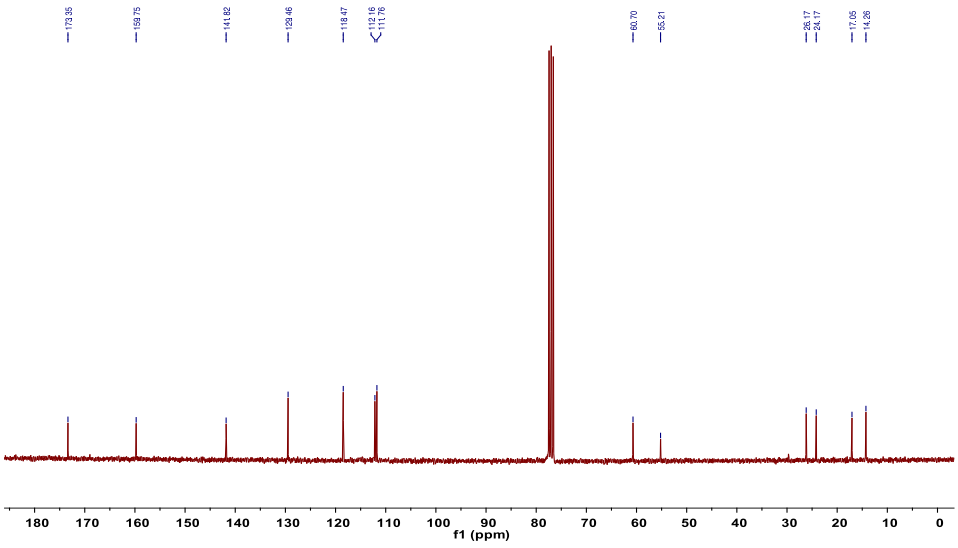

Figure S70. ^{13}C NMR spectrum of **23** ***trans***, related to Scheme 2.

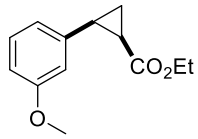

(Cis)

23: **^{1}H NMR** (400 MHz, $CDCl_3$) δ 7.17 (t, J = 7.9 Hz, 1H), 6.85 (ddd, J = 11.3, 6.0, 1.4 Hz, 2H), 6.74 (dd, J = 8.2, 2.6 Hz, 1H), 3.90 (q, J = 7.1 Hz, 2H), 3.78 (s, 3H), 2.55 (dd, J = 16.7, 8.7 Hz, 1H), 2.07 (ddd, J = 9.3, 7.8, 5.7 Hz, 1H), 1.69 (dt, J = 7.5, 5.4 Hz, 1H), 1.31 (ddd, J = 8.6, 7.9, 5.0 Hz, 1H), 1.00 (t, J = 7.1 Hz, 3H); **^{13}C NMR** (101 MHz, $CDCl_3$) δ 170.9, 159.3, 138.2, 128.8, 121.7, 115.0, 112.2, 60.2, 55.1, 25.5, 21.8, 14.1, 11.2.

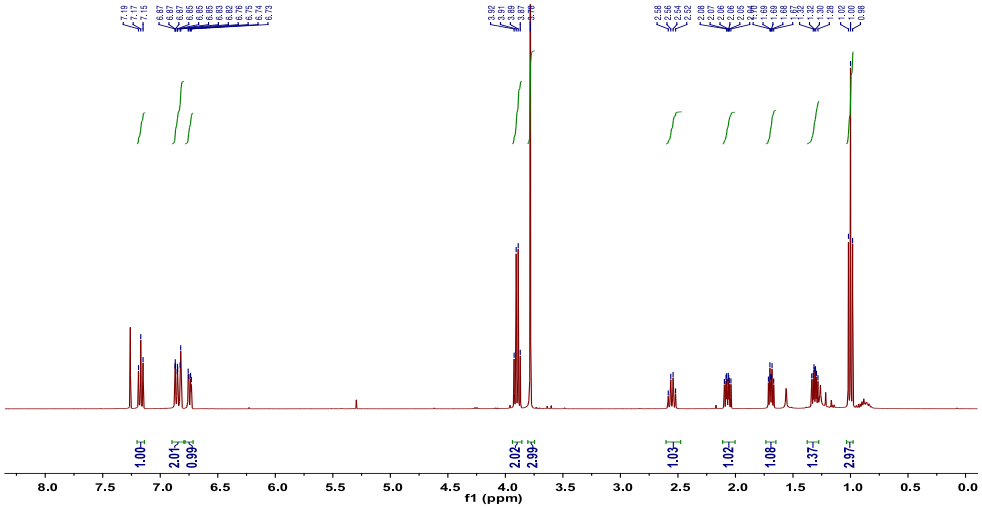

Figure S71. ^{1}H NMR spectrum of **23** ***cis***, related to Scheme 2.

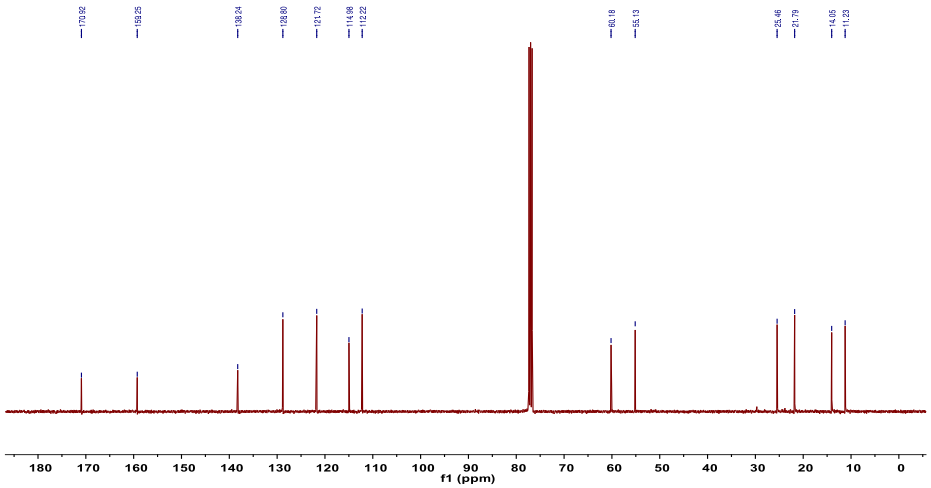

Figure S72. ^{13}C NMR spectrum of **23** ***cis***, related to Scheme 2.

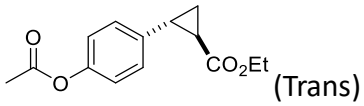

(Trans)

24: ^{1}H NMR (400 MHz, $CDCl_3$) δ 7.14 – 7.08 (m, 2H), 7.03 – 6.97 (m, 2H), 4.17 (q, *J* = 7.1 Hz, 2H), 2.51 (ddd, *J* = 9.3, 6.5, 4.2 Hz, 1H), 2.28 (s, 3H), 1.87 (ddd, *J* = 8.4, 5.3, 4.2 Hz, 1H), 1.59 (ddd, *J* = 9.3, 5.3, 4.6 Hz, 1H), 1.36 – 1.22 (m, 4H); **^{13}C NMR** (101 MHz, $CDCl_3$) δ 173.2, 169.5, 149.2, 137.7, 127.3, 121.6, 60.7, 25.6, 24.1, 21.1, 16.9, 14.3.

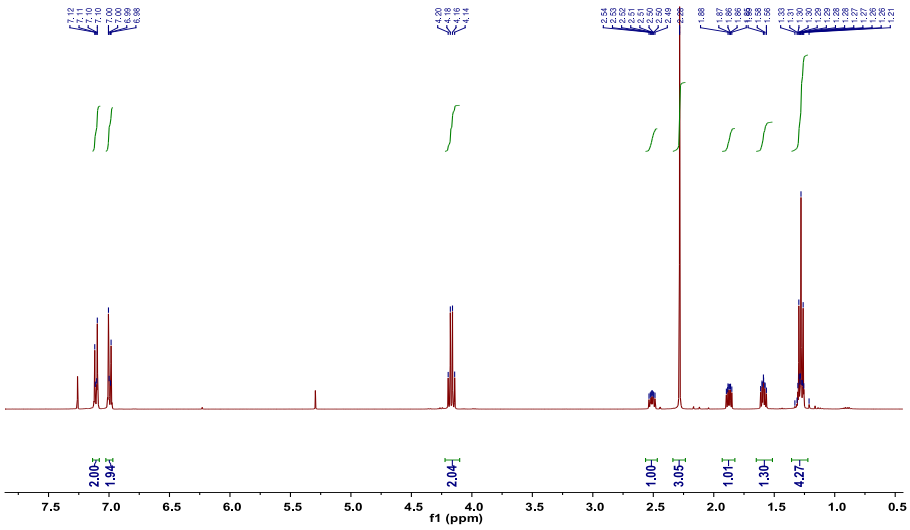

Figure S73. ^{1}H NMR spectrum of **24** ***trans***, related to Scheme 2.

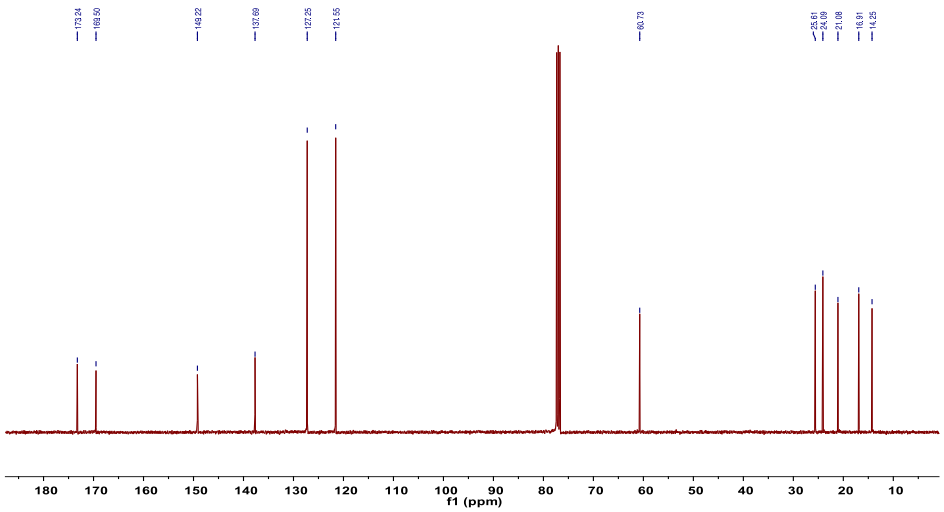

Figure S74. ^{13}C NMR spectrum of **24** ***trans***, related to Scheme 2.

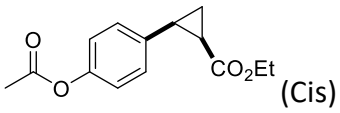

(Cis)

24: **^{1}H NMR** (400 MHz, $CDCl_3$) δ 7.29 – 7.24 (m, 2H), 7.01 – 6.96 (m, 2H), 3.94 – 3.83 (m, 2H), 2.54 (dd, J = 16.7, 8.7 Hz, 1H), 2.27 (s, 3H), 2.13 – 2.02 (m, 1H), 1.72 – 1.64 (m, 1H), 1.33 (ddd, J = 8.7, 7.9, 5.1 Hz, 1H), 0.98 (t, J = 7.1 Hz, 3H); **^{13}C NMR** (101 MHz, $CDCl_3$) δ 170.8, 169.4, 149.4, 134.2, 130.2, 120.9, 60.3, 24.8, 21.9, 21.1, 14.0, 11.3.

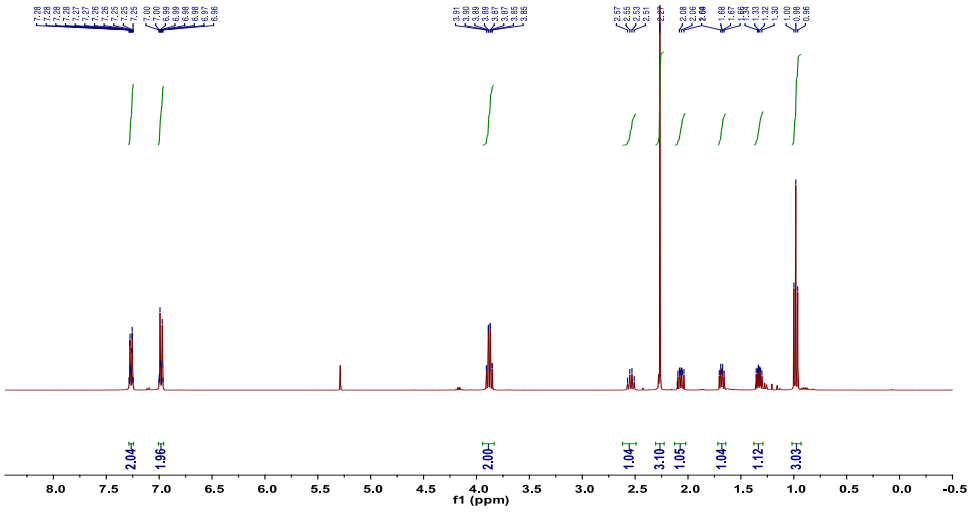

Figure S75. ^{1}H NMR spectrum of **24** ***cis***, related to Scheme 2.

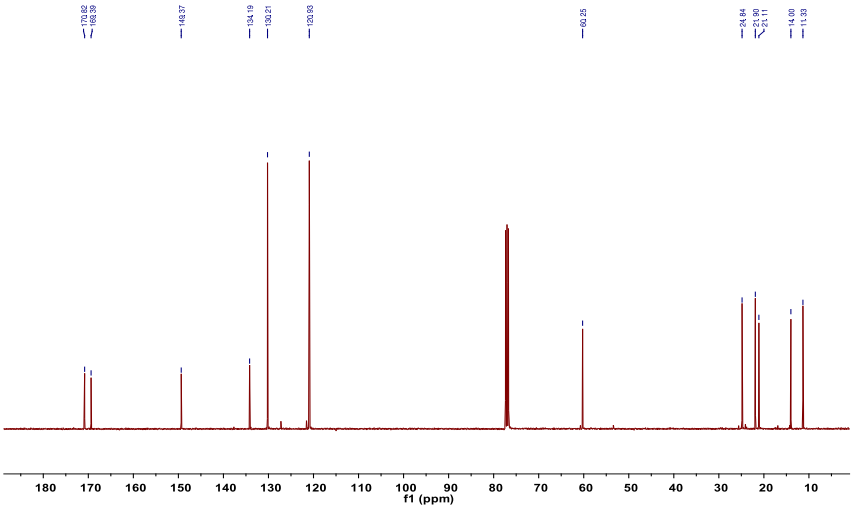

Figure S76. ^{13}C NMR spectrum of **24** ***cis***, related to Scheme 2.

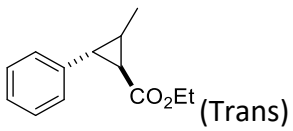

(Trans)

25: **^{1}H NMR** (400 MHz, $CDCl_3$) δ 7.31 – 7.24 (m, 2H), 7.22 – 7.16 (m, 1H), 7.09 (dd, *J* = 5.2, 3.3 Hz, 2H), 4.18 (qd, *J* = 7.1, 1.9 Hz, 2H), 2.42 (dd, *J* = 6.4, 5.1 Hz, 1H), 2.02 (dd, *J* = 9.2, 5.0 Hz, 1H), 1.72 – 1.65 (m, 1H), 1.36 (d, *J* = 6.2 Hz, 3H), 1.29 (t, *J* = 7.1 Hz, 3H); **^{13}C NMR** (101 MHz, $CDCl_3$) δ 171.6, 140.6, 128.4, 126.2, 126.0, 60.4, 32.4, 29.4, 25.5, 14.4, 12.0.

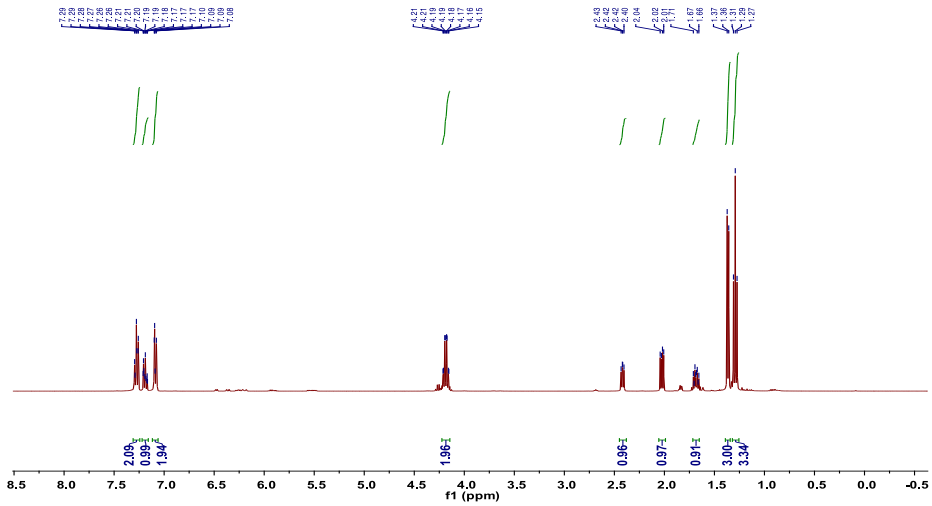

Figure S77. ^{1}H NMR spectrum of **25** ***trans***, related to Scheme 2.

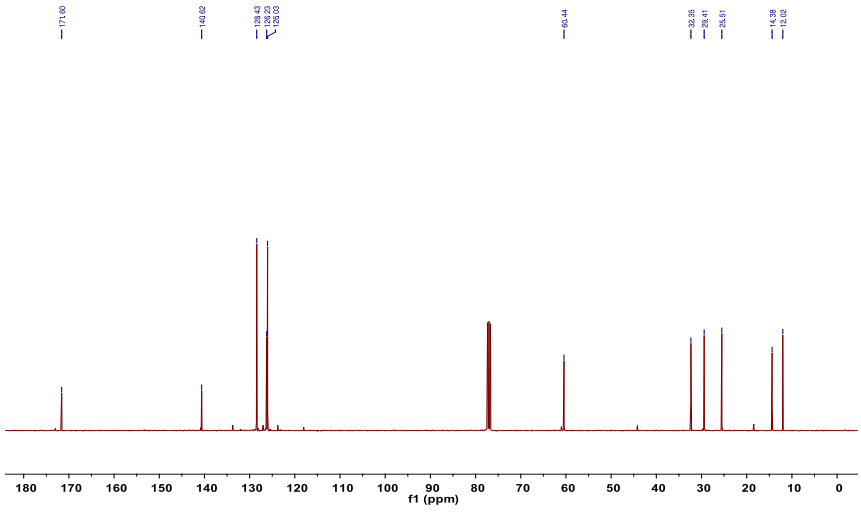

Figure S78. ^{13}C NMR spectrum of **25** ***trans***, related to Scheme 2.

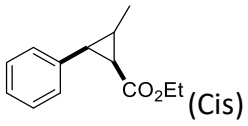

25: **^{1}H NMR** (400 MHz, $CDCl_3$) δ 7.26 – 7.22 (m, 4H), 7.21 – 7.15 (m, 1H), 3.87 (q, J = 7.1 Hz, 2H), 2.35 (dd, J = 9.3, 6.9 Hz, 1H), 2.13 – 2.02 (m, 1H), 1.82 (dd, J = 9.3, 5.1 Hz, 1H), 1.28 (d, J = 6.1 Hz, 3H), 0.98 (t, J = 7.1 Hz, 3H); **^{13}C NMR** (101 MHz, $CDCl_3$) δ 170.9, 136.8, 129.1, 127.8, 126.5, 60.1, 34.2, 30.1, 19.7, 17.7, 14.0.

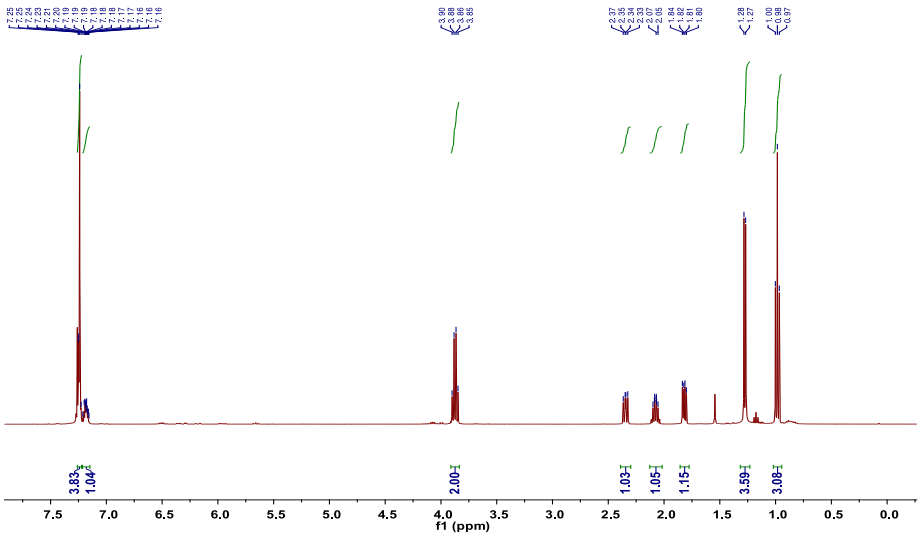

Figure S79. ^{1}H NMR spectrum of **25** ***cis***, related to Scheme 2.

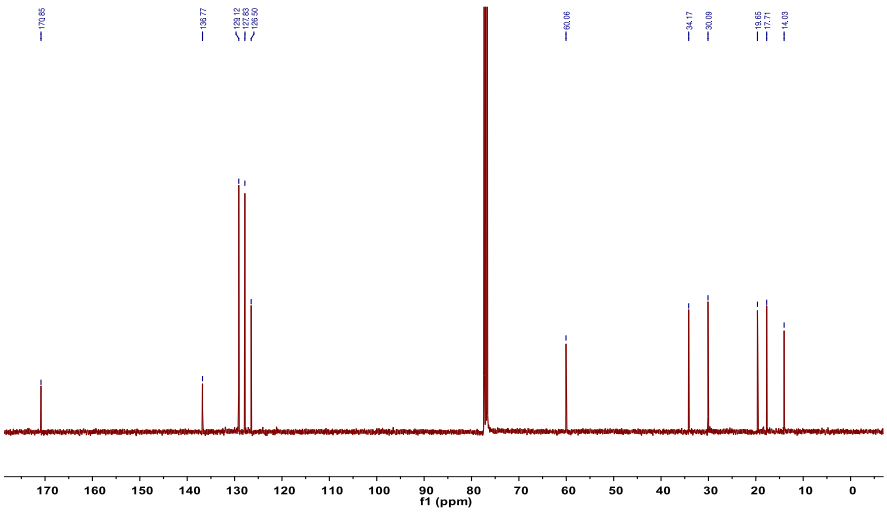

Figure S80. ^{13}C NMR spectrum of **25** ***cis***, related to Scheme 2.

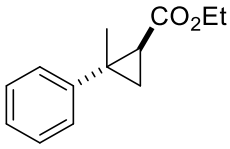

(Trans)

26: ^{1}H NMR (400 MHz, $CDCl_3$) δ 7.35 – 7.28 (m, 4H), 7.25 – 7.19 (m, 1H), 4.28 – 4.16 (m, 2H), 1.99 (dd, *J* = 8.3, 6.0 Hz, 1H), 1.55 (s, 3H), 1.45 (ddd, *J* = 13.0, 7.1, 4.7 Hz, 2H), 1.32 (t, *J* = 7.1 Hz, 3H); **^{13}C NMR** (101 MHz, $CDCl_3$) δ 172.2, 145.9, 128.5, 127.3, 126.4, 60.5, 30.6, 27.9, 20.8, 19.9, 14.4.

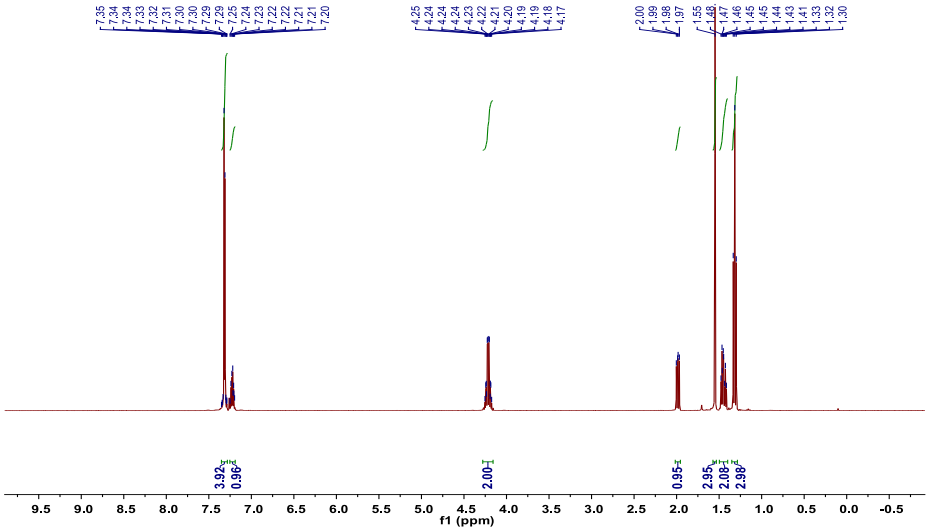

Figure S81. ^{1}H NMR spectrum of **26** ***trans***, related to Scheme 2.

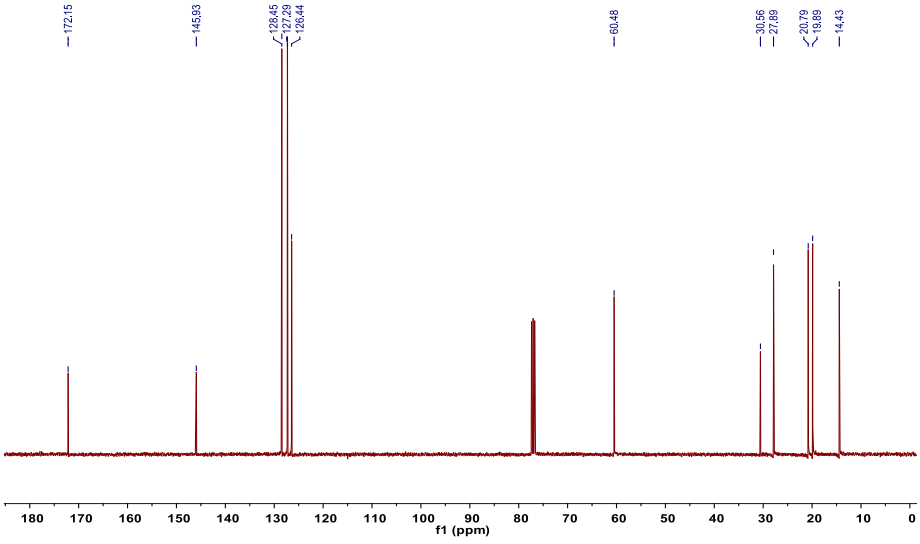

Figure S82. ^{13}C NMR spectrum of **26** ***trans***, related to Scheme 2.

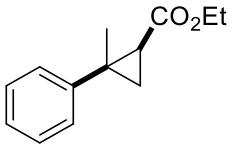

(Cis)

26: ^{1}H NMR (400 MHz, $CDCl_3$) δ 7.32 – 7.24 (m, 4H), 7.20 (dqd, J = 4.8, 4.1, 2.8 Hz, 1H), 3.91 – 3.77 (m, 2H), 1.91 (dd, J = 7.8, 5.4 Hz, 1H), 1.81 – 1.75 (m, 1H), 1.47 (s, 3H), 1.15 (dd, J = 7.8, 4.6 Hz, 1H), 0.95 (t, J = 7.1 Hz, 3H); **^{13}C NMR** (101 MHz, $CDCl_3$) δ 171.2, 141.9, 128.8, 128.1, 126.6, 60.1, 32.0, 28.6, 28.6, 19.4, 13.9.

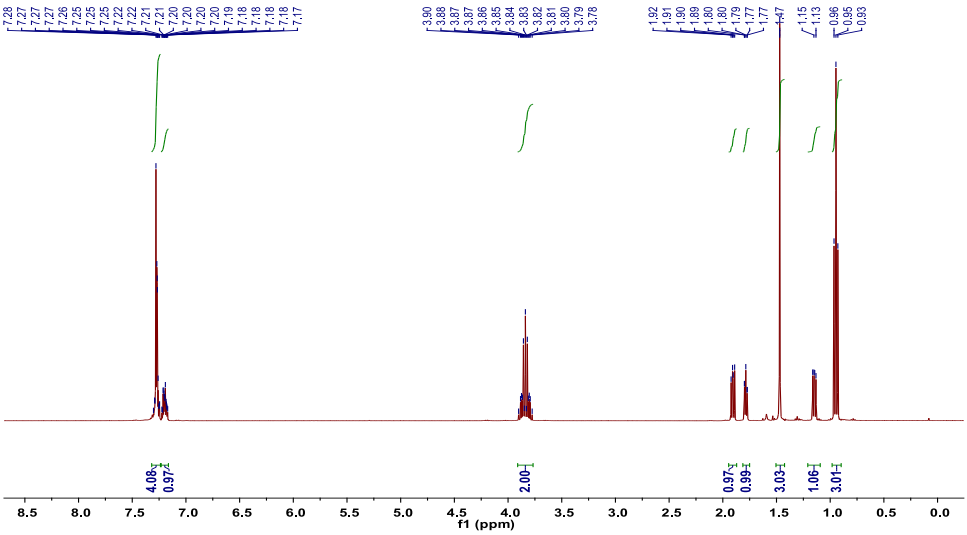

Figure S83. ^{1}H NMR spectrum of **26** ***cis***, related to Scheme 2.

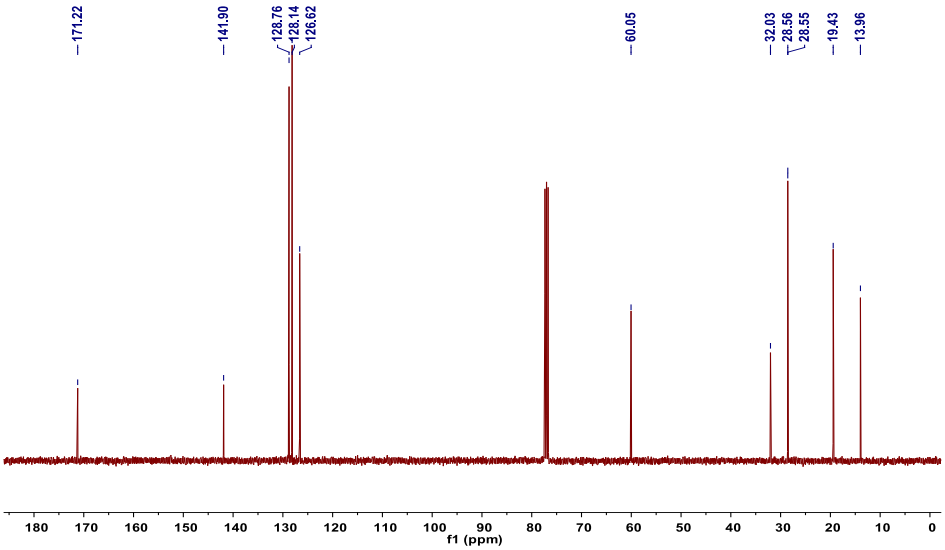

Figure S84. ^{13}C NMR spectrum of **26** ***cis***, related to Scheme 2.

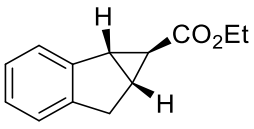

(Trans)

27: ^{1}H NMR (400 MHz, $CDCl_3$) δ 7.38 – 7.31 (m, 1H), 7.21 – 7.10 (m, 3H), 4.16 (q, *J* = 7.1 Hz, 2H), 3.28 (dd, *J* = 17.6, 6.4 Hz, 1H), 3.12 – 3.01 (m, 1H), 2.96 (ddd, *J* = 6.5, 2.4, 1.4 Hz, 1H), 2.45 (tdd, *J* = 6.5, 3.3, 0.6 Hz, 1H), 1.28 (t, *J* = 7.1 Hz, 3H), 1.24 – 1.19 (m, 1H); **^{13}C NMR** (101 MHz, $CDCl_3$) δ 172.7, 143.7, 141.8, 126.4, 126.3, 125.2, 123.9, 60.5, 35.4, 34.3, 30.8, 26.4, 14.3.

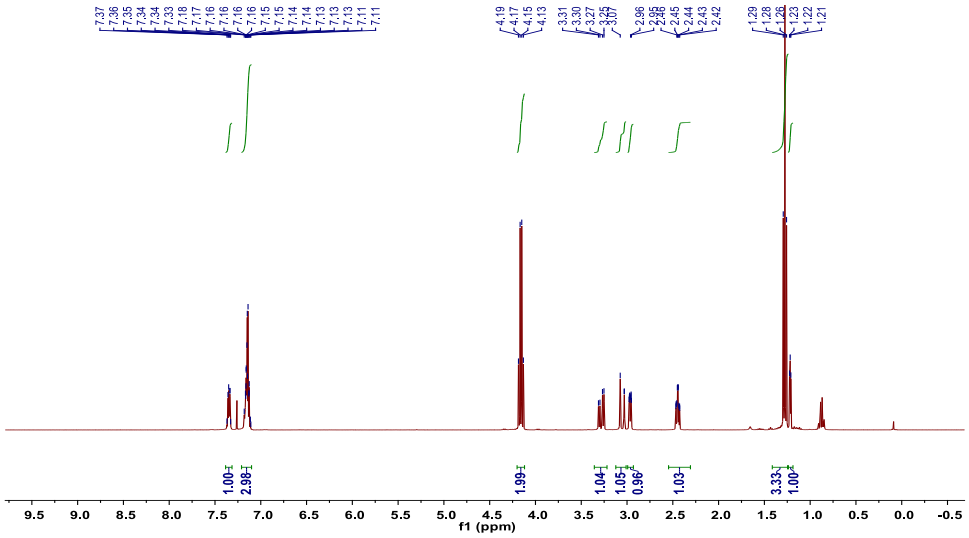

Figure S85. ^{1}H NMR spectrum of **27** ***trans***, related to Scheme 2.

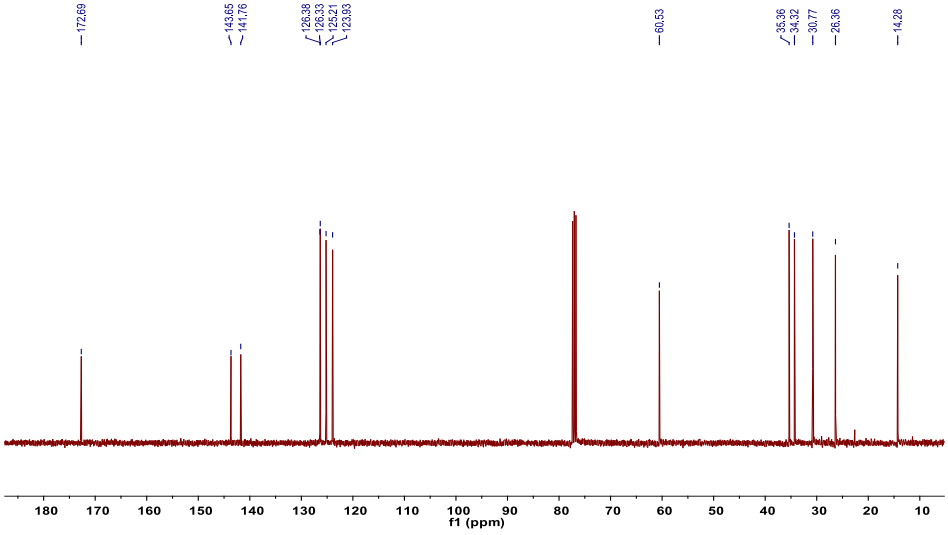

Figure S86. ^{13}C NMR spectrum of **27** ***trans***, related to Scheme 2.

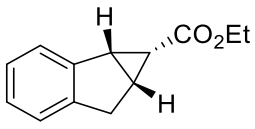

(Cis)

27: ^{1}H NMR (400 MHz, $CDCl_3$) δ 7.36 – 7.27 (m, 1H), 7.18 – 7.08 (m, 3H), 3.83 (q, J = 7.1 Hz, 2H), 3.36 (d, J = 17.3 Hz, 1H), 3.21 (dd, J = 17.2, 6.8 Hz, 1H), 2.99 – 2.91 (m, 1H), 2.27 (dtd, J = 7.8, 7.0, 0.9 Hz, 1H), 2.01 (t, J = 8.2 Hz, 1H), 0.95 (t, J = 7.1 Hz, 3H); **^{13}C NMR** (101 MHz, $CDCl_3$) δ 169.6, 144.7, 139.9, 126.5, 126.0, 124.6, 123.9, 59.9, 32.4, 31.6, 24.7, 23.6, 13.9.

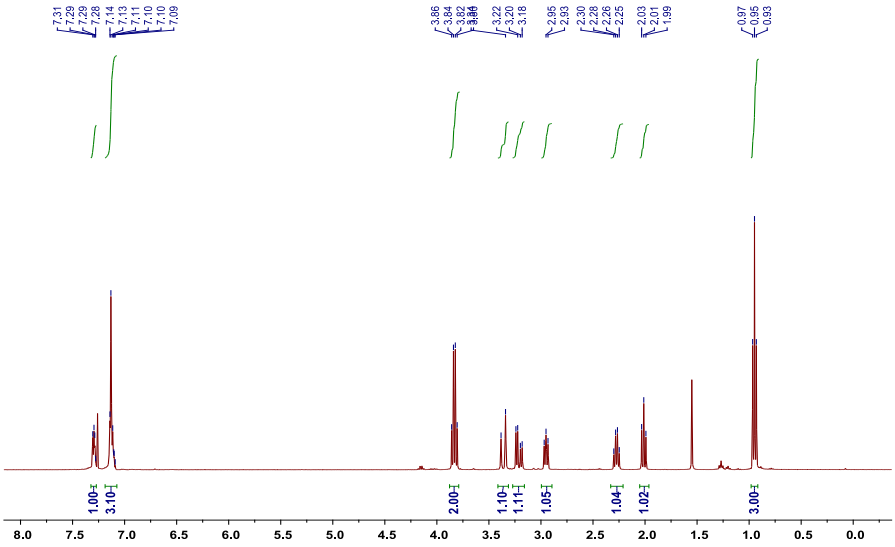

Figure S87. ^{1}H NMR spectrum of **27** ***cis***, related to Scheme 2.

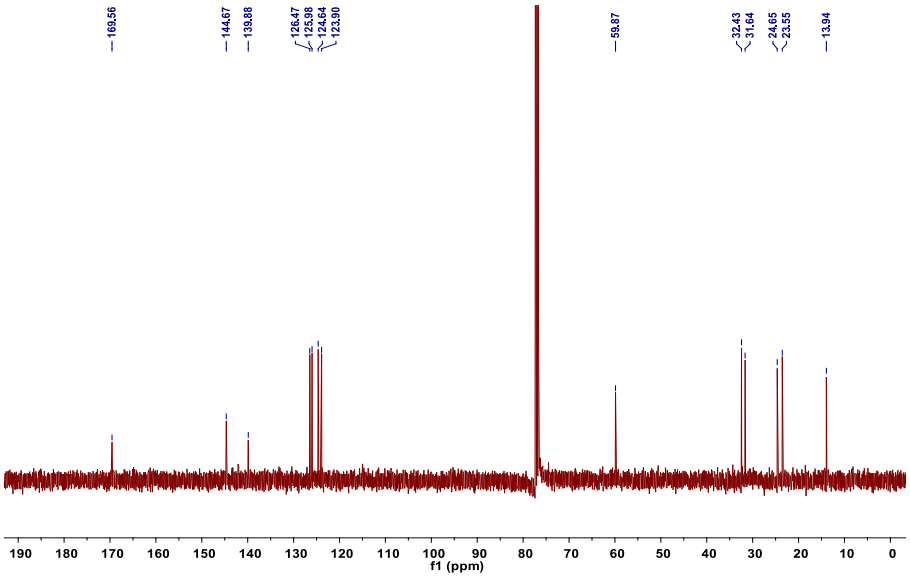

Figure S88. ^{13}C NMR spectrum of **27** ***cis***, related to Scheme 2.

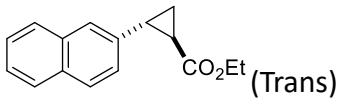

(Trans)

28: ^{1}H NMR (300 MHz, $CDCl_3$) δ 7.78 (t, J = 8.8 Hz, 2H), 7.58 (s, 1H), 7.45 (pd, J = 6.8, 3.4 Hz, 2H), 7.21 (dd, J = 8.5, 1.7 Hz, 1H), 4.20 (q, J = 7.2 Hz, 2H), 2.76 – 2.59 (m, 1H), 2.08 – 1.96 (m, 1H), 1.68 (dt, J = 9.7, 4.9 Hz, 1H), 1.43 (ddd, J = 8.4, 6.5, 4.6 Hz, 1H), 1.30 (t, J = 7.1 Hz, 3H); **^{13}C NMR** (75 MHz, $CDCl_3$) δ 173.4, 137.5, 133.4, 132.3, 128.2, 127.6, 127.4, 126.3, 125.5, 124.8, 124.6, 60.8, 26.4, 24.1, 17.0, 14.3.

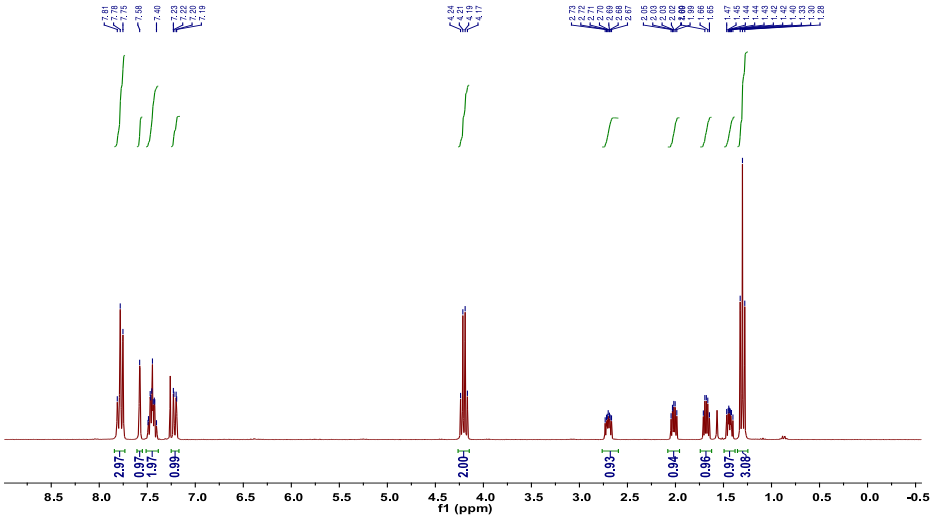

Figure S89. ^{1}H NMR spectrum of **28** ***trans***, related to Scheme 2.

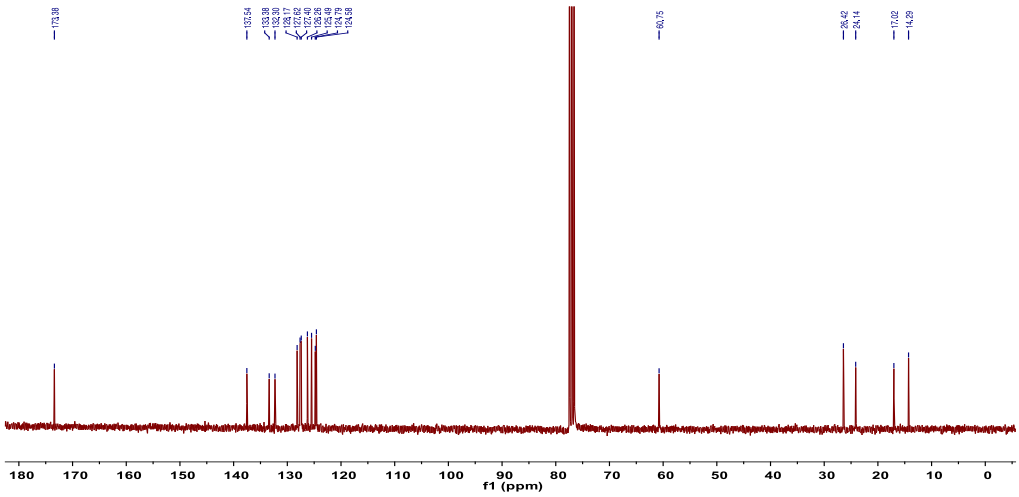

Figure S90. ^{13}C NMR spectrum of **28** ***trans***, related to Scheme 2.

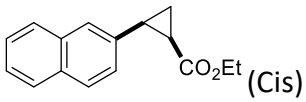

28: **^{1}H NMR** (400 MHz, $CDCl_3$) δ 7.85 – 7.63 (m, 4H), 7.49 – 7.32 (m, 3H), 3.84 (q, J = 7.1 Hz, 2H), 2.73 (dd, J = 17.0, 8.4 Hz, 1H), 2.16 (ddd, J = 9.3, 7.8, 5.6 Hz, 1H), 1.93 – 1.76 (m, 1H), 1.42 (ddd, J = 8.6, 7.8, 5.1 Hz, 1H), 0.92 (t, J = 7.1 Hz, 3H); **^{13}C NMR** (101 MHz, $CDCl_3$) δ 170.9, 134.1, 133.6, 133.2, 132.4, 127.9, 127.7, 127.6, 127.4, 125.9, 125.4, 60.1, 25.7, 22.0, 14.0, 11.4.

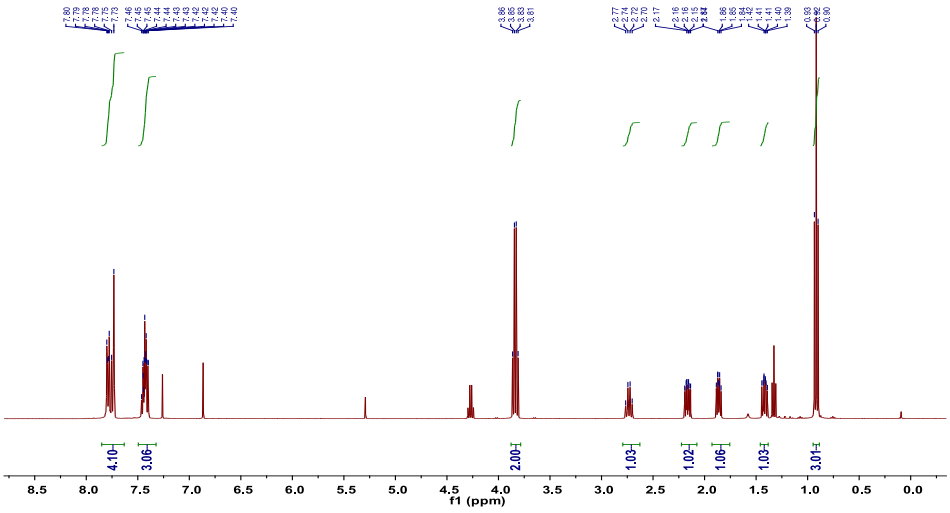

Figure S91. ^{1}H NMR spectrum of **28** ***cis***, related to Scheme 2.

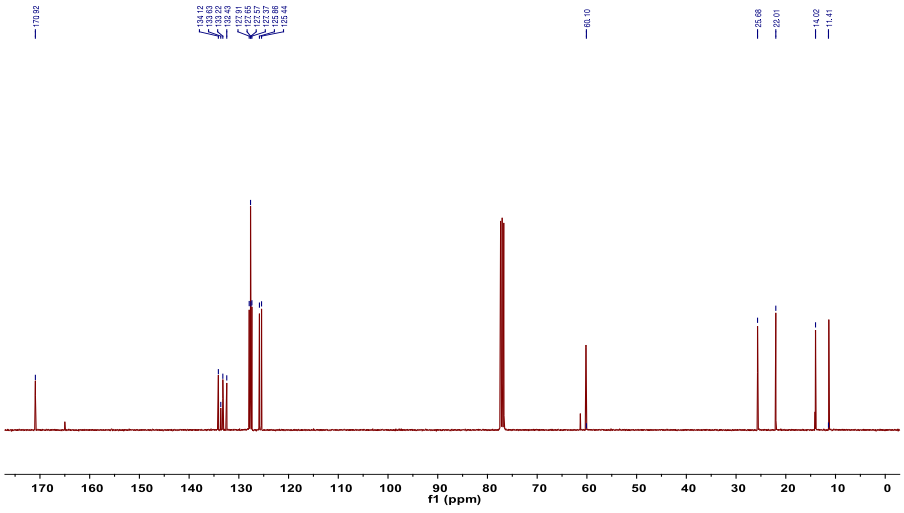

Figure S92. ^{13}C NMR spectrum of **28** ***cis***, related to Scheme 2.

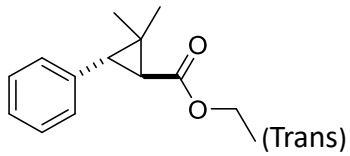

29: ^{1}H NMR (400 MHz, $CDCl_3$) δ 7.29 (tt, *J* = 8.1, 1.5 Hz, 1H), 7.24 – 7.14 (m, 1H), 4.19 (qd, *J* = 7.1, 2.4 Hz, 1H), 2.70 (d, *J* = 5.9 Hz, 0H), 1.96 (d, *J* = 5.9 Hz, 0H), 1.39 (s, 1H), 1.31 (t, *J* = 7.1 Hz, 1H), 0.93 (s, 3H); **^{13}C NMR** (101 MHz, CDCl3) δ 172.3, 137.4, 128.8, 128.1, 126.3, 60.4, 37.4, 31.6, 29.2, 21.9, 20.7, 14.4.

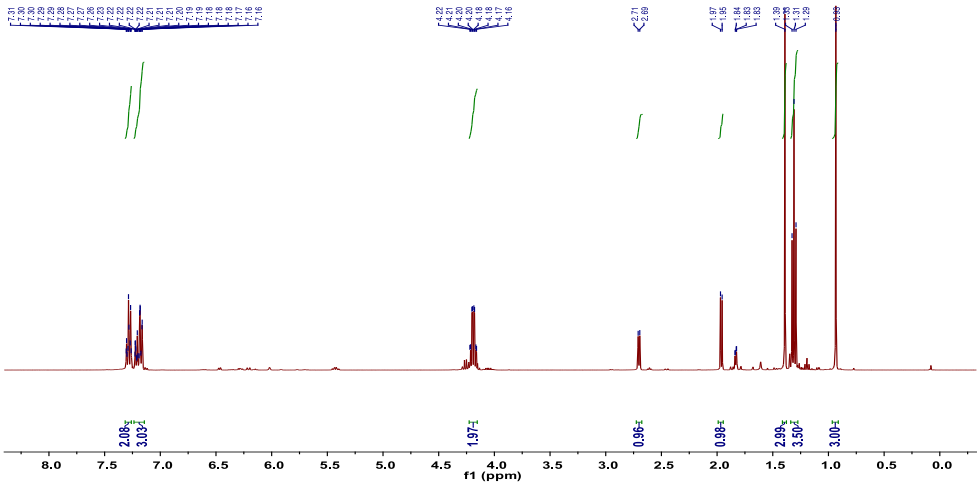

Figure S93. ^{1}H NMR spectrum of **29** ***trans***, related to Scheme 2.

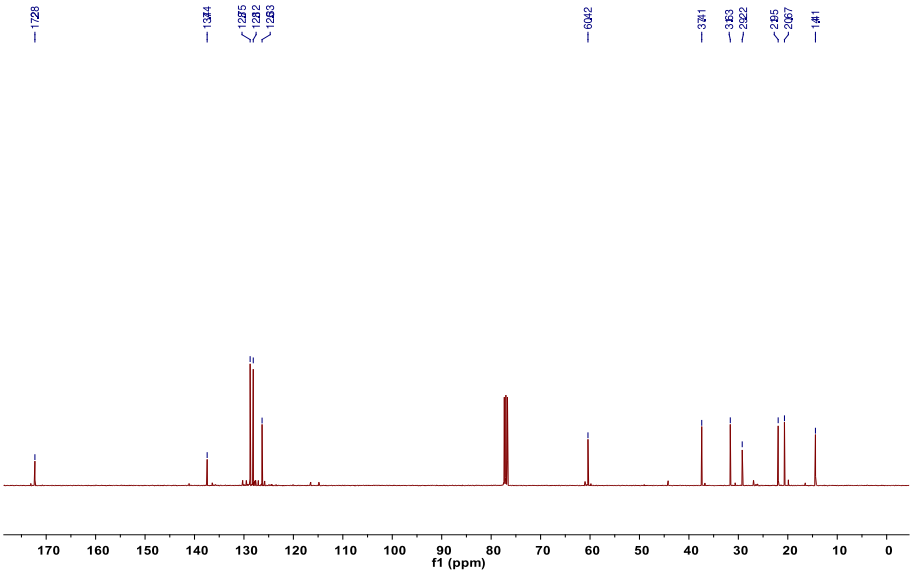

Figure S94. ^{13}C NMR spectrum of **29** ***trans***, related to Scheme 2.

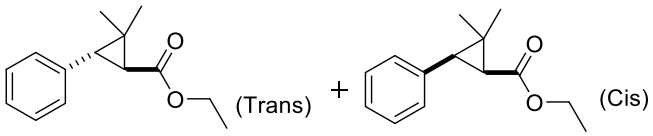

29: ^{1}H NMR (400 MHz, $CDCl_3$) δ 7.33 – 7.10 (m, trans and cis H), 4.19 (qd, trans H), 4.05 (dtd, cis H), 2.70 (d, trans H), 2.45 (d, cis H), 1.96 (d, trans H), 1.86 (d, cis H), 1.55 (s, cis H), 1.39 (s, trans H), 1.35 (s, cis H), 1.31 (t, trans H), 1.19 (t, cis H), 0.93 (s, trans H).

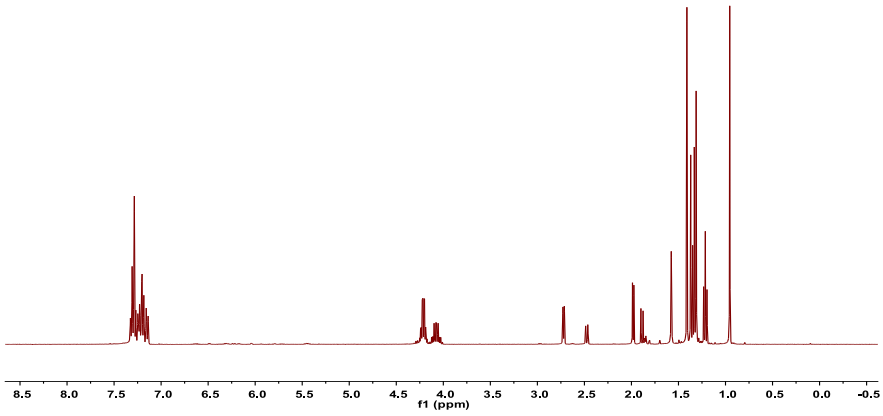

Figure S95. ^{1}H NMR spectrum of **29 cis** and ***trans***, related to Scheme 2.

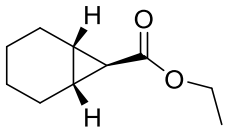

(Trans)

30: ^{1}H NMR (400 MHz, CDCl3) *δ* 4.11 (q, J = 7.1 Hz, 2H), 1.91 (dddd, J = 9.9, 7.4, 4.0, 2.0 Hz, 2H), 1.77 – 1.66 (m, 2H), 1.60 (ddd, J = 5.5, 3.9, 1.0 Hz, 2H), 1.39 (t, J = 4.3 Hz, 1H), 1.35 – 1.24 (m, 5H), 1.24 – 1.12 (m, 2H); **^{13}C NMR** (101 MHz, CDCl3) δ 174.8, 60.1, 25.7, 22.7, 22.1, 20.9, 14.3.

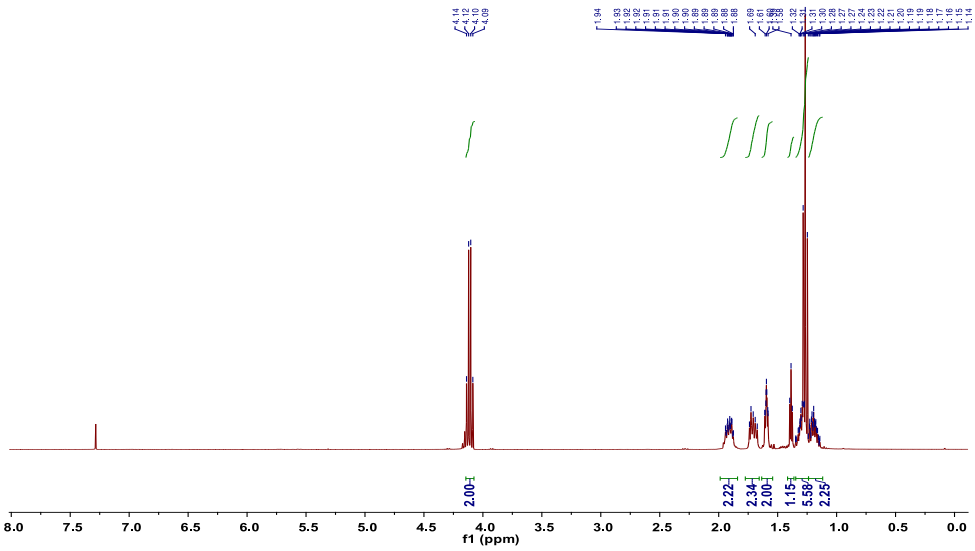

Figure S96. ^{1}H NMR spectrum of **30** ***trans***, related to Scheme 2.

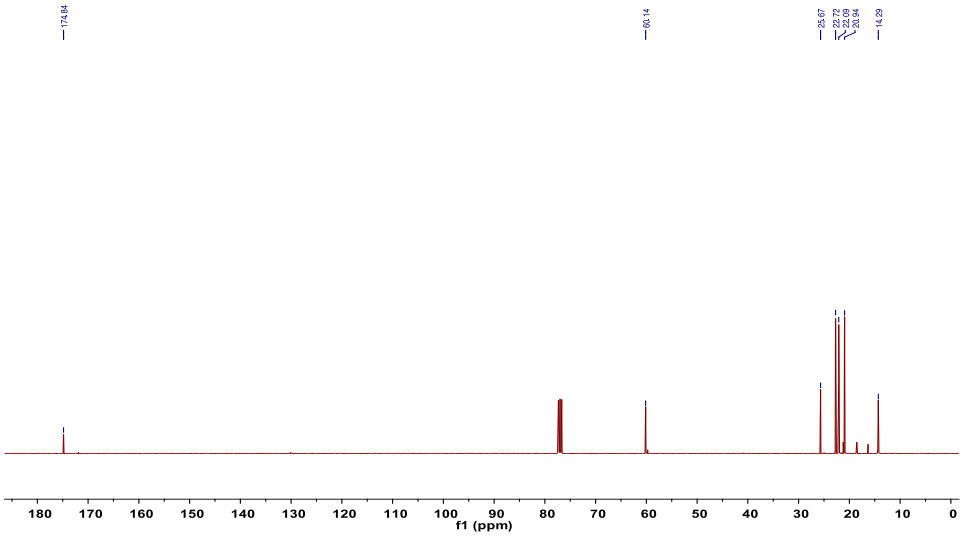

Figure S97. ^{13}C NMR spectrum of **30** ***trans***, related to Scheme 2.

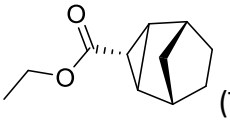

(Trans)

31: ^{1}H NMR (400 MHz, $CDCl_3$) δ 4.08 (q, J = 7.1 Hz, 2H), 2.35 (s, 2H), 1.52 (t, J = 2.5 Hz, 1H), 1.49 – 1.41 (m,2H), 1.37 – 1.27 (m, 4H), 1.23 (t, J = 7.1 Hz, 3H), 0.94 – 0.85 (m, 1H), 0.67 (d, J = 10.8 Hz, 1H); **^{13}C NMR** (101 MHz, $CDCl_3$) δ 174.2, 60.2, 35.8, 28.7, 28.6, 25.9, 16.3, 14.3.

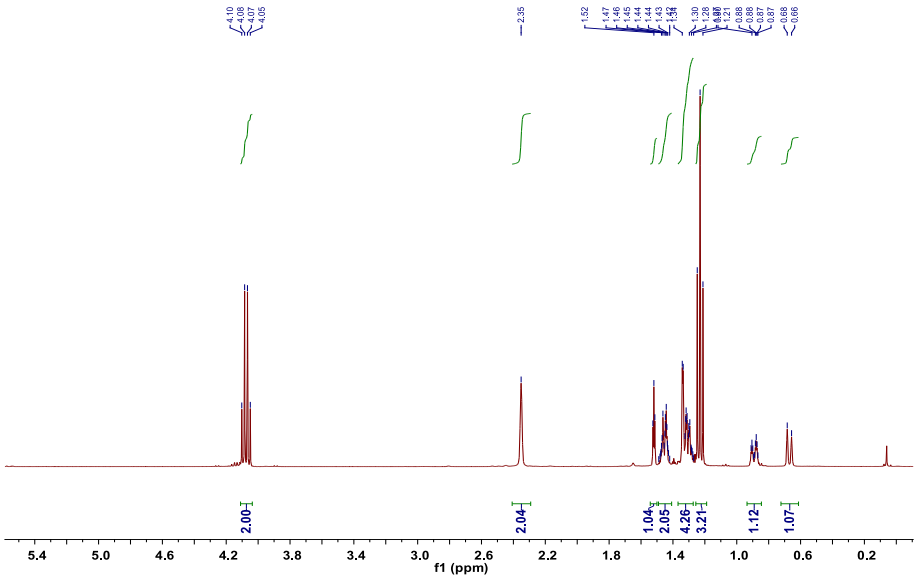

Figure S98. ^{1}H NMR spectrum of **31** ***trans***, related to Scheme 2.

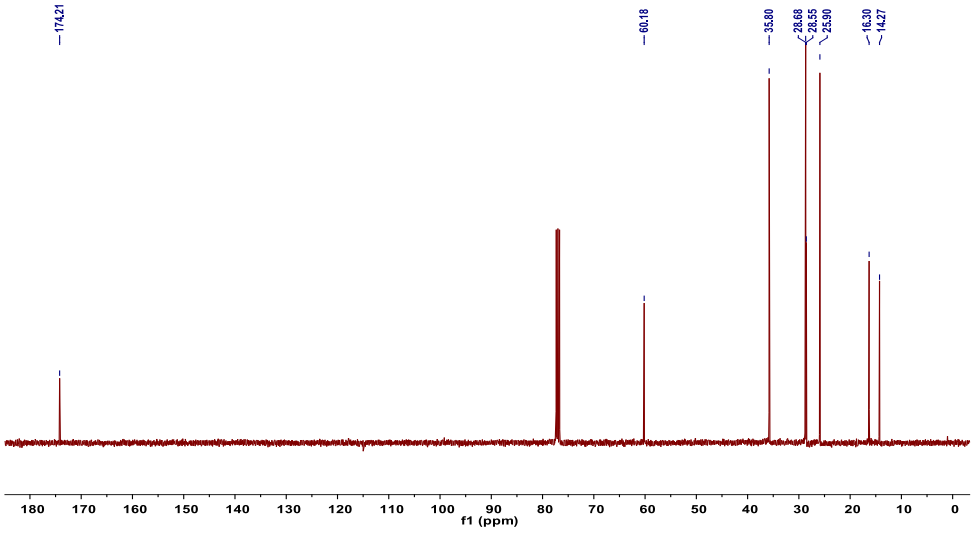

Figure S99. ^{13}C NMR spectrum of **31** ***trans***, related to Scheme 2.

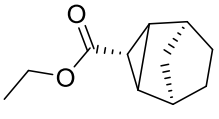

(Cis)

31: ^{1}H NMR (400 MHz, $CDCl_3$) δ 4.13 (q, J = 7.1 Hz, 2H), 2.50 (s, 2H), 1.54 – 1.43 (m, 2H), 1.32 – 1.20 (m, 6H), 1.10 (d, J = 7.5 Hz, 2H), 0.74 (dd, J = 3.5, 1.7 Hz, 2H); **^{13}C NMR** (101 MHz, $CDCl_3$) δ 172.4, 60.5, 36.0, 29.5, 29.4, 21.7, 20.8, 14.1.

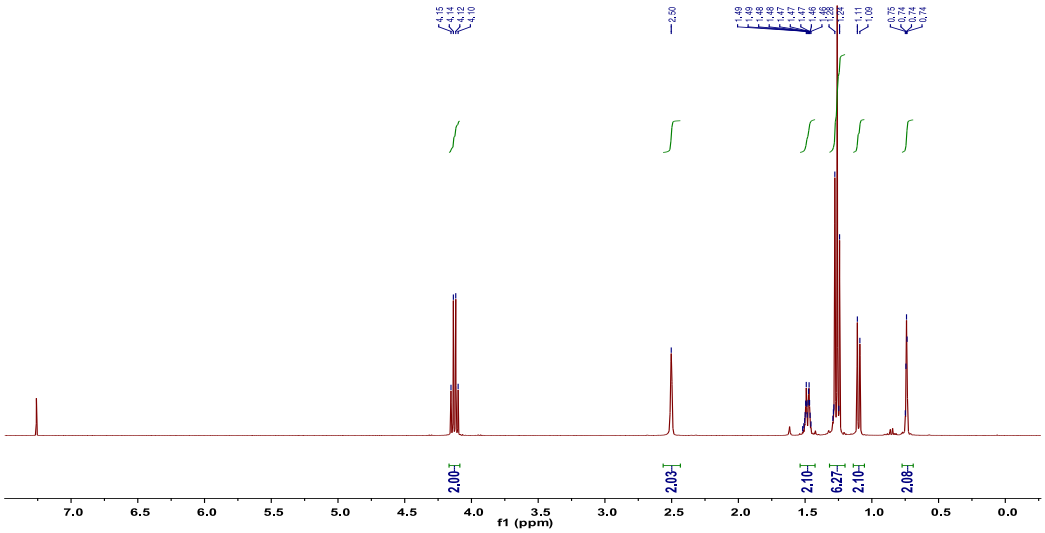

Figure S100. ^{1}H NMR spectrum of **31** ***cis***, related to Scheme 2.

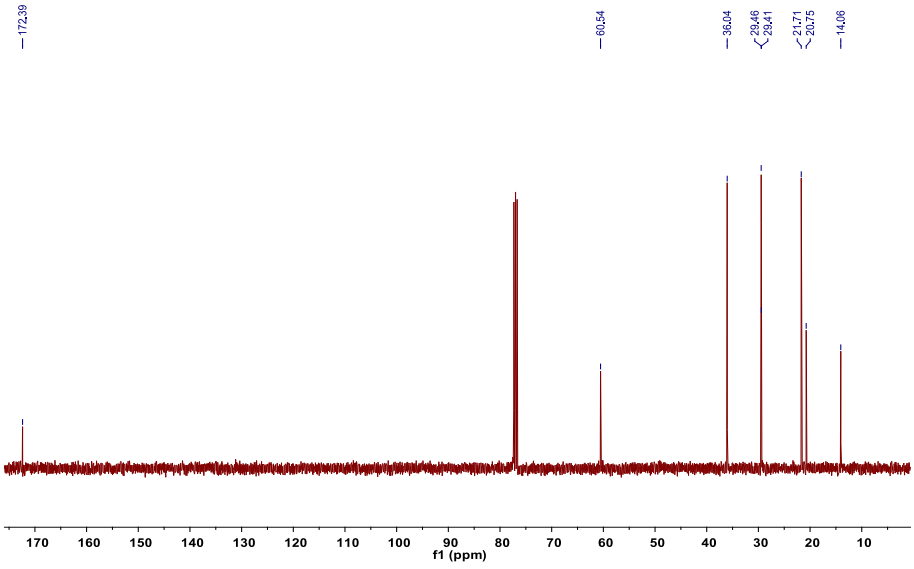

Figure S101. ^{13}C NMR spectrum of **31** ***cis***, related to Scheme 2.

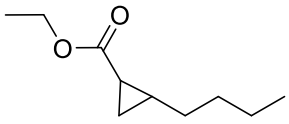

(Trans+cis)

32: ^{1}H NMR (400 MHz, $CDCl_3$, trans and cis-isomers): δ 4.13-4.09 (q, J = 7.2 Hz, cis-2H), 4.13-4.19 (q, J = 7.1 Hz, trans-2H), 1.70–1.10 (m, 24H), 1.03–0.93 (m, cis-1H), 0.89 (t, J = 7.0 Hz, trans-3H), 0.88 (t, J = 6.9 Hz, cis-3H), 0.68 (ddd, J = 4.1, 5.4, 7.6 Hz, trans-1H); **^{13}C NMR** (101 MHz, $CDCl_3$) δ 174.6, 173.0, 60.2, 60.1, 32.7, 31.8, 31.2, 26.7, 22.9, 22.4, 22.3, 21.9, 20.2, 18.21, 15.5, 14.3, 14.3, 14.0, 14.0, 13.3.

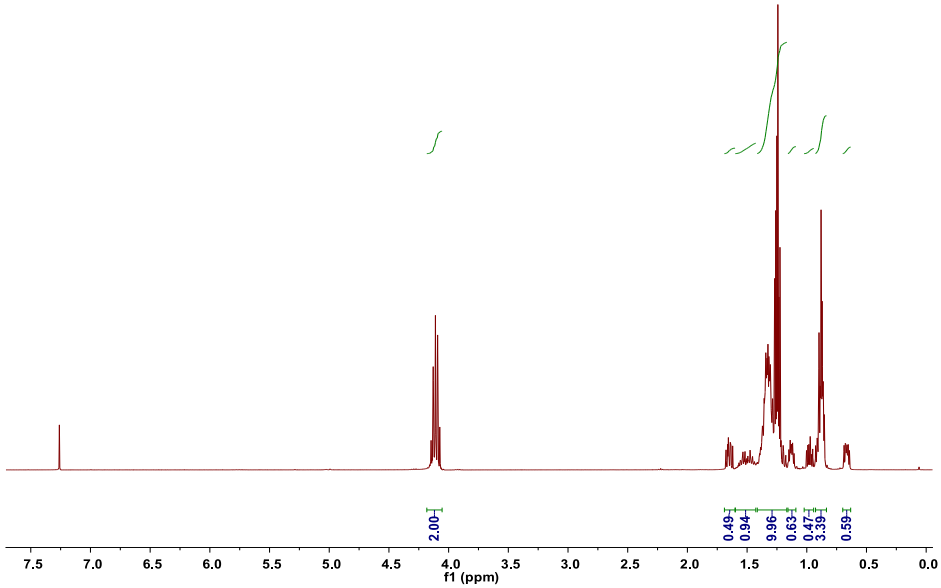

Figure S102. ^{1}H NMR spectrum of **32**, related to Scheme 2.

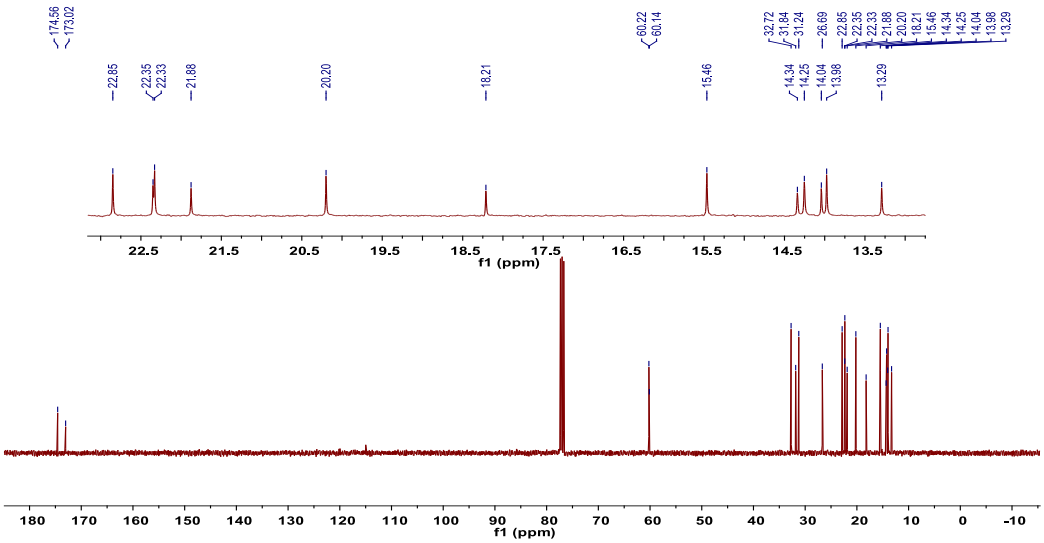

Figure S103. ^{13}C NMR spectrum of **32**, related to Scheme 2.

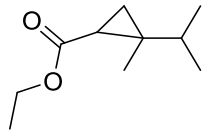

(Trans+Cis)

33: **^{1}H NMR** (400 MHz, $CDCl_3$) δ 4.19 – 4.04 (m, 4H), 1.73 (dt, J = 13.8, 6.9 Hz, 1H), 1.46 (ddd, J = 20.3, 7.9, 5.5 Hz, 2H), 1.25 (td, J = 7.1, 1.0 Hz, 6H), 1.11 – 0.92 (m, 18H), 0.85 – 0.78 (m, 5H); **^{13}C NMR** (101 MHz, $CDCl_3$) δ 172.7, 172.7, 60.2, 60.1, 38.0, 32.0, 31.6, 28.9, 27.84, 26.8, 22.0, 21.4, 19.5, 19.2, 19.1, 19.0, 18.3, 14.4, 14.3, 11.1.

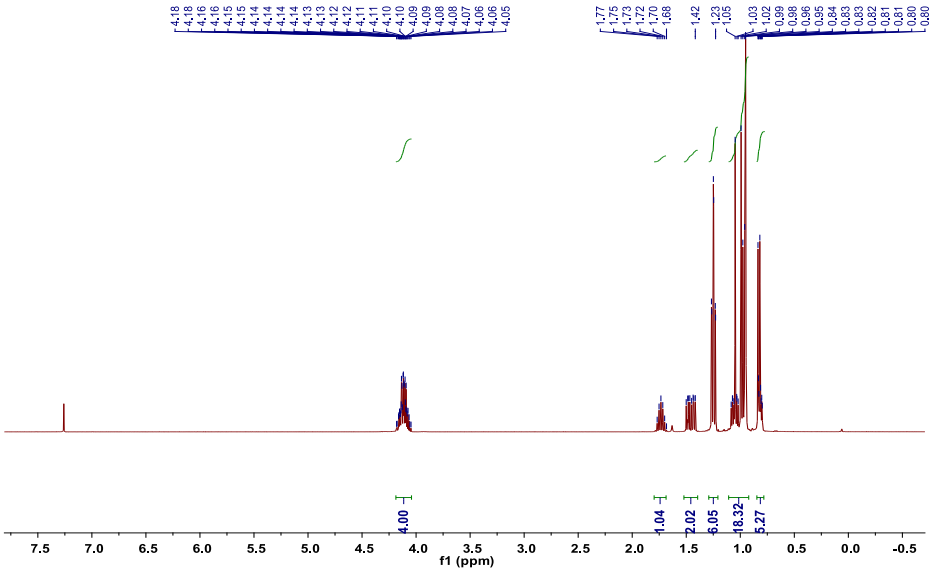

Figure S104. ^{1}H NMR spectrum of **33**, related to Scheme 2.

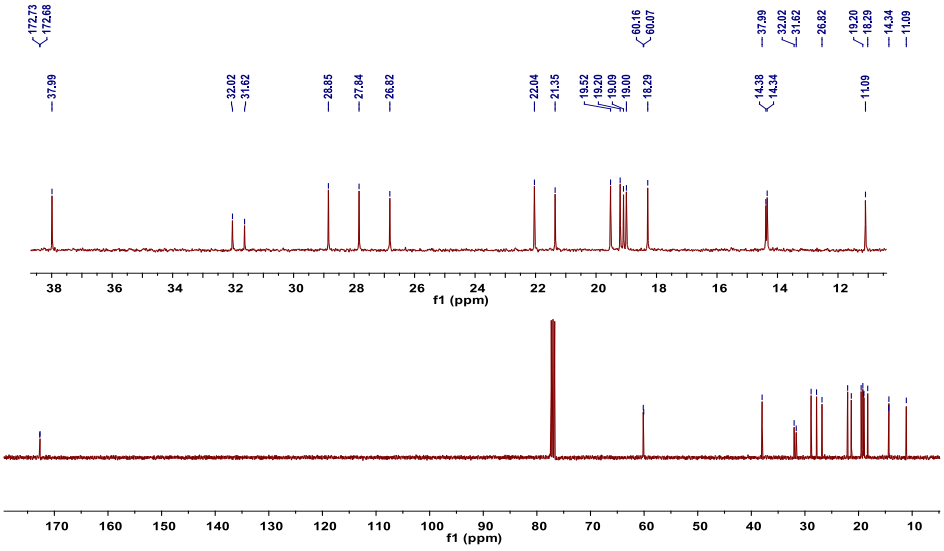

Figure S105. ^{13}C NMR spectrum of **33**, related to Scheme 2.

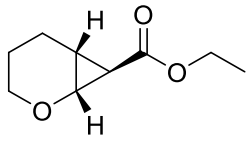

(Trans)

34: **^{1}H NMR** (400 MHz, $CDCl_3$) δ 4.19 – 4.04 (m, 2H), 3.90 (dd, J = 5.8, 3.4 Hz, 1H), 3.65 – 3.53 (m, 1H), 3.36 (td, J = 11.2, 2.2 Hz, 1H), 2.09 – 1.88 (m, 2H), 1.80 – 1.65 (m, 2H), 1.58 – 1.38 (m, 2H), 1.24 (t, J = 7.1 Hz, 3H); **^{13}C NMR** (101 MHz, $CDCl_3$) δ 172.4, 64.5, 60.34, 59.8, 26.5, 22.0, 21.9, 18.9, 14.3.

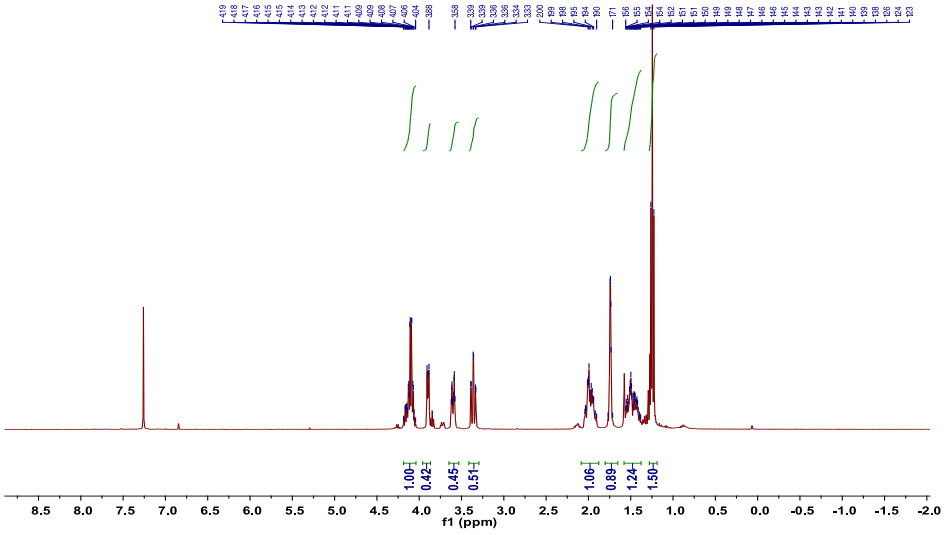

Figure S106. ^{1}H NMR spectrum of **34** ***trans***, related to Scheme 2.

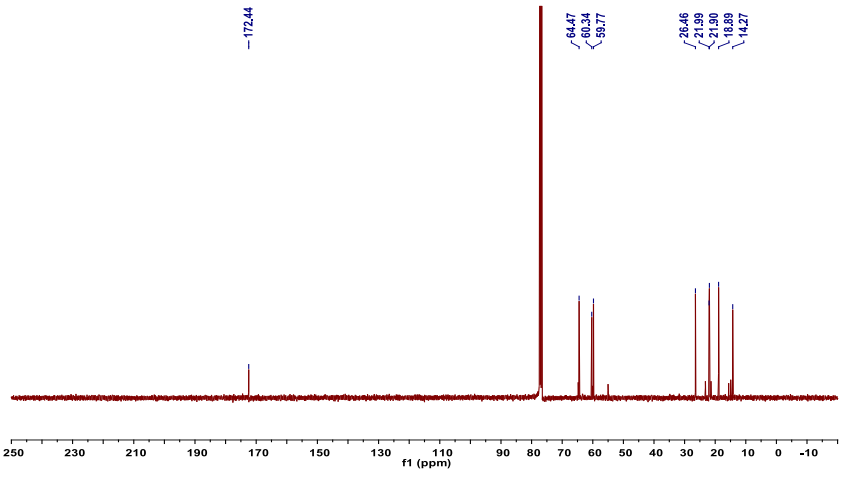

Figure S107. ^{13}C NMR spectrum of **34** ***trans***, related to Scheme 2.

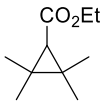

35: **^{1}H NMR** (400 MHz, $CDCl_3$) δ 4.07 (q, J = 7.1 Hz, 2H), 1.27 – 1.22 (m, 9H), 1.17 (s, 6H), 1.16 (s, 1H); **^{13}C NMR** (101 MHz, CDCl3) δ 172.1, 59.5, 35.8, 29.8, 23.5, 16.5, 14.4.

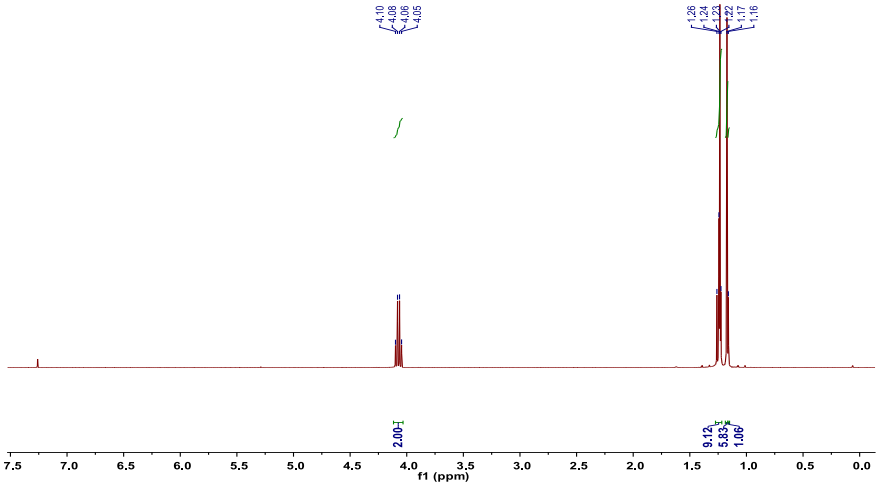

Figure S108. ^{1}H NMR spectrum of **35**, related to Scheme 2.

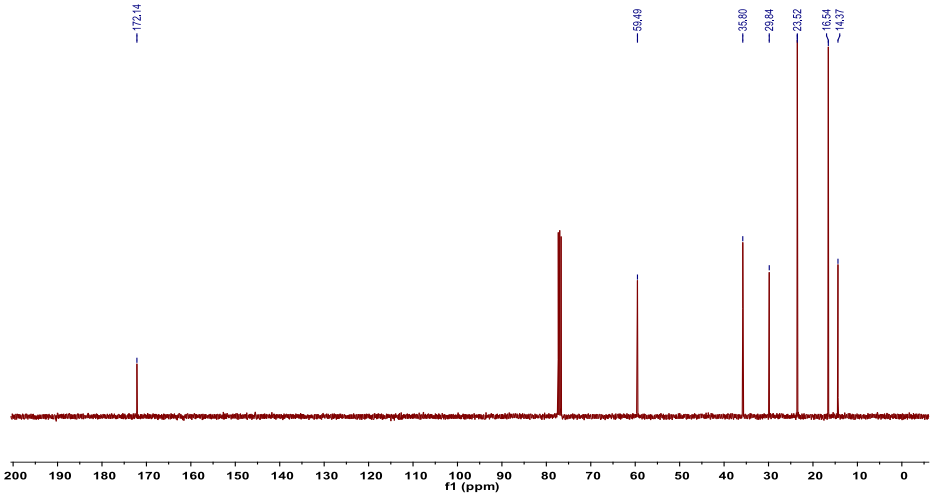

Figure S109. ^{13}C NMR spectrum of **35**, related to Scheme 2.

DFT Calculations

All theoretical calculations were based on density functional theory (DFT) and have been performed with the ORCA program package.[6] Geometry optimization were performed with the hybrid functional B3LYP using the TZVP[7] basis set for all atoms and by taking advantage of the resolution of the identity (RI) approximation in the Split-RI-J variant[8] with the appropriate Coulomb fitting sets.[9] Increased integration grids (Grid4 in ORCA convention) and tight SCF convergence criteria were used. Complexes **1**, **36**, **37** and **3** consist of two to three magnetically interacting centres and can be best described by the Broken Symmetry (BS) approach,[10] as already demonstrated in studies of related systems.[11] Single-point BS-DFT calculations were performed with the hybrid functional B3LYP[12] and the alternative spin configurations for the BS calculations were generated with the "FlipSpin" feature of ORCA. For the description of the systems we used the isotropic Heisenberg-Dirac-Van Vleck (HDvV) exchange Hamiltonian[13] $H = -2\sum_{i>j} J_{ij} S_i S_j$ where J_{ij} is the exchange coupling between pairwise number *i* and *j* while *Si* is the spin operator of the *i*th metal center. The possible pairwise exchange couplings in these systems were determined within the BS-DFT framework and diagonalization of the HDvV Hamiltonian which provides the magnetic sublevel spectrum of the species was performed by employing the orca_eca utility of ORCA. The relative energies were also obtained from single-point calculations using the B3LYP functional together with the TZV/P basis set. They were computed from the gas-phase optimized structures as a sum of electronic energy and thermal corrections to free energy. Zero point vibrational energy (ZPVE)

---

[6] F. Neese, *Wiley Interdiscip. Rev. Comput. Mol. Sci.* **2012**, *2*, 73–78.
[7] A. Schäfer, C. Huber, R. J. Ahlrichs, *Chem. Phys.* **1994**, *100*, 5829–5835.
[8] F. Neese, *J. Comput. Chem.* **2003**, *24*, 1740–1747.
[9] F. Weigend, *PhysChemChemPhys* **2006**, *8*, 1057–1065.
[10] a) L. Noodleman, J. *Chem. Phys.* **1981**, *74*, 5737–5743; b) L. Noodleman, E. R. Davidson, *Chem. Phys.* **1986**, *109*, 131–143.
[11] a) A. D. Pantazis, M. Orio, T. Petrenko, S. Zein, E. Bill, W. Lubitz, J. Messinger, F. Neese, *Chem. Eur. J.* **2009**, *15*, 5108–5123. b) C. Baffert, M. Orio, D. A. Pantazis, C. Duboc, A. G. Blackman, G. Blondin, F. Neese, A. Deronzier, M.-N. Collomb, *Inorg. Chem.,* **2009**, *48*, 10281–10288. c) A. Kochem, B. Faure, S. Bertaina, E. Rivière, M. Giorgi, M. Réglier, M. Orio, A. J. Simaan, *Eur J. Inorg. Chem.*, **2018**, *47*, 5039–5046.
[12] A. D. Becke, *J. Chem. Phys.* **1993**, *98*, 5648–5652; b) C. T.Lee, W. T. Yang, R. G. Parr, *Phys. Rev. B* **1988**, *37*, 785-789.
[13] a) P. A. M. Dirac, *Proc. Roy. Soc.* **1929**, *A123*, 714; b) W. Heisenberg, *Z.* Physik **1926**, *38*, 411-426; c) W. Heisenberg, *Z. Physik* **1928**, *49*, 619-636; d) J. H. Vleck, In *The Theory of Electronic and Magnetic Susceptibilies*, Oxford University: London: **1932**; p 384.

corrections[14] were evaluated from the calculated harmonic frequencies and are included in the total energies. The counterpoise (CP) procedure was used to correct the total energy for the basis set superposition error (BSSE).[15] Molecular orbitals and spin-density plots were generated using the orca plot utility program and were visualized with the Chemcraft program.[16]

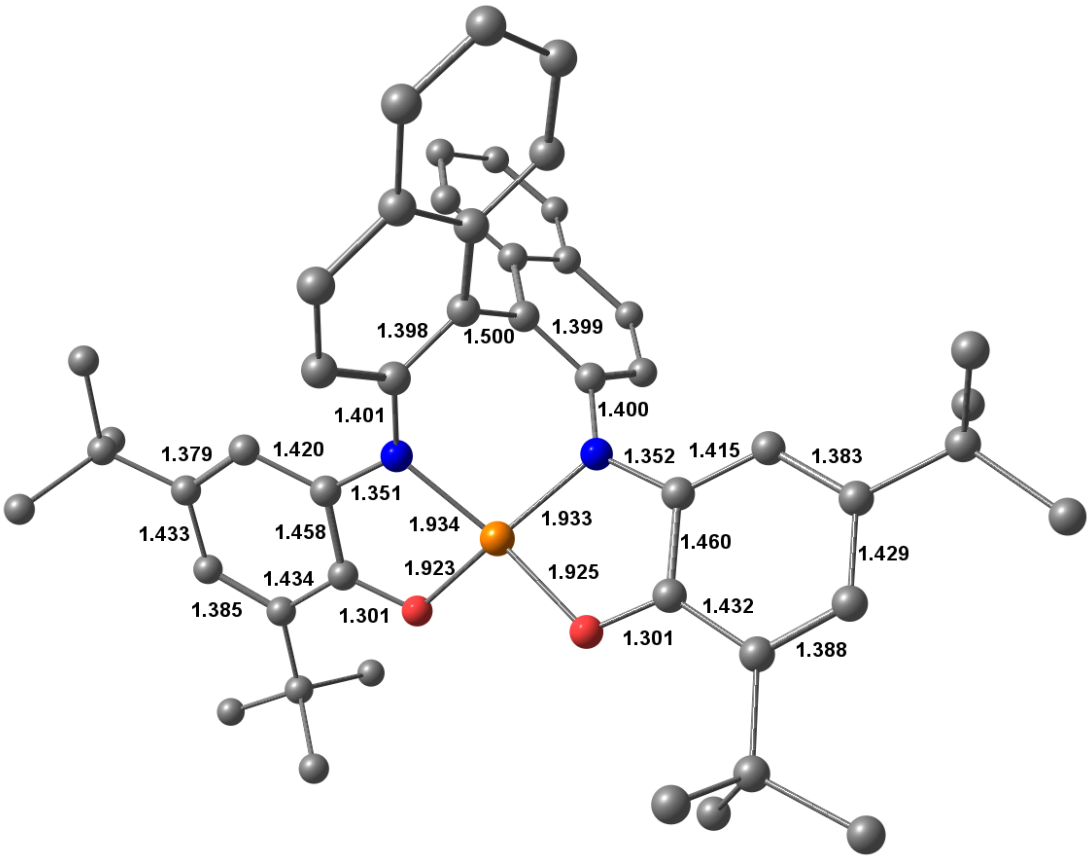

Figure S110. DFT-optimized structure of **3** and selected metrical parameters. Color scheme: Cu brown, O red, N blue and C grey. Protons were omitted for clarity, related to Scheme 3.

[14] R. Krishnan, J. S. Binkley, R. Seeger, J. A. Pople, *J Chem. Phys.* **1980**, *72*, 650-654.

[15] a) S. F. Boys, F. Bernardi, *Mol. Phys.* **1970**, 19, 553-566; b) S. Simon, M. Duran, J. J. Dannenberg, *J. Chem. Phys.* **1996**, *105*, 11024-11031.

[16] Chemcraft, http://chemcraftprog.com.

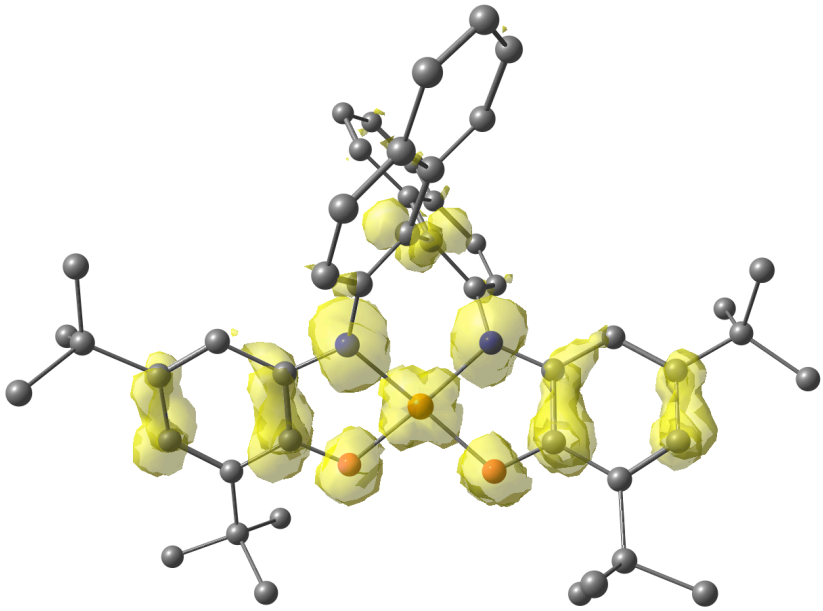

Figure S111. Spin density plot for the HS state of **3**, related to Scheme 3.

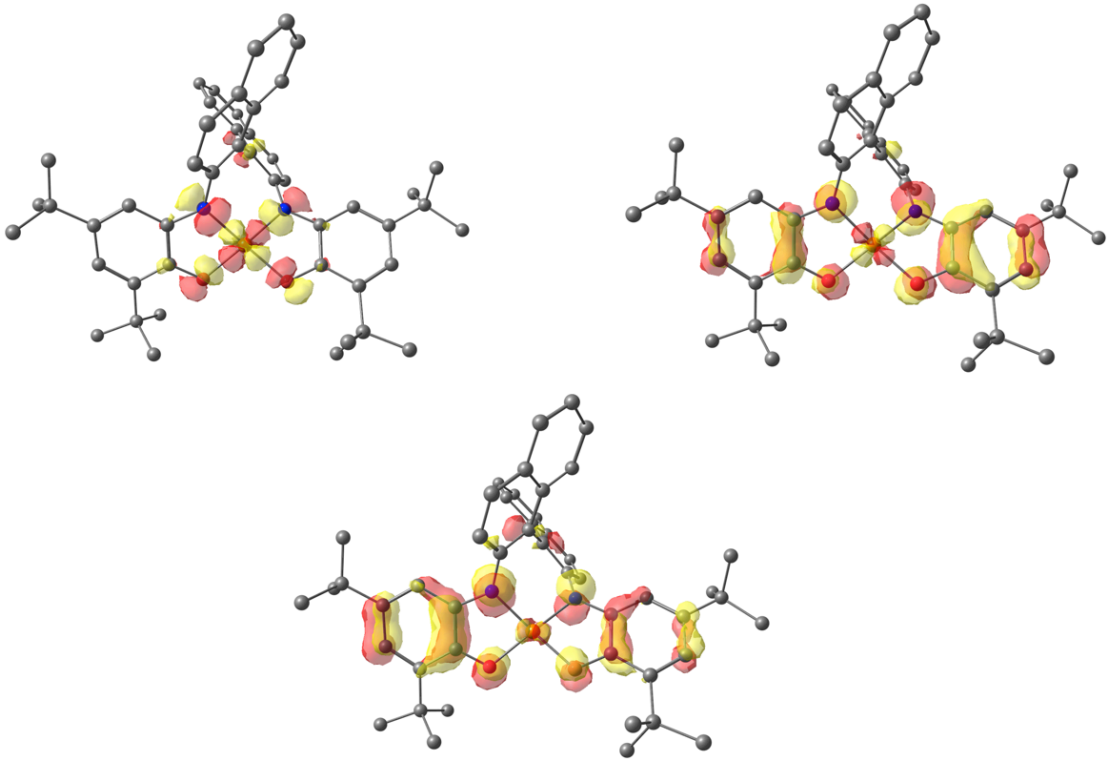

Figure S112. Localized SOMOs of the high-spin state of **3**, related to Scheme 3.

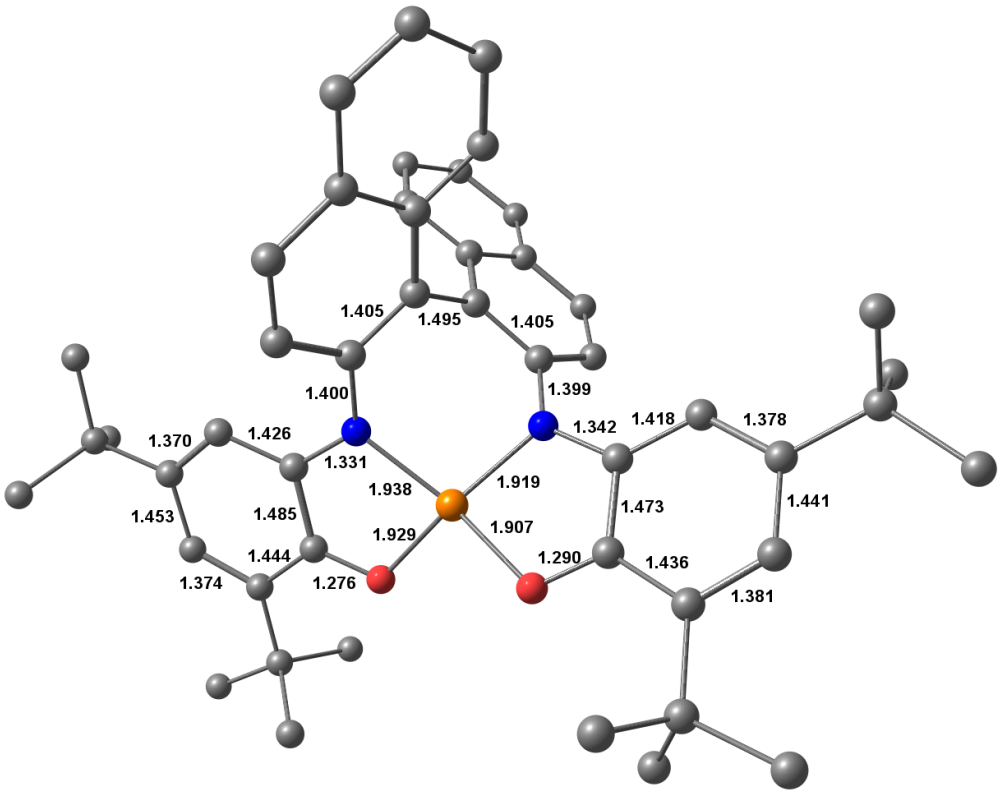

Figure S113. DFT-optimized structure of **1** and selected metrical parameters. Color scheme: Cu brown, O red, N blue and C grey. Protons were omitted for clarity, related to Scheme 3.

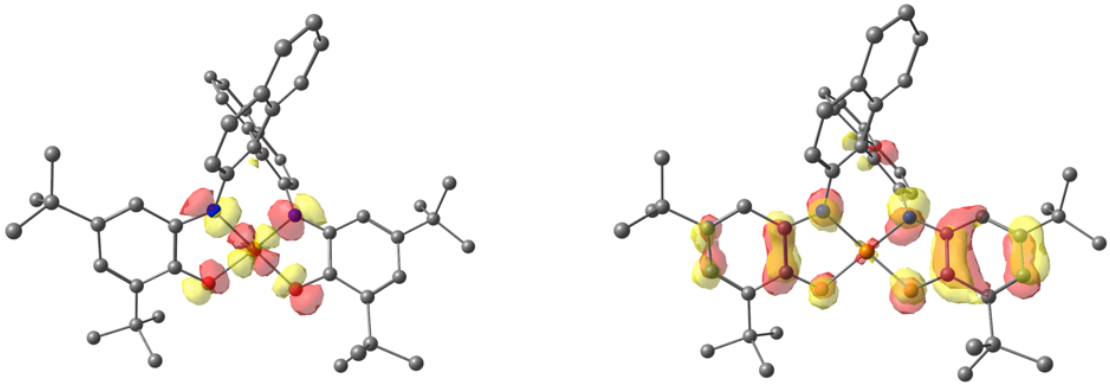

Figure S114. Localized SOMO of the high-spin state of **1**, related to Scheme 3.

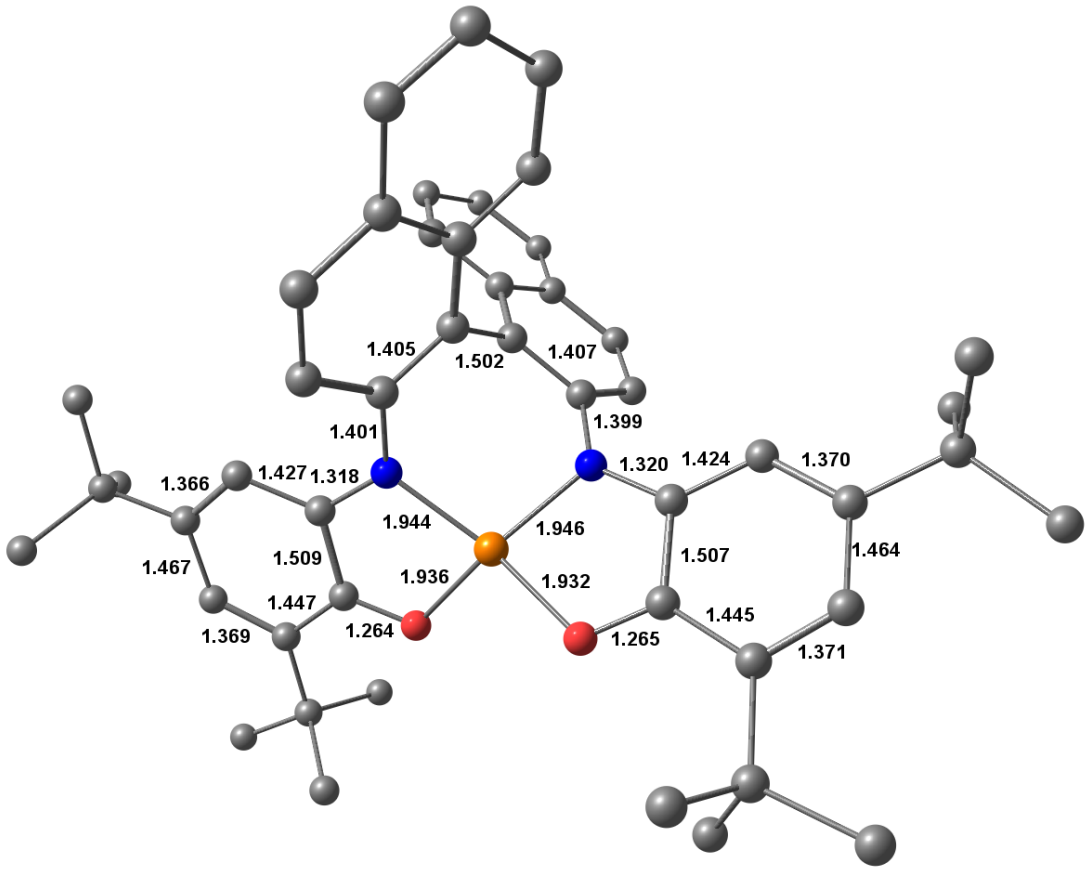

Figure S115. DFT-optimized structure of **5** and selected metrical parameters. Color scheme: Cu brown, O red, N blue and C grey. Protons were omitted for clarity, related to Scheme 3.

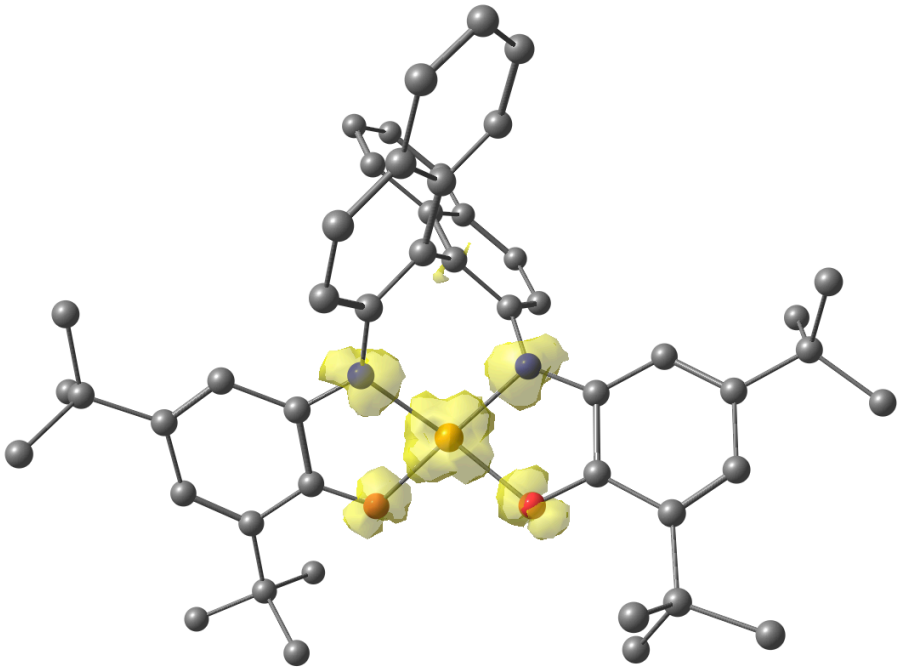

Figure S116. Spin density plot for **5**, related to Scheme 3.

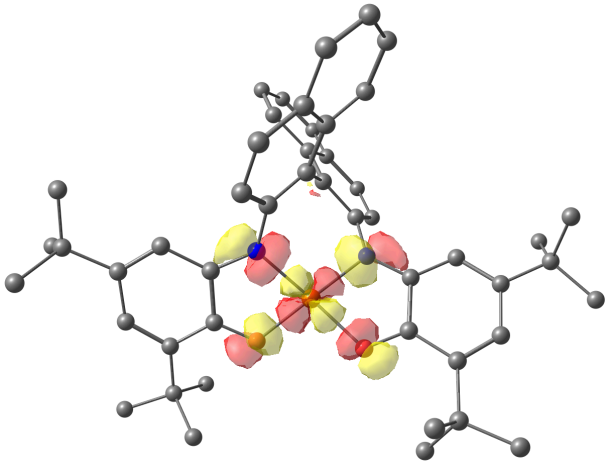

Figure S117. Localized SOMOs of **5**, related to Scheme 3.

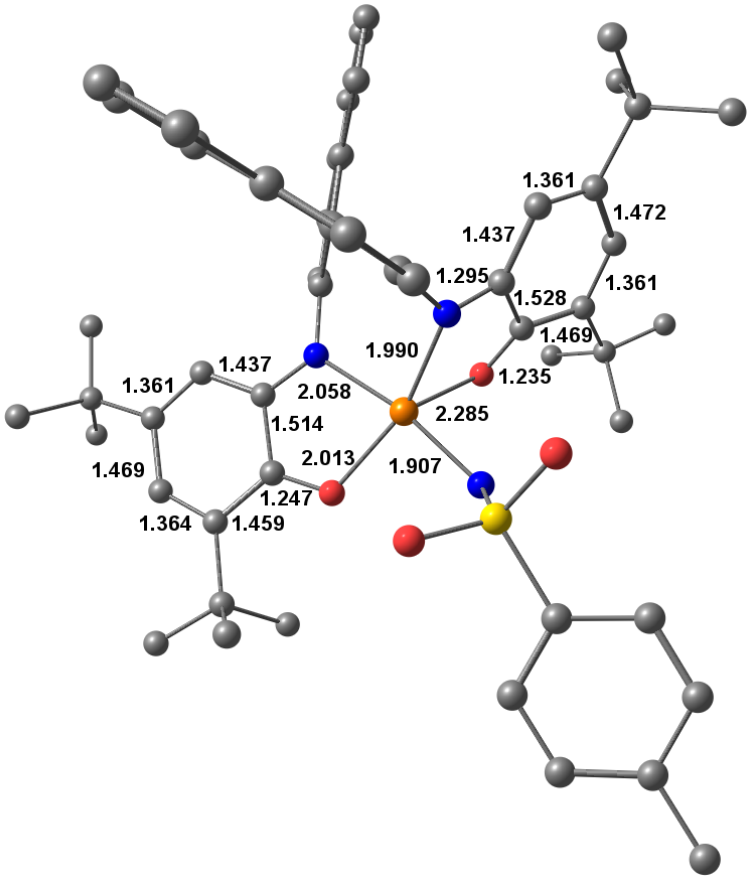

Figure S118. DFT-optimized structure of **36a** and selected metrical parameters. Color scheme: Cu brown, O red, N blue and C grey. Protons were omitted for clarity, related to Figure 4.

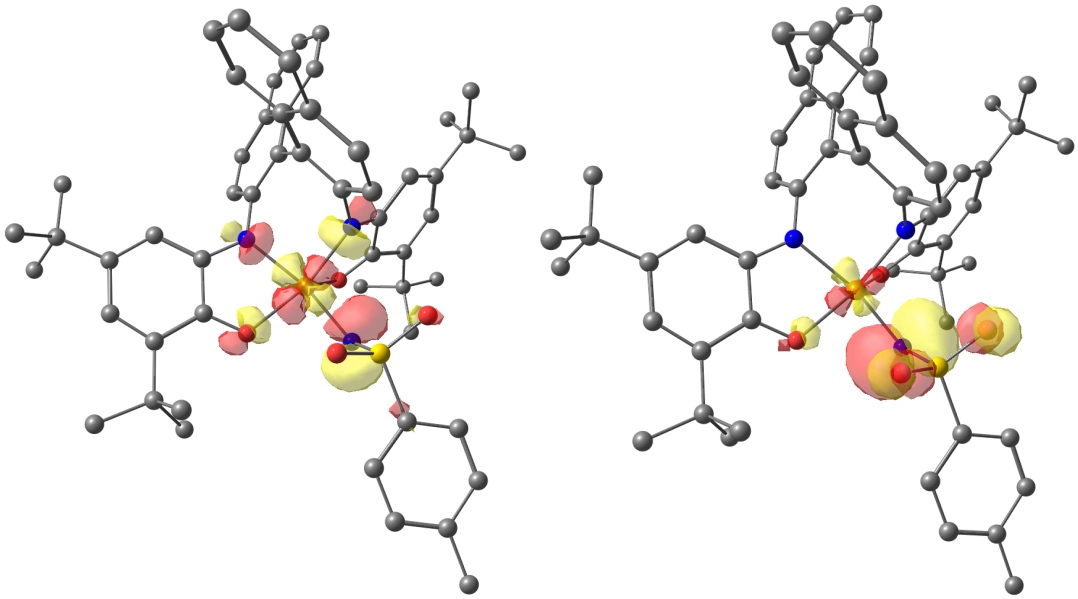

Figure S119. Localized SOMOs of the high-spin state of **36a**, related to Figure 4.

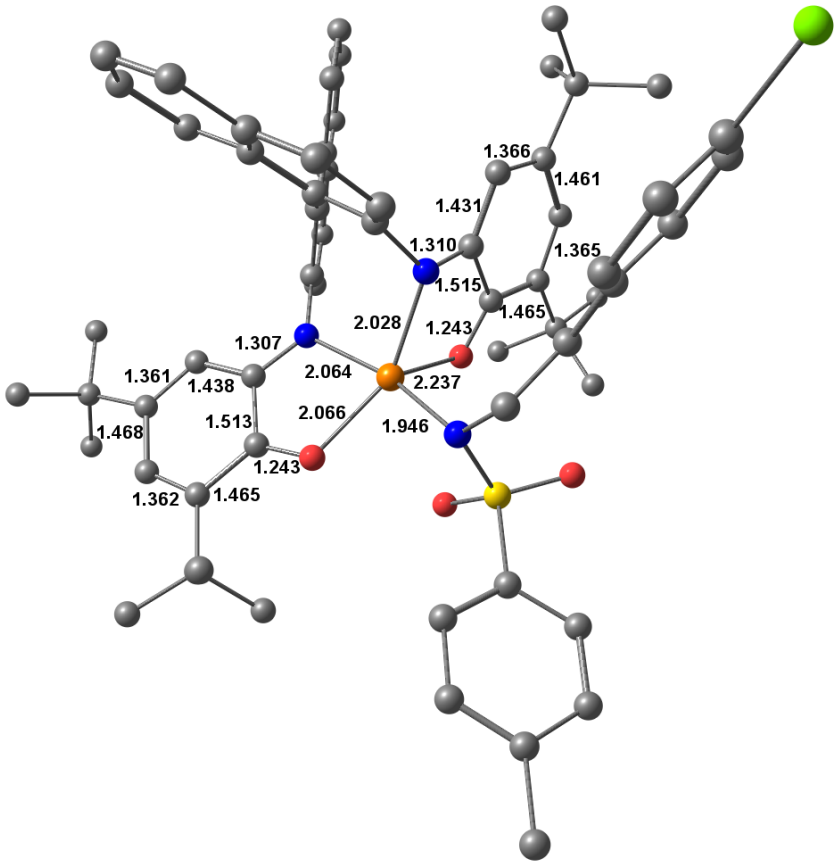

Figure S120. DFT-optimized structure of **37a** and selected metrical parameters. Color scheme: Cu brown, O red, N blue and C grey. Protons were omitted for clarity, related to Figure 4.

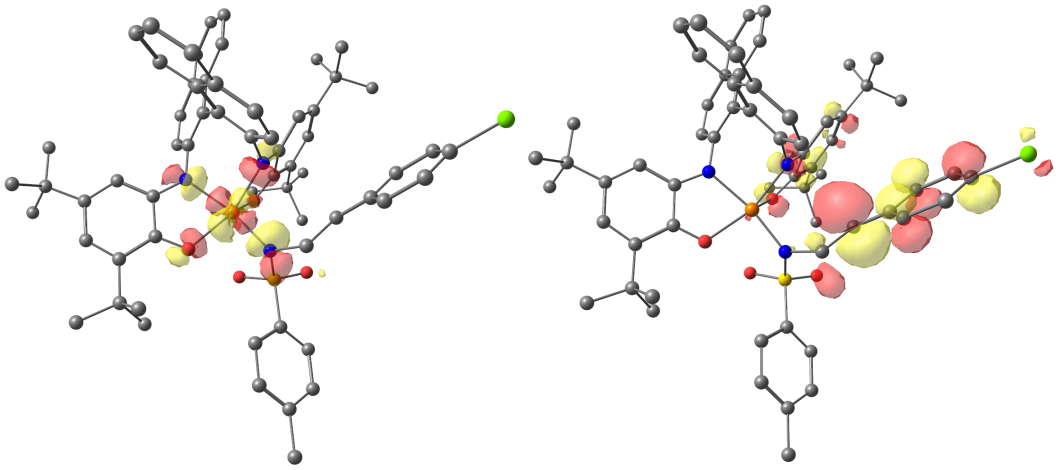

Figure S121. Localized SOMOs of the high-spin state of **37a**, related to Figure 4.

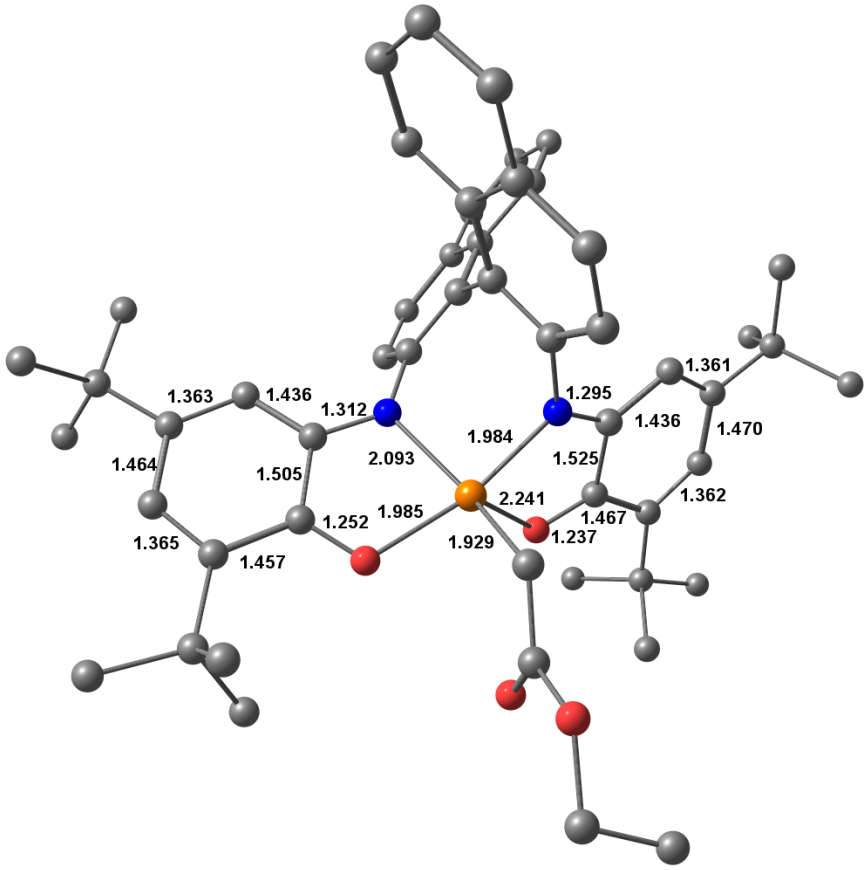

Figure S122. DFT-optimized structure of **36b** and selected metrical parameters. Color scheme: Cu brown, O red, N blue and C grey. Protons were omitted for clarity, related to Figure 4.

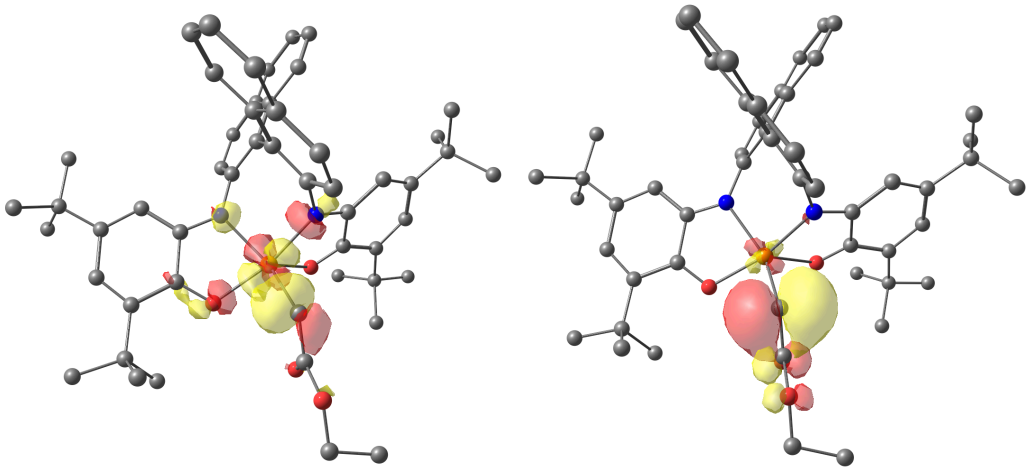

Figure S123. Localized SOMOs of the high-spin state of **36b**, related to Figure 4.

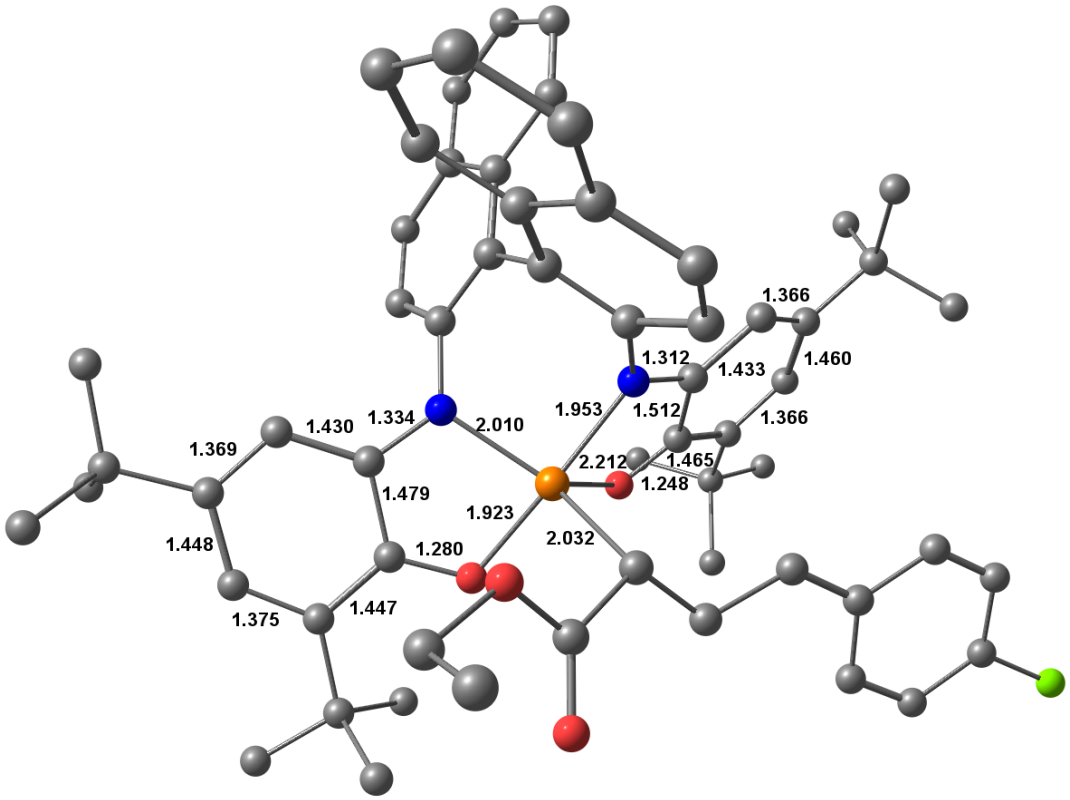

Figure S124. DFT-optimized structure of **37b** and selected metrical parameters. Color scheme: Cu brown, O red, N blue and C grey. Protons were omitted for clarity, related to Figure 4.

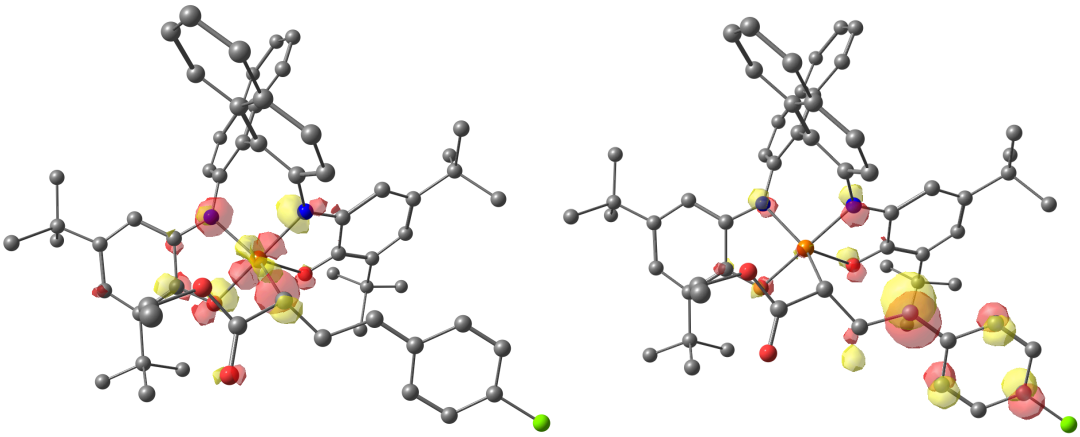

Figure S125. Localized SOMOs of the high-spin state of **37b**, related to Figure 4.

Table S15. DFT-calculated ground spin states (GS) and energetic separation (cm^{-1}) with the first excited states (ES), Boltzmann populations at 298 K and computed exchange coupling constants (cm^{-1}) of **3**, **1**, **36a, 36b, 37a** and **37b**, related to Figure 4.

Species	**3**	**1**	**36a**	**37a**	**36b**	**37b**
GS	0, S = 1/2	0, S = 1	0, S = 1	0, S = 0	0, S = 1	0, S = 0
ES	258, S= 3/2	314, S= 0	1116, S= 0	124, S= 1	1642, S= 0	6, S= 1
Boltzmann populations	78% S =1/2 22% S =3/2	79% S =1 21% S =0	99% S =1 1% S =0	65% S =0 35% S =1	99% S =1 1% S =0	51% S =0 49% S =1
J	-303 (SQ-SQ) +332 (Cu-SQ) +366 (Cu-SQ)	+140 (Cu-SQ)	+958 (Cu-NTs)	-62 (Cu-Styr)	+821 (Cu-Carb)	-3 (Cu-Styr)

Table S16. DFT-calculated final energies for the intermediates obtained upon nitrene insertion on complexes **4** and **1**, related to Figure 4.

Species	E(Eh)	ΔE(Eh)	ΔE(kcal/mol)
Nitrene	-874.0129	-	-
4	-3453.9334	-	-
4 + nitrene	-4327.9463	+0.0702	+44.1
Adduct **4**-nitrene	-4328.0165	0	0
1	-3759.7575	-	-
1 + nitrene	-4633.7704	+0.0742	+46.6
Adduct **1**-nitrene, **36a**	-4633.8446	0	0

Table S17. DFT-calculated final energies for the intermediates obtained upon alkene insertion on nitrene intermediates obtained from complexes **4** and **1**, related to Figure 4.

Species	E(Eh)	ΔE(Eh)	ΔE(kcal/mol)
Nitrene-alkene	1643.2177	-	-
4	-3453.9334	-	-
4 + nitrene-alkene	-5097.1511	+0.0002	+0.1
Adduct **4**-nitrene-alkene	-5097.1513	0	0
1	-3759.7575	-	-
1 + nitrene-alkene	-5402.9752	+0.0115	+7.2
Adduct **1**-nitrene alkene, **37a**	-5402.9867	0	0

Table S18. Comparison of catalytic efficiency for copper-catalyzed aziridination, related to Figure 4.

Substrate	Product	Catalyst	Reaction conditions	Yield	Reference
1-hexene	**17**	$(py)_2CuCl_2$	Catalyst (5 mol%), 10 min 1 equiv PhINTs, 2 equiv $NaBAr^F{}_4$	49%	*J. Org. Chem.* **2005**, *70*, 4833-4839
		Complex **1**	See scheme 1	80%	This work
O-acyl geranium	**19** and **20**	Trispyrazolylborate Ag catalyst	Catalyst (5% mol), 8 h [cat]:[PhINTs]:[diene] = 1:20:30	93%	*J. Am. Chem. Soc.* **2014**, *136*, 5342−5350
		Complex **1**	See scheme 1	86%	This work
Styrene derivatives Ar–CH=CH_2	Ar = Ph	(bispidine)copper(II) complex	Catalyst (5 mol%), 6 min 1 equiv PhINTs, 22 equiv. styrene	91%	*Chem. Eur. J.* **2008**, *14*, 5313 – 5328
	Ar = 4-Cl-Ph, **8**	Complex **1**	See scheme 1	>99%	This work